

Analysis of second-moments and their budgets for Richtmyer–Meshkov instability and variable-density turbulence induced by re-shock

Man Long Wong*

*Department of Aeronautics and Astronautics, &
Center for Turbulence Research, Stanford, CA 94305, USA*

Jon R. Baltzer

*XTD-IDA, Los Alamos National Laboratory
Los Alamos, NM 87545, USA*

Daniel Livescu

*CCS-2, Los Alamos National Laboratory
Los Alamos, NM 87545, USA*

Sanjiva K. Lele

*Department of Aeronautics and Astronautics,
Department of Mechanical Engineering, &
Center for Turbulence Research, Stanford University
Stanford, CA 94305, USA
(Dated: October 11, 2024)*

The nonlinear Richtmyer–Meshkov instability and mixing transition induced by a Mach 1.45 shock and subsequent re-shock at an interface between two ideal gases (sulphur hexafluoride and air) with high Atwood number are studied with second-moment analysis using data from high-resolution compressible Navier–Stokes simulations. The analysis first addresses the importance of second-order moments: turbulent mass flux and density-specific-volume covariance, together with their transport equations. These quantities play an essential role on the development of Favre-averaged Reynolds stress and turbulent kinetic energy in this variable-density flow. Then, grid sensitivities and the time evolution of the second-moment quantities are investigated, followed by a detailed study of the transport equations of the second-moments using fully resolved data before re-shock. After re-shock, budgets of large-scale second-moments, which have insignificant influence from numerical regularization, are studied with the effects of subfilter-scale stress accounted. The effects of subfilter-scale stress on the budgets of large-scale second-moments with different levels of filtering are also examined.

* mlwong@alumni.stanford.edu

I. INTRODUCTION

Richtmyer–Meshkov (RM) instability, or RMI [1, 2], arises in many natural phenomena and engineering applications when a shock wave traverses an interface separating two materials of different densities. RMI is used by astrophysicists to explain the cause of turbulent mixing during supernova explosion [3–5] and is also taken into account in many stellar models [6]. In inertial confinement fusion (ICF), it is a common belief that there exists mixing between the capsule material and fuel due to RMI that prohibits a useful yield obtained from a fusion reaction for power generation [7–9]. RMI is also employed in some proposed combustion systems since it can enhance the mixing of fuel and oxidizer in supersonic and hypersonic air-breathing engines [10, 11]. RMI is similar to the Rayleigh–Taylor (RT) instability, or RTI, which appears when there is a gravitational acceleration pointing in the opposite direction of the density gradient across an interface. In contrast to RTI, RMI occurs because of impulsive acceleration and is unstable regardless of the direction of the acceleration. Turbulent mixing induced from RMI and RTI with high density variations at the interfaces falls into the category of variable-density turbulence [12], where the Atwood number, which is defined as the difference in the fluid densities divided by their sum, is high. Variable-density turbulent mixing can also be triggered by other types of instabilities at an interface, such as the Kelvin–Helmholtz (KH) instability, or KHI, at a shear layer [12].

Direct numerical simulation (DNS) [13], which resolves all scales in flows using a mesh with grid spacing of at least order of magnitude of the Kolmogorov scale, is a powerful tool for studying turbulent flows, especially flows with laminar to turbulent transition. However, its requirements of computational resources is tremendous for high Reynolds number flows and is computationally too expensive for many engineering applications, even on the largest supercomputers to date. As a result, turbulence modeling approaches are commonly adopted to avoid resolving all spatial and temporal scales in simulations of complex turbulent flows in the industry. The large eddy simulation (LES) and Reynolds averaged Navier–Stokes (RANS) methodologies are two popular modeling strategies [14, 15]. LES consists of modeling of small-scales that are assumed to be more universal and self-similar, while the larger scales are resolved on the grid. On the other hand, the entire flow structure is modeled based on statistical averaging in the RANS approach. In general, LES has higher fidelity than RANS-based simulations for turbulent flows where unsteady large-scales play critical roles, since the large-scale features are resolved in LES. However, LES also has larger demand on computational resources due to constraints on grid spacing and time step size for representing the motions of the scales captured. Often, the hybrid RANS-LES approach is chosen as a compromise between computational cost and accuracy [16].

The Besnard–Harlow–Rauenzahn (BHR) family of models based on second-moment closure represent a popular RANS-based approach for variable-density turbulence. The first version of BHR model was proposed by Besnard *et al.* [17], in which the unclosed Reynolds stress tensor in the multi-species Favre-averaged (density-weighted-averaged) Navier–Stokes (FANS) equations is closed with the aid of additional modeled transport equations. These include modeled equations of decay rate of turbulent kinetic energy and other second-moment quantities, such as turbulent mass flux and density-specific-volume covariance. These second-moments play important roles in variable-density turbulence; particularly the turbulent mass flux directly affects the development of Favre-averaged Reynolds stress. The modeling assumptions of the first BHR model were not tested against different types of variable-density flows until the work by Banerjee *et al.* [18], where simplifications of the original BHR model were also introduced. In their model (BHR *k-S-a*), the Favre-averaged equations are closed with the turbulent kinetic energy transport equation instead of the equation of the Reynolds stress tensor. The transport equation of the decay rate of turbulent kinetic energy is also replaced with a more physically interpretable transport equation of turbulent length scale. Their model was validated with the experimental data, but the model coefficients are tuned from flow to flow. Later, the BHR-2 model by Stalsberg-Zarling and Gore [19] was proposed. BHR-2 re-adopts the modeled transport equation of density-specific-volume covariance instead of an algebraic model in the BHR *k-S-a* model, which was only strictly valid for immiscible fluids. An improved BHR-3 model with modeled transport equations of Reynolds stress tensor and density-specific-volume covariance was proposed by Schwarzkopf *et al.* [20] and was shown capable of capturing the Reynolds normal stress anisotropy and density-specific-volume covariance well in various variable-density flows, without varying model coefficients. The BHR-3 model was further improved by Schwarzkopf *et al.* [21] with two length scales to capture the difference between the transport and dissipation turbulent scales in RTI-induced turbulence. Besides the BHR family of models, there are also similar models for turbulent mixing such as the second-moment model by Grégoire *et al.* [22] with Boussinesq approximation and the *k-L-a* model by Morgan and Wickett [23] extended from the *k-L* model [24].

Modeling based on the transport of second-moments is more popular in RANS-based approach for variable-density flows and most proposed LES models for the subfilter-scale (SFS) or subgrid-scale (SGS) terms are based on first-order closures [25]. These include the eddy-viscosity type SFS/SGS closure [26–28] and the stretched-vortex approach, such as [29, 30]. There is still a lack of research on the application of second-moments for the closure of SFS/SGS terms in LES. Besides, the role of SFS/SGS terms on the large-scale turbulent quantities, especially the resolved turbulent kinetic energy in variable-density flows, is still unclear. In this paper, we have performed high-resolution

RMI simulations with re-shock to provide high-fidelity data for analyzing the physical mechanisms underlying the evolution of second-moments. The set-up of the numerical experiment follows the highest Reynolds number three-dimensional (3D) case in our previous paper [31]. Before re-shock, the instability induced at the interface grows nonlinearly but does not achieve mixing transition. After re-shock, the flow inside the mixing layer transitions and remains turbulent with a wide span of scales until the end of simulation. The 3D simulation presented in this work is advanced to higher grid resolution compared to the cases in the previous work, with number of grid cells exceeding 4.5 billion. Grid sensitivity test shows that the second-moments required for closing the FANS equations are well grid-converged during the simulations. We also examine the budgets of the second-moment transport equations before and after re-shock. The budgets analyzed after re-shock are based on large-scale contributions to second-moments under the influence of the SFS stress. The budgets of the large-scale second-moments are not affected by the numerical regularization, and the effects of SFS stress in the evolution of large-scale second-moments are studied.

II. GOVERNING EQUATIONS

The conservative multi-component Navier–Stokes equations are solved in this study:

$$\frac{\partial \rho Y_i}{\partial t} + \nabla \cdot (\rho \mathbf{u} Y_i) = -\nabla \cdot \mathbf{J}_i, \quad (1)$$

$$\frac{\partial \rho \mathbf{u}}{\partial t} + \nabla \cdot (\rho \mathbf{u} \mathbf{u} + p \boldsymbol{\delta}) = \nabla \cdot \boldsymbol{\tau}, \quad (2)$$

$$\frac{\partial E}{\partial t} + \nabla \cdot [(E + p) \mathbf{u}] = \nabla \cdot (\boldsymbol{\tau} \cdot \mathbf{u} - \mathbf{q}_c - \mathbf{q}_d), \quad (3)$$

where ρ , $\mathbf{u} = [u, v, w]^T = [u_1, u_2, u_3]^T$, p , and E are the density, velocity vector, pressure, and total energy of the fluid mixture respectively. Y_i is the mass fraction of species $i \in [1, 2, \dots, N]$, with N the total number of species. \mathbf{J}_i is diffusive mass flux for species i . $\boldsymbol{\tau}$, \mathbf{q}_c , and \mathbf{q}_d are viscous stress tensor, conductive heat flux, and inter-species diffusional enthalpy flux, respectively. $\boldsymbol{\delta}$ is the identity tensor. Since all Y_i 's sum up to one by definition, the continuity equation for the mixture density can be derived by summing up the continuity equations of all species given by equation (1) as:

$$\frac{\partial \rho}{\partial t} + \nabla \cdot (\rho \mathbf{u}) = 0. \quad (4)$$

The mixture is assumed to be ideal and calorically perfect, with:

$$E = \rho \left(e + \frac{1}{2} \mathbf{u} \cdot \mathbf{u} \right), \quad (5)$$

$$p = (\gamma - 1) \rho e, \quad e = c_v T, \quad (6)$$

where e and T are respectively specific internal energy and temperature of the mixture. γ and c_v are the ratio of specific heats and specific heat at constant volume of the mixture respectively.

The multi-component diffusive mass flux of species i is given by [32]:

$$\mathbf{J}_i = \rho \frac{M_i}{M^2} \sum_{j=1}^N M_j \tilde{D}_{ij} \nabla X_j, \quad (7)$$

where M_i and X_i are respectively the molecular weight and mole fraction of species i . M is the molecular weight of the mixture and \tilde{D}_{ij} is the ij th element of the matrix of ordinary multi-component diffusion coefficients $\tilde{\mathbf{D}}$. The mole fraction of species i is given by:

$$X_i = \frac{M}{M_i} Y_i. \quad (8)$$

The multi-component diffusive mass flux is reduced to the Fick's law for binary mixture:

$$\mathbf{J}_i = -\rho D_i \nabla Y_i, \quad i = 1, 2, \quad (9)$$

where $D_1 = D_2$ is the binary diffusion coefficient. Note that the Fick's law is sufficient in this work since only binary mixture is studied.

The viscous stress tensor $\boldsymbol{\tau}$ for a Newtonian mixture is:

$$\boldsymbol{\tau} = 2\mu\mathbf{S} + \left(\mu_v - \frac{2}{3}\mu\right)\boldsymbol{\delta}(\nabla \cdot \mathbf{u}), \quad (10)$$

where μ and μ_v are the shear viscosity and bulk viscosity respectively of the mixture. \mathbf{S} is the strain-rate tensor given by:

$$\mathbf{S} = \frac{1}{2} \left[\nabla \mathbf{u} + (\nabla \mathbf{u})^T \right]. \quad (11)$$

The conductive flux and the inter-species diffusional enthalpy flux [33] are given by:

$$\mathbf{q}_c = -\kappa \nabla T, \quad (12)$$

$$\mathbf{q}_d = \sum_{i=1}^N h_i \mathbf{J}_i, \quad (13)$$

where κ is the thermal conductivity of the mixture. h_i is the specific enthalpy of species i :

$$h_i = c_{p,i} T, \quad (14)$$

where $c_{p,i}$ is the specific heat capacity at constant pressure of species i .

The equations and mixing rules for the fluid properties γ , c_v , $c_{p,i}$, μ , μ_v , κ , and D_i are given in appendices B and C.

III. NUMERICAL METHODS

3D numerical experiments with adaptive mesh refinement (AMR) were conducted with the Hydrodynamics Adaptive Mesh Refinement Simulator (HAMeRS) [34] supported with Structured Adaptive Mesh Refinement Application Infrastructure (SAMRAI) library [35–39] from Lawrence Livermore National Laboratory (LLNL). The convective fluxes of the governing equations are discretized with the explicit form of sixth-order localized dissipation weighted compact nonlinear scheme (WCNS) [40] for shock-capturing and stabilization of solutions. Derivatives of diffusive and viscous fluxes are computed with explicit sixth-order finite difference schemes in non-conservative form. A third order total variation diminishing Runge–Kutta (RK-TVD) scheme [41] is employed for the time advancement with a convective Courant–Friedrichs–Lewy (CFL) number of 0.5 and a diffusive CFL number of 0.25. The regions for adaptive mesh refinement are identified with a gradient sensor on pressure field and a wavelet sensor [42] on density field to detect shock waves and mixing regions, respectively. An additional sensor based on mass fractions is also used to assist the detection of mixing regions.

IV. INITIAL CONDITIONS AND COMPUTATIONAL DOMAIN

The 3D case set-up in our previous paper [31], with physical transport coefficients for the gases considered, is chosen in this work. In this set-up, the shock-induced mixing problem is simulated in a numerical shock tube with a cross-sectional area of 2.5 cm \times 2.5 cm. A planar shock wave of Mach number $Ma = 1.45$ is initialized in a sulphur hexafluoride (SF_6) region, with the Rankine–Hugoniot jump conditions to interact with a diffuse interface between SF_6 and air. Multi-mode perturbation expressed in the following equation is imposed on the interface:

$$S(y, z) = A \sum_m \cos\left(\frac{2\pi m}{L_{yz}} y + \phi_m\right) \cos\left(\frac{2\pi m}{L_{yz}} z + \psi_m\right), \quad (15)$$

where $L_{yz} = 2.5$ cm. The perturbation has 11 modes with wavenumber m between 20 and 30 in each transverse direction. Constant amplitude $A = \sqrt{2} \times 0.01$ mm is used for each mode and random phase shifts ϕ_m and ψ_m between 0 and 2π are introduced to each mode to prevent summing up of harmonic modes. ϕ_m and ψ_m of each mode are given in the Supplemental Material.

The computational domain and initial conditions are shown in figure 1. Boundaries are periodic in the transverse directions and reflective boundary conditions are applied at the end wall. The length of domain is chosen to be large enough such that no waves leave the open-sided boundary during the simulations. The pre-shocked gases are

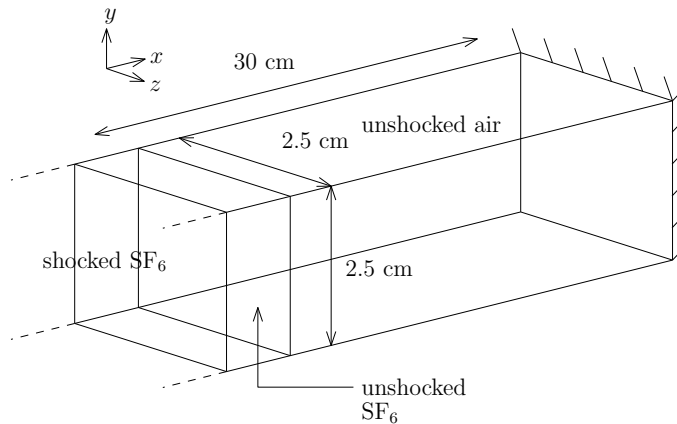


FIG. 1. Schematic diagram of initial flow field and computational domain.

TABLE I. Initial conditions of the post-shock state and the pre-shock states of the light- and heavy-gas sides.

Quantity	Post-shock SF ₆	Pre-shock SF ₆	Air
ρ (kg m ⁻³)	11.97082	5.972866	1.145601
p (Pa)	218005.4	101325.0	101325.0
T (K)	319.9084	298.0	298.0
u (m s ⁻¹)	98.93441	0	0

stationary initially and have temperature $T = 298$ K and pressure $p = 101325$ Pa. Table I shows the initial conditions of gases in different portions of the domain. The initial Atwood number $At = (\rho_{\text{SF}_6} - \rho_{\text{air}})/(\rho_{\text{SF}_6} + \rho_{\text{air}})$ across the interface is 0.68.

The shock wave is initially positioned at a location such that the shock-interface interaction first happens at 0.05 ms after the numerical simulations have started. $t = 0$ is set at the instance when the shock interacts with the interface. Since the simulations are initiated in the heavy-light gas setting, the shock wave is transmitted to the light-fluid side and a rarefaction wave is reflected back to the heavy-fluid side. After hitting the wall, the transmitted shock is reflected back towards the interface when it hits the end wall and this causes the re-shock of the interface. Since the shock arrives at the interface from the light-fluid side this time, a transmitted shock and a refracted shock are generated. The refracted shock will lead to a second re-shock. The end time of the simulations is chosen at $t = 1.75$ ms when the second re-shock is just about to happen, as the grid resolution requirements become too large to accurately capture this flow stage. Figure 2 shows the space-time (x - t) diagram for different features in a one-dimensional (1D) flow representation. This problem was studied in the previous work [31] with both two-dimensional (2D) and 3D simulations. In this work, results from a higher resolution 3D AMR simulation are studied for the second-moment analysis of the shock-induced variable-density instability and turbulence.

V. TRANSPORT EQUATIONS OF SECOND-MOMENTS

To get a statistical view of a chaotic or turbulent field, it is a common practice to ensemble average the governing equations. The conservative variables are decomposed into ensemble means and fluctuations through Reynolds decomposition. The Reynolds decomposition of an arbitrary variable, f , rewrites the variable as:

$$f = \bar{f} + f', \quad (16)$$

where \bar{f} and f' are the mean and fluctuation of f respectively. If the flow has homogeneous directions and the widths of domain in the homogeneous directions are sufficiently larger than the length scales of turbulent features, one can estimate the ensemble mean with mean over all homogeneous directions. For variable-density flows, after averaging the conservative variables of the governing equations it is natural to see the Favre-averaged (density-weighted-averaged) quantities. The Favre decomposition is given by:

$$f = \tilde{f} + f'', \quad (17)$$

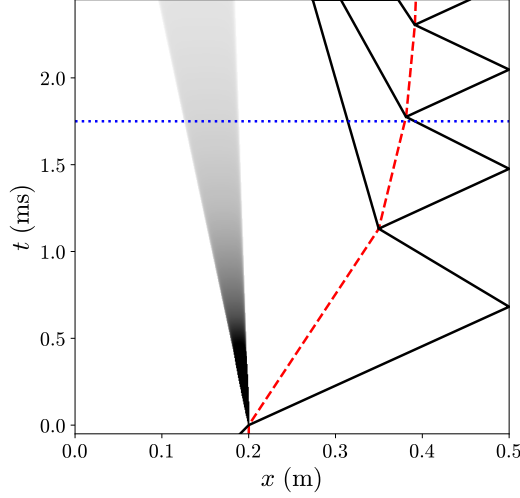


FIG. 2. x - t diagram showing the propagation of material interface, shock waves, and rarefaction. Red dashed line: material interface; black lines: shock waves; gray region: rarefaction. The blue dotted line indicates the end time of the simulations.

where $\tilde{f} = \overline{\rho f} / \bar{\rho}$. The Reynolds and Favre averages of the velocity are related with:

$$\tilde{u}_i = \bar{u}_i + a_i, \quad (18)$$

where $a_i = \overline{\rho' u_i'} / \bar{\rho}$ is the velocity associated with the turbulent mass flux $\bar{\rho} a_i$. The fluctuation, u_i' , and the Favre fluctuation, u_i'' , have similar relation as the averages:

$$u_i'' = u_i' - a_i. \quad (19)$$

If we apply averaging on the continuity equation and conservative transport equation of momentum given by equations (4) and (2) respectively, we obtain:

$$\frac{\partial \bar{\rho}}{\partial t} + \frac{\partial (\bar{\rho} \tilde{u}_k)}{\partial x_k} = 0, \quad (20)$$

$$\frac{\partial (\bar{\rho} \tilde{u}_i)}{\partial t} + \frac{\partial (\bar{\rho} \tilde{u}_k \tilde{u}_i)}{\partial x_k} = - \frac{\partial (\bar{p} \delta_{ki})}{\partial x_k} + \frac{\partial \bar{\tau}_{ki}}{\partial x_k} - \frac{\partial (\bar{\rho} \tilde{R}_{ki})}{\partial x_k}, \quad (21)$$

where \tilde{R}_{ij} is the Favre-averaged Reynolds stress tensor given by:

$$\tilde{R}_{ij} = \frac{\overline{\rho u_i'' u_j''}}{\bar{\rho}}. \quad (22)$$

The Favre-averaged Reynolds stress tensor appears as an unclosed term in the Favre-averaged transport equation of momentum. The development of the Favre-averaged Reynolds stress can be studied through its transport equations given by Besnard *et al.* [17]:

$$\underbrace{\frac{\partial \bar{\rho} \tilde{R}_{ij}}{\partial t}}_{\text{term (I)}} + \underbrace{\frac{\partial (\bar{\rho} \tilde{u}_k \tilde{R}_{ij})}{\partial x_k}}_{\text{term (II)}} = \underbrace{a_i \left(\frac{\partial \bar{p}}{\partial x_j} - \frac{\partial \bar{\tau}_{jk}}{\partial x_k} \right) + a_j \left(\frac{\partial \bar{p}}{\partial x_i} - \frac{\partial \bar{\tau}_{ik}}{\partial x_k} \right) - \bar{\rho} \tilde{R}_{ik} \frac{\partial \tilde{u}_j}{\partial x_k} - \bar{\rho} \tilde{R}_{jk} \frac{\partial \tilde{u}_i}{\partial x_k}}_{\text{term (III)}} - \underbrace{\frac{\partial (\overline{\rho u_i'' u_j'' u_k''})}{\partial x_k}}_{\text{term (IV)}} - \underbrace{\frac{\partial (\overline{u_i' p'})}{\partial x_j} - \frac{\partial (\overline{u_j' p'})}{\partial x_i} + \frac{\partial (\overline{u_i' \tau'_{jk}})}{\partial x_k} + \frac{\partial (\overline{u_j' \tau'_{ik}})}{\partial x_k}}_{\text{term (V)}} + \underbrace{p' \frac{\partial u_i'}{\partial x_j} + p' \frac{\partial u_j'}{\partial x_i} - \tau'_{jk} \frac{\partial u_i'}{\partial x_k} - \tau'_{ik} \frac{\partial u_j'}{\partial x_k}}_{\text{term (VI)}}, \quad (23)$$

where the left hand side (LHS) consists of rate of change (I) and convection (II). The right hand side (RHS) consists of production (III), turbulent transport (IV), pressure-strain redistribution (V), and dissipation (VI).

In the paper by Schwarzkopf *et al.* [20], Favre decomposition is used for the viscous stress in the Favre-averaged Reynolds stress transport equation instead of Reynolds decomposition. However, we follow the original work by Besnard *et al.* [17] to use Reynolds decomposition for the viscous stress as we believe Favre decomposition should only be applied in the advective or convective terms. The Reynolds decomposition of the viscous stress was also employed in the DNS analysis of Livescu *et al.* [43], which was later used to refine the model by Schwarzkopf *et al.* [21]. Besides, the dissipation term with Reynolds decomposition on viscous stress in the turbulent kinetic energy transport equation can be proved to be strictly negative if both shear and bulk viscosities are uniform in the domain, while that with Favre decomposition on viscous stress cannot be proved to be strictly negative. Also, note that with relation given by equation (19):

$$\frac{\partial (\overline{u'_i p'})}{\partial x_j} = \frac{\partial (\overline{u''_i p'})}{\partial x_j}, \quad (24)$$

$$\frac{\partial (\overline{u'_i \tau'_{jk}})}{\partial x_k} = \frac{\partial (\overline{u''_i \tau'_{jk}})}{\partial x_k}, \quad (25)$$

$$p' \frac{\partial u'_i}{\partial x_j} = p' \frac{\partial u''_i}{\partial x_j}, \quad (26)$$

$$\tau'_{jk} \frac{\partial u'_i}{\partial x_k} = \tau'_{jk} \frac{\partial u''_i}{\partial x_k}. \quad (27)$$

The relations above are commonly used to interchange terms in the transport equations of \tilde{R}_{ij} and k in many previous studies.

In flows where the mean is 1D, such as the numerical experiment being studied in this work (where the y and z directions are homogeneous), the transport equation of \tilde{R}_{11} can be simplified to:

$$\underbrace{\frac{\partial \tilde{\rho} \tilde{R}_{11}}{\partial t}}_{\text{term (I)}} + \underbrace{\frac{\partial (\tilde{\rho} \tilde{u} \tilde{R}_{11})}{\partial x}}_{\text{term (II)}} = \underbrace{2a_1 \left(\frac{\partial \tilde{p}}{\partial x} - \frac{\partial \tilde{\tau}_{11}}{\partial x} \right) - 2\tilde{\rho} \tilde{R}_{11} \frac{\partial \tilde{u}}{\partial x}}_{\text{term (III)}} - \underbrace{\frac{\partial (\overline{\rho u'' u'' u''})}{\partial x} - 2 \frac{\partial (\overline{u' p'})}{\partial x} + 2 \frac{\partial (\overline{u' \tau'_{11}})}{\partial x}}_{\text{term (IV)}} + \underbrace{2p' \frac{\partial u'}{\partial x}}_{\text{term (V)}} - \underbrace{2 \left(\tau'_{11} \frac{\partial u'}{\partial x} + \tau'_{12} \frac{\partial u'}{\partial y} + \tau'_{13} \frac{\partial u'}{\partial z} \right)}_{\text{term (VI)}}. \quad (28)$$

The transport equation of \tilde{R}_{22} for 1D mean flow can be reduced to:

$$\underbrace{\frac{\partial \tilde{\rho} \tilde{R}_{22}}{\partial t}}_{\text{term (I)}} + \underbrace{\frac{\partial (\tilde{\rho} \tilde{u} \tilde{R}_{22})}{\partial x}}_{\text{term (II)}} = \underbrace{- \frac{\partial (\overline{\rho v'' v'' u''})}{\partial x} + 2 \frac{\partial (\overline{v' \tau'_{21}})}{\partial x}}_{\text{term (IV)}} + \underbrace{2p' \frac{\partial v'}{\partial y}}_{\text{term (V)}} - \underbrace{2 \left(\tau'_{21} \frac{\partial v'}{\partial x} + \tau'_{22} \frac{\partial v'}{\partial y} + \tau'_{23} \frac{\partial v'}{\partial z} \right)}_{\text{term (VI)}}. \quad (29)$$

Note that there is no production term (term (III)) in the transport equation of \tilde{R}_{22} . The transport equation of \tilde{R}_{33} is similar. In the present flow, the Reynolds shear stress components, \tilde{R}_{12} , \tilde{R}_{13} , and \tilde{R}_{23} , are statistically zero.

The transport equation of the turbulent kinetic energy per unit mass, $k = \tilde{R}_{ii}/2$, can be simply obtained by taking half of the trace of the Reynolds stress tensor transport equation. For 1D mean flow, it has the following form:

$$\underbrace{\frac{\partial \tilde{\rho} k}{\partial t}}_{\text{term (I)}} + \underbrace{\frac{\partial (\tilde{\rho} \tilde{u} k)}{\partial x}}_{\text{term (II)}} = \underbrace{a_1 \left(\frac{\partial \tilde{p}}{\partial x} - \frac{\partial \tilde{\tau}_{11}}{\partial x} \right) - \tilde{\rho} \tilde{R}_{11} \frac{\partial \tilde{u}}{\partial x}}_{\text{term (III)}} - \underbrace{\frac{1}{2} \frac{\partial (\overline{\rho u''_i u''_i u''})}{\partial x} - \frac{\partial (\overline{u' p'})}{\partial x} + \frac{\partial (\overline{u'_i \tau'_{i1}})}{\partial x}}_{\text{term (IV)}} + \underbrace{p' \frac{\partial u'_i}{\partial x_i}}_{\text{term (V)}} - \underbrace{\tau'_{ij} \frac{\partial u'_i}{\partial x_j}}_{\text{term (VI)}}, \quad (30)$$

where the left hand side (LHS) consists of rate of change (I) and convection (II). The right hand side (RHS) consists of production (III), turbulent transport (IV), pressure-dilatation (V), and dissipation (VI).

The velocity associated with the turbulent mass flux, a_i , in the mean flow pressure gradient terms only appears in variable-density or/and compressible flows. It is an important term for understanding the energetics in these kinds of flows, as the mean pressure gradient multiplied by it is the agent for the transfer of mean kinetic energy into turbulent kinetic energy. Correct modeling of a_i can also help us close the Reynolds stress transport equations. The transport equation of turbulent mass flux $\bar{\rho}a_i$ is given by [17]:

$$\underbrace{\frac{\partial(\bar{\rho}a_i)}{\partial t}}_{\text{term (I)}} + \underbrace{\frac{\partial(\bar{\rho}\tilde{u}_k a_i)}{\partial x_k}}_{\text{term (II)}} = \underbrace{b \left(\frac{\partial \bar{p}}{\partial x_i} - \frac{\partial \bar{\tau}_{ki}}{\partial x_k} \right) - \tilde{R}_{ik} \frac{\partial \bar{\rho}}{\partial x_k}}_{\text{term (III)}} + \underbrace{\bar{\rho} \frac{\partial(a_k a_i)}{\partial x_k} - \bar{\rho} a_k \frac{\partial \bar{u}_i}{\partial x_k}}_{\text{term (IV)}} - \underbrace{\bar{\rho} \frac{\partial(\overline{\rho' u'_i u'_k / \bar{\rho}})}{\partial x_k}}_{\text{term (V)}} + \underbrace{\bar{\rho} \left(\frac{1}{\rho} \right)' \left(\frac{\partial p'}{\partial x_i} - \frac{\partial \tau'_{ik}}{\partial x_k} \right) + \bar{\rho} \varepsilon_{a_i}}_{\text{term (VI)}}, \quad (31)$$

where the LHS consists of rate of change (I) and convection (II). The RHS contains production (III), redistribution (IV), turbulent transport (V), and destruction (VI). Also,

$$\varepsilon_{a_i} = -\overline{u'_i \frac{\partial u'_k}{\partial x_k}}. \quad (32)$$

Note that ε_{a_i} is ignored in the work by Besnard *et al.* [17] and in many turbulence models. However, ε_{a_i} was shown to be non-negligible at early times in the evolution of constant acceleration RTI [43]. Here, it is also found that ε_{a_i} is significant in the budgets at different times before re-shock for the flow being studied in this work.

For 1D mean flow, the transport equation of $\bar{\rho}a_1$ can be simplified to:

$$\underbrace{\frac{\partial(\bar{\rho}a_1)}{\partial t}}_{\text{term (I)}} + \underbrace{\frac{\partial(\bar{\rho}\tilde{u}a_1)}{\partial x}}_{\text{term (II)}} = \underbrace{b \left(\frac{\partial \bar{p}}{\partial x} - \frac{\partial \bar{\tau}_{11}}{\partial x} \right) - \tilde{R}_{11} \frac{\partial \bar{\rho}}{\partial x}}_{\text{term (III)}} + \underbrace{\bar{\rho} \frac{\partial(a_1 a_1)}{\partial x} - \bar{\rho} a_1 \frac{\partial \bar{u}}{\partial x}}_{\text{term (IV)}} - \underbrace{\bar{\rho} \frac{\partial(\overline{\rho' u' u' / \bar{\rho}})}{\partial x}}_{\text{term (V)}} + \underbrace{\bar{\rho} \left(\frac{1}{\rho} \right)' \left(\frac{\partial p'}{\partial x} - \frac{\partial \tau'_{11}}{\partial x} - \frac{\partial \tau'_{12}}{\partial y} - \frac{\partial \tau'_{13}}{\partial z} \right) + \bar{\rho} \varepsilon_{a_1}}_{\text{term (VI)}}. \quad (33)$$

Note that a_2 and a_3 for 1D mean flow are statistically equal to zero. The density-specific-volume covariance, $b = -\overline{\rho'(1/\rho)'}$, mediates the turbulent mass flux production mechanism. The component of production term, $b\bar{p}_{,1}$, is crucial to the prediction of the rate of change of turbulent mass flux and requires the modeling of b .

The transport equation of b was first derived by Besnard *et al.* [17] in the following advection form with the Reynolds-averaged velocity:

$$\frac{\partial b}{\partial t} + \bar{u}_k b_{,k} = -\frac{b+1}{\bar{\rho}} (\bar{\rho} a_k)_{,k} - \bar{\rho} \left(\left(\frac{1}{\rho} \right)' u'_k \right)_{,k} - 2\bar{\rho} \varepsilon_b, \quad (34)$$

where

$$\varepsilon_b = \overline{\left(\frac{1}{\rho} \right)' \frac{\partial u'_k}{\partial x_k}}. \quad (35)$$

In Schwarzkopf *et al.* [20], the transport equation of $\bar{\rho}b$ in the conservative form is derived from equation (34) with the averaged mixture continuity equation (equation (4)) as:

$$\underbrace{\frac{\partial \bar{\rho}b}{\partial t}}_{\text{term (I)}} + \underbrace{\frac{\partial(\bar{\rho}\tilde{u}_k b)}{\partial x_k}}_{\text{term (II)}} = \underbrace{-2(b+1)a_k \frac{\partial \bar{\rho}}{\partial x_k}}_{\text{term (III)}} + \underbrace{+2\bar{\rho}a_k \frac{\partial b}{\partial x_k}}_{\text{term (IV)}} + \underbrace{\bar{\rho}^2 \frac{\partial(\overline{\rho'(1/\rho)' u'_k / \bar{\rho}})}{\partial x_k}}_{\text{term (V)}} + \underbrace{+2\bar{\rho}^2 \varepsilon_b}_{\text{term (VI)}}, \quad (36)$$

where the LHS consists of rate of change (I) and convection (II). The RHS consists of production (III), redistribution (IV), turbulent transport (V), and destruction (VI). For 1D mean flow, the transport equation of $\bar{\rho}b$ can be simplified

to:

$$\underbrace{\frac{\partial(\bar{\rho}b)}{\partial t}}_{\text{term (I)}} + \underbrace{\frac{\partial(\bar{\rho}\tilde{u}b)}{\partial x}}_{\text{term (II)}} = \underbrace{-2(b+1)a_1\frac{\partial\bar{\rho}}{\partial x}}_{\text{term (III)}} + \underbrace{+2\bar{\rho}a_1\frac{\partial b}{\partial x}}_{\text{term (IV)}} + \underbrace{\bar{\rho}^2\frac{\partial(\overline{(\rho'/\rho)'u'/\bar{\rho}})}{\partial x}}_{\text{term (V)}} + \underbrace{+2\bar{\rho}^2\varepsilon_b}_{\text{term (VI)}}. \quad (37)$$

The transport equation of $\bar{\rho}b$ in conservative form shown above instead of that in advection form is studied in this work. Conservative form of b transport equation was also considered in the DNS analysis of Livescu *et al.* [43].

VI. GRID SENSITIVITY ANALYSIS

In this section, the quality of simulations is studied through grid sensitivity analysis. Table II shows the grid settings used for the problem. There are totally three levels of grids with two levels of mesh refinement in all grid settings. The refinement ratios in each direction from the base level to second level and from second level to the finest level are 1:2 and 1:4 respectively. Four different grid settings are tested, with number of grid points in the transverse directions increasing from 32 points (grid B) to 256 points (grid E) on the base level. The finest level for the largest mesh resolution case has a grid spacing of 12.2 μm . With this grid spacing, there are around 68 grid points across the smallest wavelength among the initial modes. The 3D simulations with grids B-D were first presented in [31], but the new simulation using the grid E settings presented here is a higher grid resolution compared to those runs and provides more accurate statistical results. This ultra-high resolution simulation has cell counts surpassing 4.5 billion, as shown in appendix A. Figure 3 presents visualizations of the mixing layer at different times with grid E.

TABLE II. Different grids used for the grid sensitivity study. Three levels of grids with 1:8 overall refinement ratio are used in all cases.

Grid	Base grid resolution	Refinement ratios	Finest grid spacing (μm)
B	$640 \times 32 \times 32$	1:2, 1:4	97.7
C	$1280 \times 64 \times 64$	1:2, 1:4	48.8
D	$2560 \times 128 \times 128$	1:2, 1:4	24.4
E	$5120 \times 256 \times 256$	1:2, 1:4	12.2

The grid sensitivities of the integral mixing width W and the domain-integrated quantities of interests ($\bar{\rho}a_1$, $\bar{\rho}b$, $\bar{\rho}\tilde{R}_{11}$, $\bar{\rho}\tilde{R}_{22}$, $\bar{\rho}\tilde{R}_{33}$, and $\bar{\rho}k$) in the transport equations of second moment quantities are examined in this section. The mixing width is defined as:

$$W = \int 4\bar{X}_{\text{SF}_6} (1 - \bar{X}_{\text{SF}_6}) dx. \quad (38)$$

The mixing width estimates the characteristic length of the mixing layer due to the entrainment of fluids. Note that since $\bar{\rho}\tilde{R}_{22}$ and $\bar{\rho}\tilde{R}_{33}$ are statistically identical, the grid sensitivity of $\bar{\rho}(\tilde{R}_{22} + \tilde{R}_{33})/2$ is studied instead.

Figure 4 compares the time evolution of the statistical quantities computed on different grids. From the figure, it can be seen that mixing width, integrals of $\bar{\rho}a_1$, $\bar{\rho}b$, and $\bar{\rho}\tilde{R}_{11}$ are well grid-converged for the entire simulation with the highest resolution grid. The grid sensitivity of the integral of $\bar{\rho}(\tilde{R}_{22} + \tilde{R}_{33})/2$ is higher than other quantities before re-shock but its contribution to the integral of turbulent kinetic energy, $\bar{\rho}k$, is order of magnitude smaller than that of $\bar{\rho}\tilde{R}_{11}$. Thus, the integral of $\bar{\rho}k$ is also grid-converged reasonably well at all times.

As the statistical quantities of interests computed on the finest resolution grid (grid E) show very small grid sensitivity throughout the simulation when compared with those from the next finest resolution grid (grid D), only results from grid E are presented and discussed in the remaining sections.

VII. ANALYSIS OF SECOND-MOMENTS

The importance of the second-moments: $\bar{\rho}a_1$, $\bar{\rho}b$, $\bar{\rho}\tilde{R}_{11}$, $\bar{\rho}\tilde{R}_{22}$, and $\bar{\rho}\tilde{R}_{33}$ to close the Favre-averaged momentum equation of the mixture is discussed earlier. In this section, the time evolution of the spatial profiles of different second-moments is studied in details.

At each impulsive acceleration such as at first shock and re-shock, the advection velocity of the mixing layer changes abruptly. However, the advection speed of mixing layer between impulsive accelerations is essentially constant in time

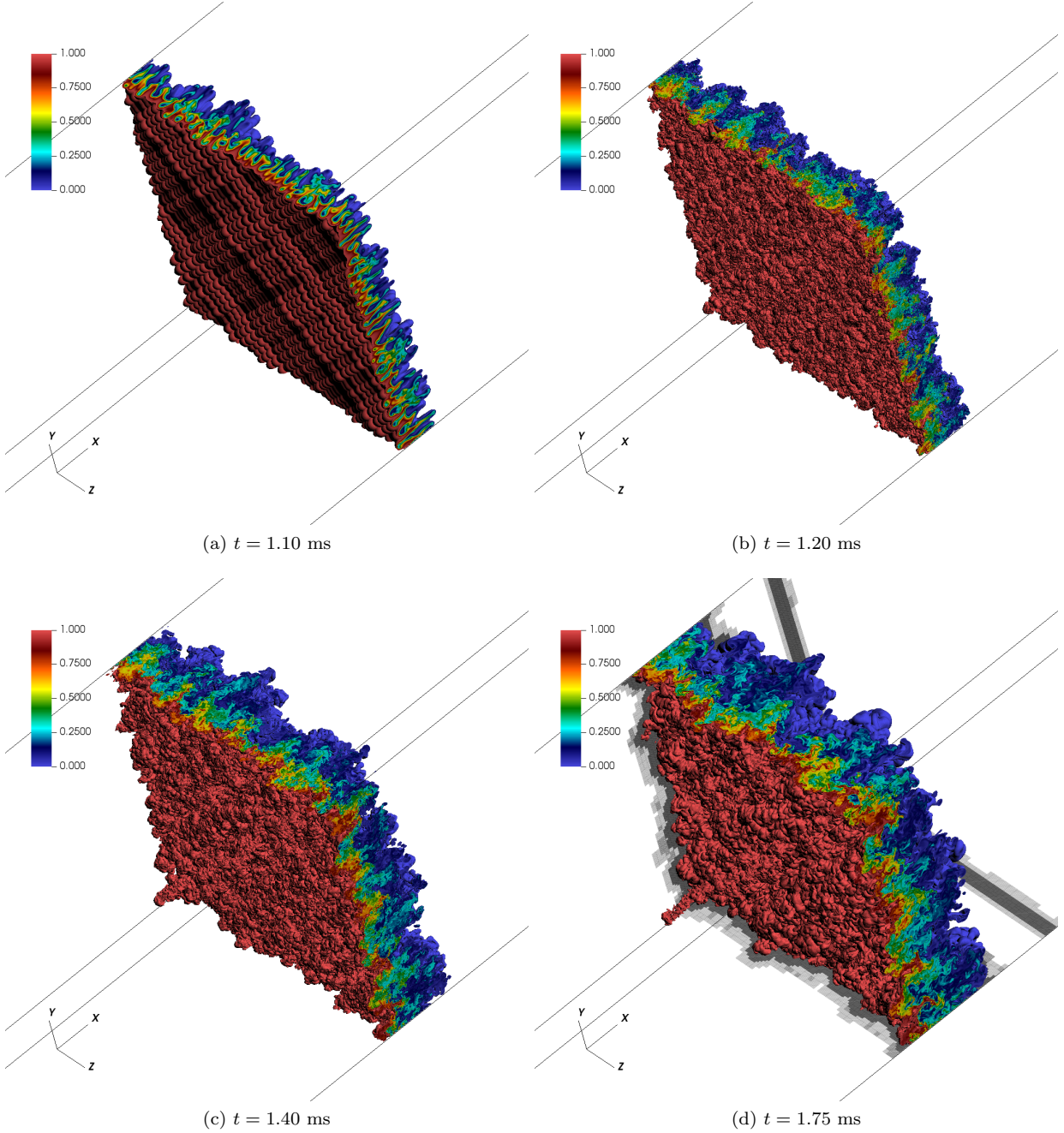


FIG. 3. Isovolumes of the SF_6 mole fraction, X_{SF_6} , at different times in the numerical shock tube with grid E. The colorbar indicates the value of X_{SF_6} . The first and second (last) refinement levels of AMR grid are shown on the side walls of the domain for the plot at $t = 1.75$ ms. The grid is refined at regions containing the mixing layer and shocks. Note that shocks are not visualized with the mole fraction isovolumes.

and is close to that given by the solutions of the 1D flow representation, U_i . Besides, the mean velocity across the mixing layer is observed to be quite uniform. Therefore, in a moving reference frame with speed U_i relative to the simulation reference frame, $\bar{u} \approx 0$ and $\tilde{u} \approx a_1$ statistically. All of the 1D spatial profiles of second-moments discussed in this section are plotted in the moving frame of the mixing layer with the \tilde{x} coordinate system. In other words, the x coordinate is shifted as:

$$\tilde{x}(x, t) = x - x_i(t), \quad (39)$$

where x_i is the location of the interface from the solutions of the 1D flow representation.

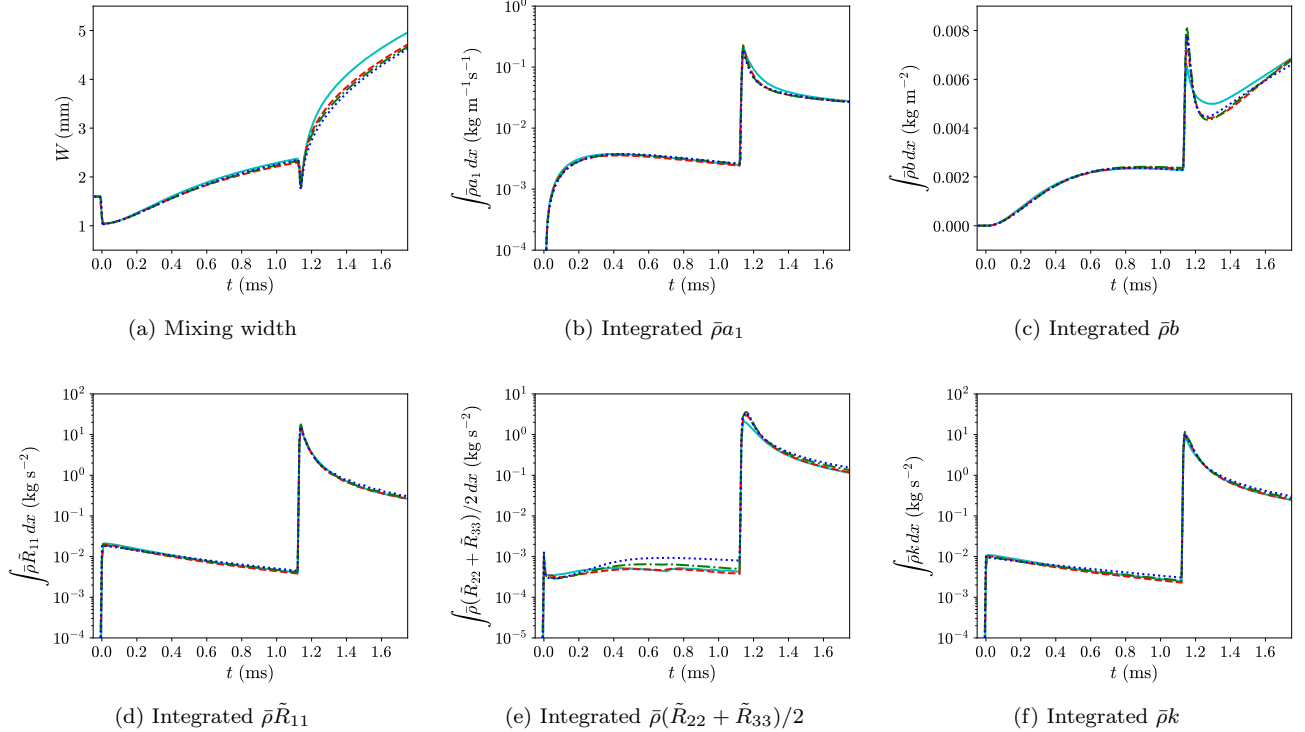


FIG. 4. Grid sensitivities of mixing width and second moment statistics. Cyan solid line: grid B; red dashed line: grid C; green dash-dotted line: grid D; blue dotted line: grid E.

A. Mean density and turbulent mass flux

The mean density profiles at different times in the moving frame of the mixing layer are shown in figure 5. The density profiles become wider over time after first shock and re-shock due to the mixing caused by the RMI. While not shown here, the density profiles collapse reasonably well at late times after both first shock and re-shock when they are normalized with the mixing width W . Similar collapse for the mole fraction profiles was also reported in the previous work [31].

Figure 6 compares the profiles of $\bar{\rho}a_1$ at different times before re-shock and after re-shock. The study of turbulent mass flux, $\bar{\rho}a_1$, and the velocity associated with turbulent mass flux, a_1 , is very important for understanding variable-density effects in the current problem and modeling similar types of flows. From the figure, it can be seen that there is a sudden rise in $\bar{\rho}a_1$, followed by its decay after each shock event. It can also be noticed that at late times after first-shock and re-shock, $\bar{\rho}a_1$ peaks at a position slightly to the heavier fluid side (slightly negative \tilde{x}). This suggests that there is a fixed point at the same location in the mean density profiles at late times, which can be deduced from equation (20). The fixed point can be seen and verified from the mean density profiles shown in figure 5.

B. Density-specific-volume covariance

The density-specific-volume covariance, b , mediates the turbulent mass flux production mechanism. It can also be viewed as a metric for the homogeneity of mixing. b is a non-negative quantity and $b = 0$ corresponds to fluids that are homogeneously mixed. Figure 7 displays the profiles of b at different times before and after re-shock. It can be seen that the magnitude of the peak of b at late times after first shock and re-shock remains quite unchanged. b can also be expressed as a sum of a series of density probability density function (PDF) moments [44]:

$$b = \frac{\overline{\rho'^2}}{\bar{\rho}^2} \left[1 - i_\rho \frac{\overline{\rho'^3}}{(\bar{\rho}^2)^{3/2}} + i_\rho^2 \frac{\overline{\rho'^4}}{(\bar{\rho}^2)^2} - i_\rho^3 \frac{\overline{\rho'^5}}{(\bar{\rho}^2)^{5/2}} + \dots \right], \quad (40)$$

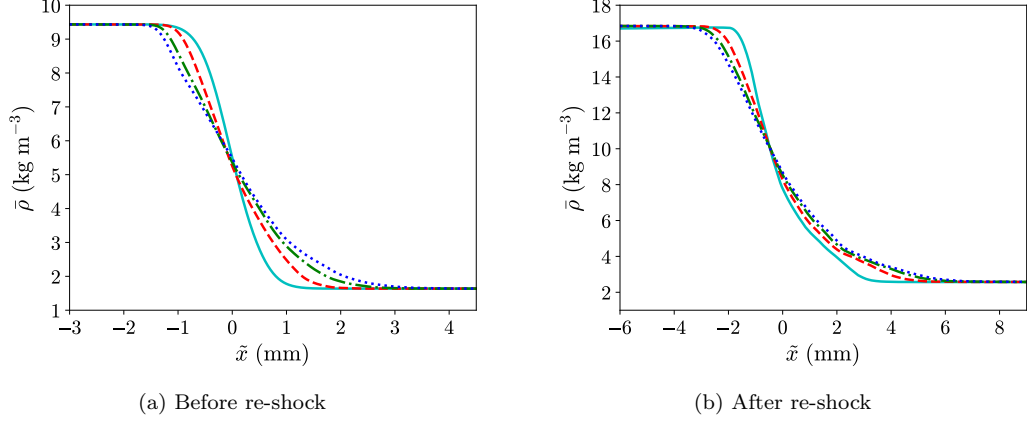


FIG. 5. Profiles of mean density, $\bar{\rho}$, at different times. Cyan solid line in (a): $t = 0.05$ ms; red dashed line in (a): $t = 0.40$ ms; green dash-dotted line in (a): $t = 0.75$ ms; blue dotted line in (a): $t = 1.10$ ms. Cyan solid line in (b): $t = 1.20$ ms; red dashed line in (b): $t = 1.40$ ms; green dash-dotted line in (b): $t = 1.60$ ms; blue dotted line in (b): $t = 1.75$ ms.

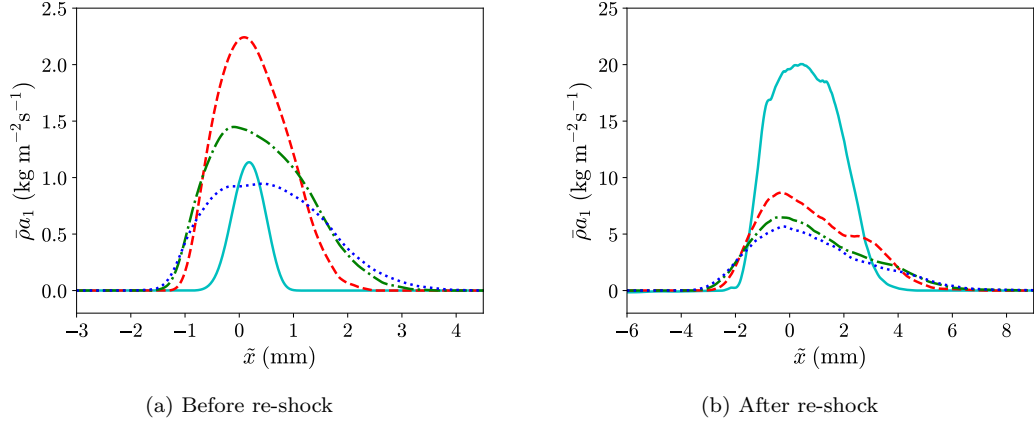


FIG. 6. Profiles of turbulent mass flux, $\bar{\rho}a_1$, at different times. Cyan solid line in (a): $t = 0.05$ ms; red dashed line in (a): $t = 0.40$ ms; green dash-dotted line in (a): $t = 0.75$ ms; blue dotted line in (a): $t = 1.10$ ms. Cyan solid line in (b): $t = 1.20$ ms; red dashed line in (b): $t = 1.40$ ms; green dash-dotted line in (b): $t = 1.60$ ms; blue dotted line in (b): $t = 1.75$ ms.

where $i_\rho = (\overline{\rho'^2})^{1/2}/\bar{\rho}$. If i_ρ is very small, the equation reduces to the Boussinesq relation:

$$b \approx \frac{\overline{\rho'^2}}{\bar{\rho}^2}. \quad (41)$$

The ratio of left hand side (density-specific-volume covariance) and right hand side (square of density intensity) of equation (41) can be used to test the Boussinesq approximation, where the corresponding component in turbulent mass flux production can be approximated with density variance instead of b . Boussinesq approximation is valid when the ratio is close to one. Figure 8 shows the variations in the ratio across the mixing region at different times. It can be seen that the ratio varies from 0.5 to 2.5. The ratio is, in general, larger than one on heavier fluid side and smaller than one on lighter fluid side, because of the skewness of the density field. The peaks are located at the edges of the mixing layers, which indicates that variable-density effects are larger at the edges than the central part of the mixing layer.

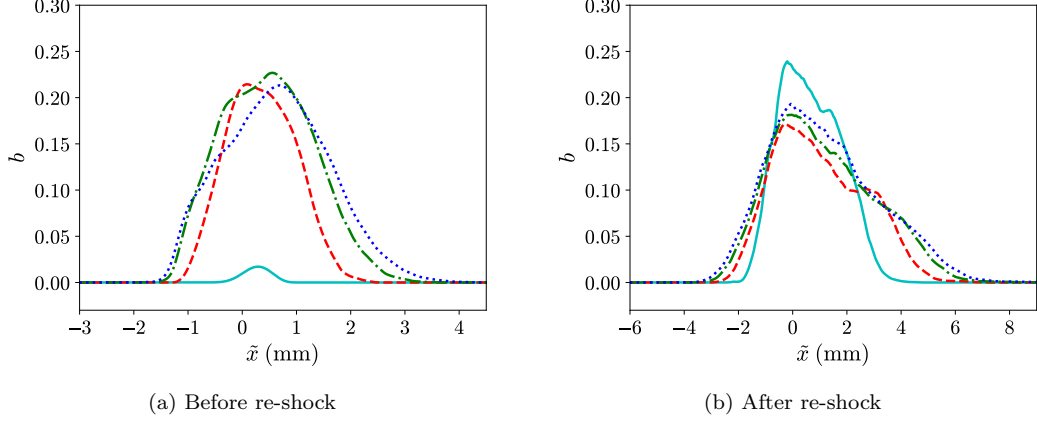


FIG. 7. Profiles of density-specific-volume covariance, b , at different times. Cyan solid line in (a): $t = 0.05$ ms; red dashed line in (a): $t = 0.40$ ms; green dash-dotted line in (a): $t = 0.75$ ms; blue dotted line in (a): $t = 1.10$ ms. Cyan solid line in (b): $t = 1.20$ ms; red dashed line in (b): $t = 1.40$ ms; green dash-dotted line in (b): $t = 1.60$ ms; blue dotted line in (b): $t = 1.75$ ms.

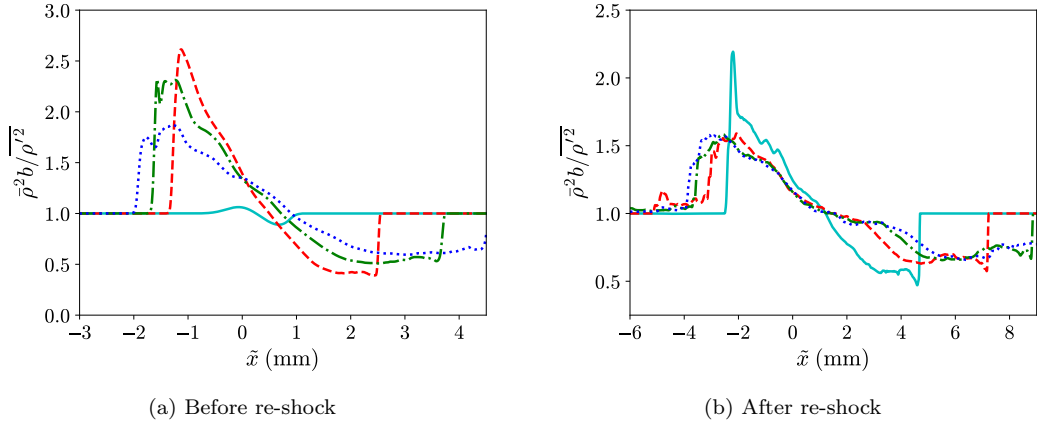


FIG. 8. Profiles of ratio of density-specific-volume covariance to square of density intensity at different times. Cyan solid line in (a): $t = 0.05$ ms; red dashed line in (a): $t = 0.40$ ms; green dash-dotted line in (a): $t = 0.75$ ms; blue dotted line in (a): $t = 1.10$ ms. Cyan solid line in (b): $t = 1.20$ ms; red dashed line in (b): $t = 1.40$ ms; green dash-dotted line in (b): $t = 1.60$ ms; blue dotted line in (b): $t = 1.75$ ms.

C. Favre-averaged Reynolds stress

The Favre-averaged Reynolds stress tensor, \tilde{R}_{ij} , appears as an unclosed term in the averaged transport equation of momentum given by equation (21). Figures 9 and 10 respectively show the profiles of Favre-averaged Reynolds normal stress components in the streamwise and transverse directions at different times. Immediately after first shock, there is generation of the Favre-averaged Reynolds normal stress in the mixing region. However, Favre-averaged Reynolds normal stress component in the streamwise direction is much larger than those in the transverse directions at that instance. As time advances, the ratios of the component in the streamwise direction to those in the transverse directions decreases, but the Reynolds normal stress fields are still very anisotropic at the moment just before re-shock. The streamwise Favre-averaged Reynolds normal stress component peaks at the lighter fluid side because of smaller inertia to entrain the fluid from nonlinear convection. After re-shock, the Favre-averaged Reynolds normal stress fields become more isotropic but there is still more contribution to turbulent kinetic energy from the streamwise Reynolds normal stress component until the end of simulation. The comparison of different Favre-averaged Reynolds stress components is shown in figure 11. All Reynolds shear stress components should be statistically zero but figure 11 shows that the Reynolds shear stress components are not absolutely zero. This is due to some lack of full statistical convergence, but the values are all negligible compared to the Reynolds normal stress components.

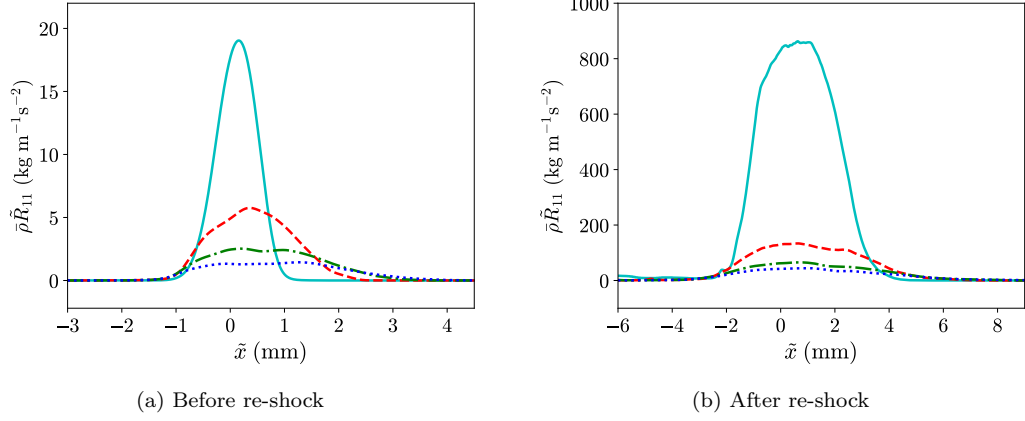


FIG. 9. Profiles of Reynolds normal stress component in streamwise direction multiplied by mean density, $\tilde{\rho}\tilde{R}_{11}$, at different times. Cyan solid line in (a): $t = 0.05$ ms; red dashed line in (a): $t = 0.40$ ms; green dash-dotted line in (a): $t = 0.75$ ms; blue dotted line in (a): $t = 1.10$ ms. Cyan solid line in (b): $t = 1.20$ ms; red dashed line in (b): $t = 1.40$ ms; green dash-dotted line in (b): $t = 1.60$ ms; blue dotted line in (b): $t = 1.75$ ms.

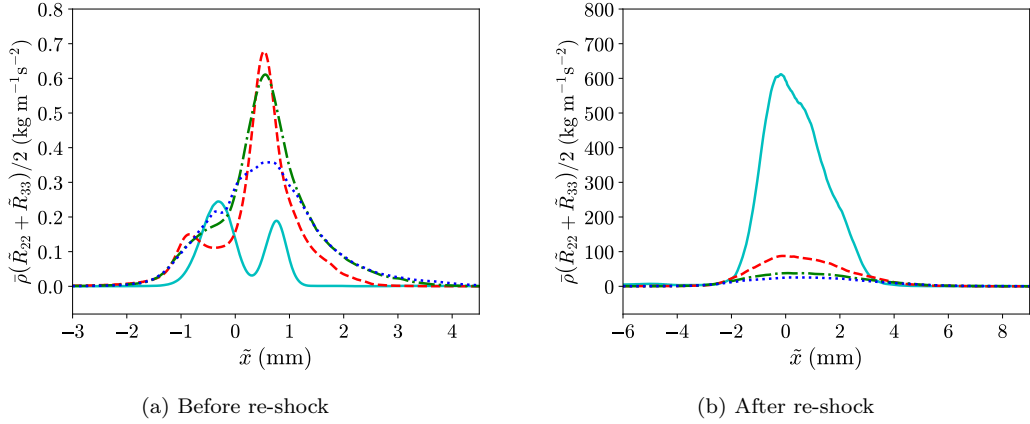


FIG. 10. Profiles of mean Reynolds normal stress component in transverse directions multiplied by mean density, $\tilde{\rho}(\tilde{R}_{11} + \tilde{R}_{22})/2$, at different times. Cyan solid line in (a): $t = 0.05$ ms; red dashed line in (a): $t = 0.40$ ms; green dash-dotted line in (a): $t = 0.75$ ms; blue dotted line in (a): $t = 1.10$ ms. Cyan solid line in (b): $t = 1.20$ ms; red dashed line in (b): $t = 1.40$ ms; green dash-dotted line in (b): $t = 1.60$ ms; blue dotted line in (b): $t = 1.75$ ms.

The Favre-averaged Reynolds stress \tilde{R}_{ij} can be decomposed as:

$$\tilde{R}_{ij} = \frac{\overline{\rho u'_i u'_j}}{\tilde{\rho}} - a_i a_j = \underbrace{\overline{u'_i u'_j}}_{\text{term (I)}} + \underbrace{\frac{\overline{\rho' u'_i u'_j}}{\tilde{\rho}}}_{\text{term (II)}} - \underbrace{a_i a_j}_{\text{term (III)}},$$

where term (I), $\overline{u'_i u'_j}$, is the definition of Reynolds stress tensor for single-species incompressible flows. Figure 12 compares the contributions of different terms to \tilde{R}_{11} at different times. We can see from the plots that, although the profile of \tilde{R}_{11} is very similar to $\overline{u' u'}$, the contributions of the other two terms, especially $\overline{\rho' u' u'}/\tilde{\rho}$, are not negligible. Figure 13 shows the discrepancies between \tilde{R}_{11} and the two different approximations: (i) $\overline{u' u'}$ and (ii) $\overline{\rho u' u'}/\tilde{\rho} = \overline{u' u'} + \overline{\rho' u' u'}/\tilde{\rho}$, through the ratios of \tilde{R}_{11} to the approximations. It can be seen that \tilde{R}_{11} cannot be well represented by $\overline{u' u'}$ alone, as the ratio can vary from 0.6 to 2.2. This is associated with the strong variable-density effects of the flow. If $\overline{\rho' u' u'}/\tilde{\rho}$ is included to approximate \tilde{R}_{11} , there is a huge improvement in the approximation, as the ratio now only varies from 0.85 to 1. Although this suggests that a_1 has small contribution to the decomposition of \tilde{R}_{11} , this does not mean that a_1 has insignificant effect on the time evolution of \tilde{R}_{11} . Thus, it is shown in the

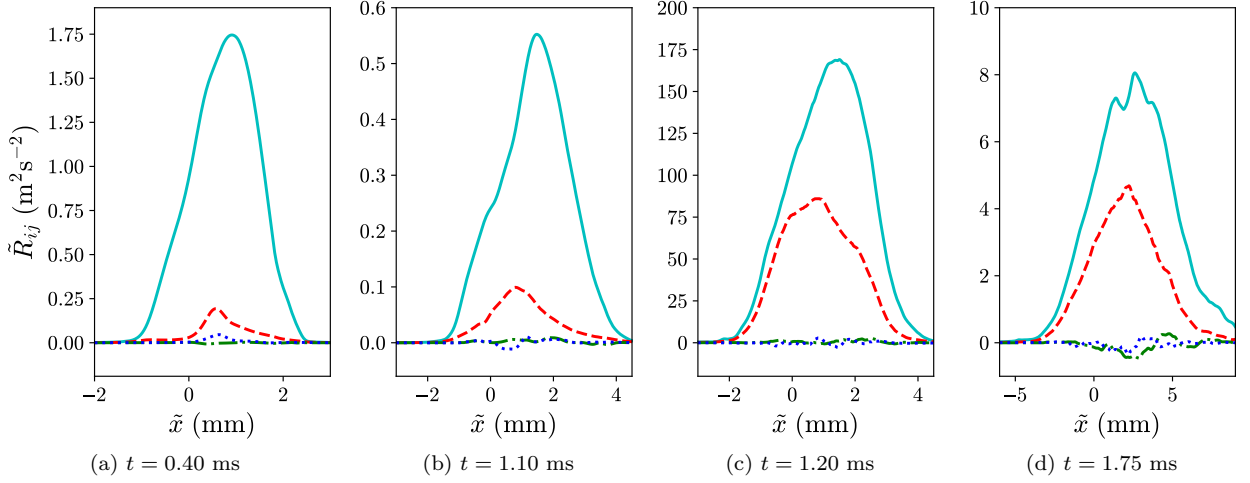


FIG. 11. Comparison of Reynolds stress components at different times. Cyan solid line: \tilde{R}_{11} ; red dashed line: $(\tilde{R}_{22} + \tilde{R}_{33})/2$; green dash-dotted line: $(\tilde{R}_{12} + \tilde{R}_{13})/2$; blue dotted line: \tilde{R}_{23} .

next few sections that a_1 plays an important role in the transport equation of \tilde{R}_{11} through the component of the production term, $2a_1\bar{p}_{,1}$.

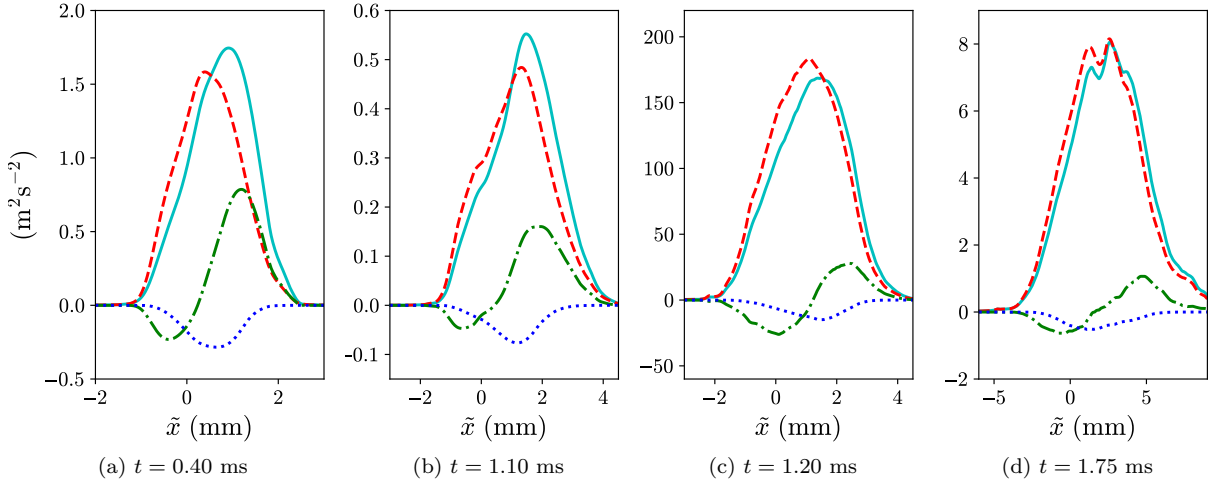


FIG. 12. Decomposition of Reynolds normal stress component in streamwise direction, $\tilde{\rho}\tilde{R}_{11}$, at different times. Cyan solid line: \tilde{R}_{11} ; red dashed line: $\overline{u'u'}$; green dash-dotted line: $\overline{\rho'u'u'}/\bar{\rho}$; blue dotted line: $-a_1^2$.

VIII. BUDGETS OF SECOND-MOMENTS BEFORE RE-SHOCK

In this section, the budgets of second-moments: $\bar{\rho}a_1$, $\bar{\rho}b$, and $\bar{\rho}\tilde{R}_{11}$ across the mixing layer before re-shock are studied. All budgets are computed with the results from the highest resolution (grid E) simulation, for which the flow fields are well-resolved. The budgets are studied in the \tilde{x} coordinate system, equivalent to studying the budgets in the moving reference frame of the mixing layer. The convective terms in all of the transport equations of second-moments for 1D mean flow have the common form of $[\bar{\rho}\tilde{u}(\cdot)]_{,1}$, where (\cdot) represents any of the second-moments (a_1 , b , or R_{ij}). Using equation (18), the convective terms can be rewritten as:

$$\frac{\partial \bar{\rho}\tilde{u}(\cdot)}{\partial x} = \underbrace{\frac{\partial \bar{\rho}\tilde{u}(\cdot)}{\partial x}}_{\text{term (I)}} + \underbrace{\frac{\partial \bar{\rho}a_1(\cdot)}{\partial x}}_{\text{term (II)}}, \quad (42)$$

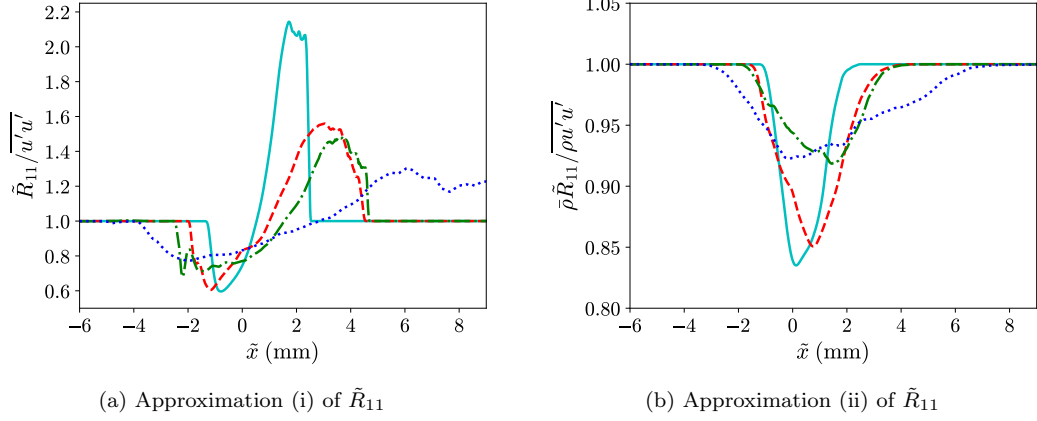


FIG. 13. Ratios of Reynolds normal stress component in streamwise direction, $\bar{\rho}\tilde{R}_{11}$, to different approximations at different times. Cyan solid line: $t = 0.40$ ms; red dashed line: $t = 1.10$ ms; green dash-dotted line: $t = 1.20$ ms; blue dotted line: $t = 1.75$ ms.

where term (I) is the convection due to mean velocity and term (II) is the convection due to velocity associated with turbulent mass flux. In the moving reference frame of the mixing layer, it is observed that \bar{u} is quite uniformly close to zero compared to \bar{R}_{11} . Hence term (I) can be ignored. The convective term is assumed fully represented by $[\bar{\rho}a_1(\cdot)]_{,1}$.

A. Turbulent mass flux

Figure 14 shows the spatial profiles of different terms in the RHS of the transport equation of streamwise component of turbulent mass flux, $\bar{\rho}a_1$, given by equation (33) at different times before re-shock across the mixing layer. The negative of the convective term of the same equation due to a_1 is also shown in the figure. The rate of change term in the LHS of the transport equation is computed by restarting the simulation at different checkpoints. In each plot, the magenta dotted line shows the profile of the residue, which is defined as the subtraction of the net RHS term from the net LHS term in the simulation frame. Therefore, the residue represents the numerical effect or SGS effect on the rate of change of conservative variable, i.e. $\bar{\rho}a_1$ here. From both figures 14(a) and 14(b), it can be seen that the residue is virtually zero across the mixing layer at different times before re-shock. Note that the thin black solid line in each plot is the sum of all of the RHS terms including the residue and the negative of the convection term due to a_1 , thus it represents the rate of change of $\bar{\rho}a_1$ in the moving frame of the mixing layer.

From figure 14, we can see that production, destruction, and turbulent transport terms play important roles in the budget equation at the chosen times before re-shock: $t = 0.40$ ms and $t = 1.10$ ms. At the two chosen times, the instability is in the nonlinear growth regime. In the interior part of the mixing layer, the production, destruction, and turbulent transport terms are the dominant terms. The production term is strictly positive in the mixing region and peaks around the middle part of the mixing region. Nonetheless, both destruction and turbulent transport terms are negative in the interior part of mixing layer to offset the effect from production. Overall, the combined effect of the destruction and turbulent transport terms is larger than that of the production and hence the peak of turbulent mass flux reduces over time. At the edges of mixing layer, all RHS terms are small except the turbulent transport term, which is positive and responsible for the spreading of the turbulent mass flux. The magnitudes of redistribution and convective terms are smaller than those of other terms but still have significant effects at different times before re-shock. The two terms have similar magnitudes but opposite signs. The convective term decreases the turbulent mass flux on the heavier fluid side and increases that on the lighter fluid side. The redistribution term has opposite effect to bring the turbulent mass flux from the light fluid side back to the heavy fluid side.

The composition of the production term is shown in figure 15. It can be seen that at the chosen times before re-shock, the production term is mainly contributed from the component, $-\tilde{R}_{11}\bar{\rho}_{,1}$, which is observed to be strictly positive. Another constituent, $b\bar{p}_{,1}$, has smaller contribution to the overall term and $-b\bar{\tau}_{11,1}$ is negligible. $b\bar{p}_{,1}$ transfers the turbulent mass flux from the heavier fluid side to the lighter fluid side, although this effect is hidden in the overall production term. As for the destruction term, figure 16 shows that all three constituents ($\bar{\rho}(1/\rho)'p'_{,1}$, $-\bar{\rho}(1/\rho)'\tau'_{1i,i}$, and $\bar{\rho}\varepsilon_{a_1}$) have similar magnitudes and are generally negative at the two times before re-shock.

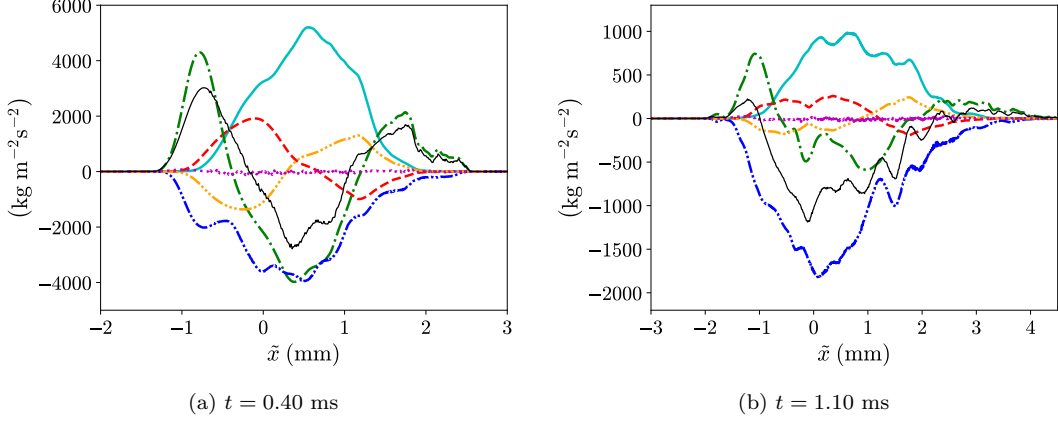


FIG. 14. Budgets of turbulent mass flux component in streamwise direction, $\bar{\rho}a_1$, given by equation (33), at different times before re-shock. Cyan solid line: production (III); red dashed line: redistribution (IV); green dash-dotted line: turbulent transport (V); blue dash-dot-dotted line: destruction (VI); orange dash-triple-dotted line: negative of convection due to streamwise velocity associated with turbulent mass flux; magenta dotted line: residue; thin black solid line: summation of all terms (rate of change in the moving frame).

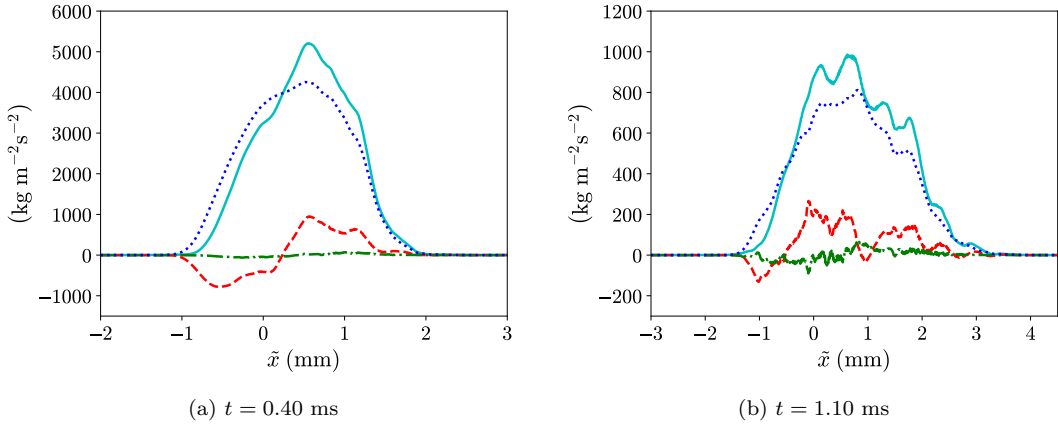


FIG. 15. Compositions of production term in the transport equation of turbulent mass flux component in streamwise direction, $\bar{\rho}a_1$, at different times before re-shock. Cyan solid line: overall production; red dashed line: $b\bar{p}_{,1}$; green dash-dotted line: $-b\bar{\tau}_{1,1}$; blue dotted line: $-\bar{R}_{11}\bar{\rho}_{,1}$.

B. Density-specific-volume covariance

Figure 17 shows the spatial profiles of different budget terms that appear in the transport equation of $\bar{\rho}b$ given by equation (37) before re-shock. Similar to the plots for budgets of the turbulent mass flux, the magenta dotted line represents the residue, which is the difference between the net LHS and net RHS terms. As seen in figures 17(a) and 17(b), the residue is basically zero. This means that there is negligible numerical effect due to insufficient spatial grid spacing on the time evolution of $\bar{\rho}b$ before re-shock. Before re-shock, the production, turbulent transport, and destruction terms are dominant, but the redistribution and convective terms cannot be neglected in the transport equation of $\bar{\rho}b$ either. Although there is a positive effect in the interior part of the mixing layer from the production term to increase $\bar{\rho}b$, the effect is offset by both turbulent transport and destruction terms. The net rate of change of $\bar{\rho}b$ around the peak of b is small so the peak of b (similarly for $\bar{\rho}b$) remains relatively constant in time compared to peaks of other second-moments, which is shown earlier. At the edges of mixing layer, most terms are small except the turbulent transport term, which is positive that leads $\bar{\rho}b$ and b to spread. Both redistribution term and convection term due to a_1 redistribute $\bar{\rho}b$ across the layer but they have exactly opposite effects (redistribution term brings $\bar{\rho}$ from the lighter fluid side to the heavy fluid side and convective term vice versa). They also have similar shapes and

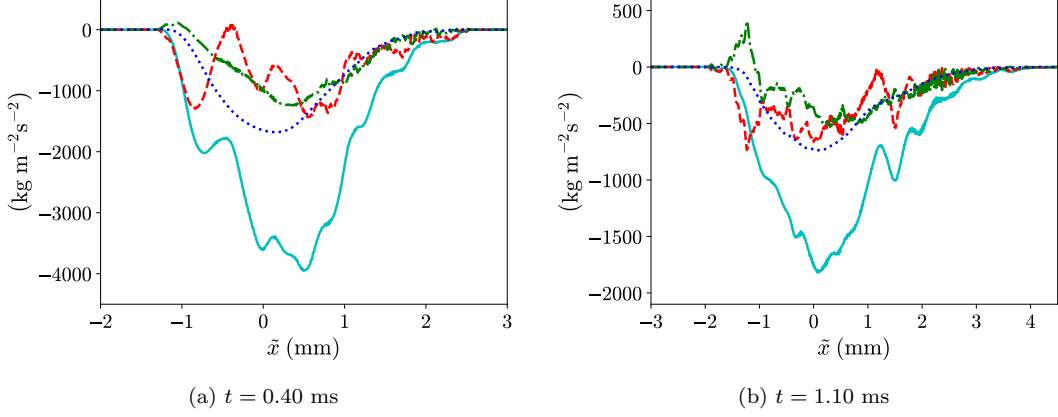


FIG. 16. Compositions of destruction term in the transport equation of turbulent mass flux component in streamwise direction, $\bar{\rho}a_1$, at different times before re-shock. Cyan solid line: overall destruction; red dashed line: $\bar{\rho}(1/\rho)'p'_{,1}$; green dash-dotted line: $-\bar{\rho}(1/\rho)'\tau'_{1,i,i}$; blue dotted line: $\bar{\rho}\varepsilon_{a_1}$.

thus roughly cancel effects from each other. A similar cancellation is also shown earlier for the corresponding terms in the budgets of $\bar{\rho}a_1$.

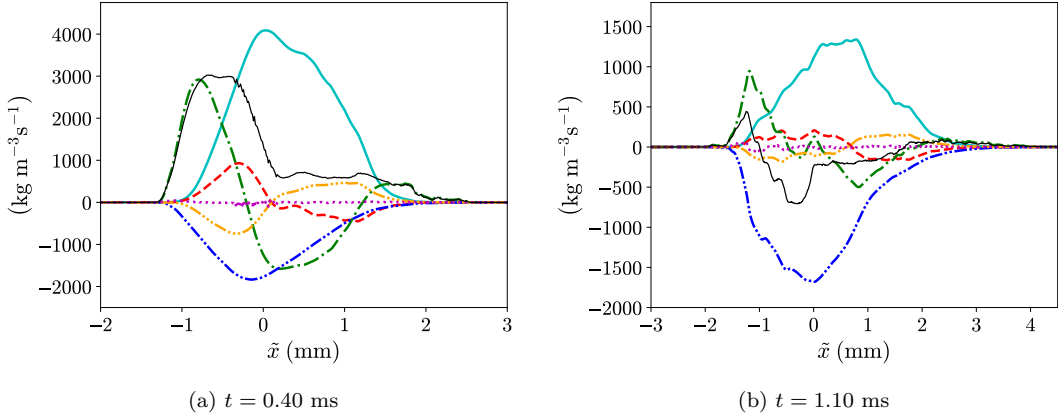


FIG. 17. Budgets of density-specific-volume covariance multiplied by mean density, $\bar{\rho}b$, given by equation (37), at different times before re-shock. Cyan solid line: production (III); red dashed line: redistribution (IV); green dash-dotted line: turbulent transport (V); blue dash-dot-dotted line: destruction (VI); orange dash-triple-dotted line: negative of convection due to streamwise velocity associated with turbulent mass flux; magenta dotted line: residue; thin black solid line: summation of all terms (rate of change in the moving frame).

C. Favre-averaged Reynolds stress

In figure 18, the spatial profiles of different terms in the transport equation of $\bar{\rho}\tilde{R}_{11}$ given by equation (28) at different times before re-shock are compared. Similar to the budgets of other second-moments, the residue due to spatial discretization is negligible before re-shock. The critical terms in the interior mixing region that cause the peak of $\bar{\rho}\tilde{R}_{11}$ (slightly inclined to the lighter fluid side) to decrease before re-shock are the pressure-strain redistribution, turbulent transport, and dissipation terms. The production and convection terms are quite positive there but their combined effect is smaller than that from the negative terms. In general, both production and convection terms are positive on the lighter fluid side and negative on the heavier fluid side. These two terms transport $\bar{\rho}\tilde{R}_{11}$ from the heavier fluid side to the lighter fluid side. On the other hand, the turbulent transport term helps bring $\bar{\rho}\tilde{R}_{11}$ from the

lighter fluid side to the heavier fluid side and more importantly it is also responsible for the spreading of the statistical quantity at the edges of the mixing layer.

Figure 19 shows the composition of production term before re-shock. It can be seen that both $2a_1\bar{p}_{,1}$ and $-2\bar{\rho}\tilde{R}_{11}\tilde{u}_{,1}$ have large contributions to the production term, while the remaining component, $-2a_1\bar{\tau}_{11,1}$, is negligible. The composition of the turbulent transport term is shown in figure 20. All three constituents: $-(\overline{\rho u'' u'' u''})_{,1}$, $-2(\overline{u' p'})_{,1}$, and $2(\overline{u' \tau'_{11}})_{,1}$ have significant contributions to the term before re-shock. The triple correlation component, $-(\overline{\rho u'' u'' u''})_{,1}$, is the root of the spreading effect while $-2(\overline{u' p'})_{,1}$ and $2(\overline{u' \tau'_{11}})_{,1}$ have opposite effects for the transfer of $\bar{\rho}\tilde{R}_{11}$ between heavy and light fluid regions. $-2(\overline{u' p'})_{,1}$ transports $\bar{\rho}\tilde{R}_{11}$ from heavier fluid side to lighter fluid side and vice versa for $2(\overline{u' \tau'_{11}})_{,1}$.

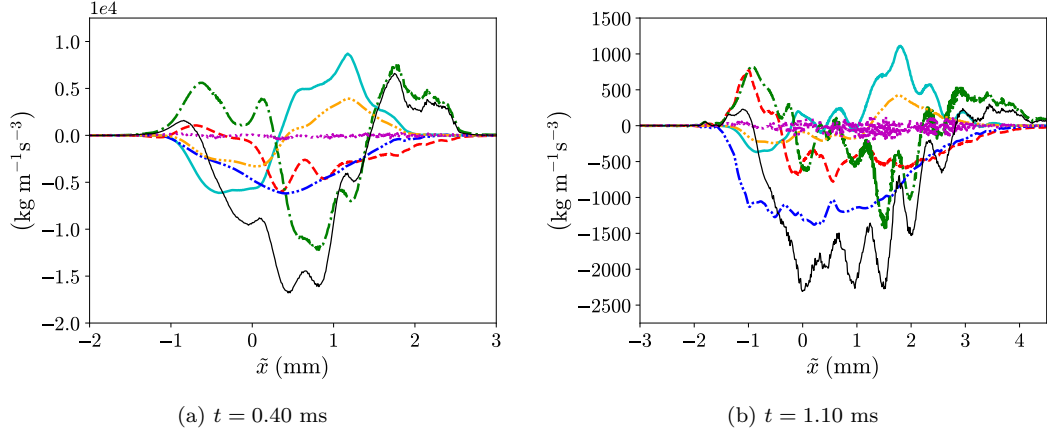


FIG. 18. Budgets of Reynolds normal stress component in streamwise direction multiplied by mean density, $\bar{\rho}\tilde{R}_{11}$, given by equation (28), at different times before re-shock. Cyan solid line: production (III); red dashed line: press-strain redistribution (V); green dash-dotted line: turbulent transport (IV); blue dash-dot-dotted line: dissipation (VI); orange dash-triple-dotted line: negative of convection due to streamwise velocity associated with turbulent mass flux; magenta dotted line: residue; thin black solid line: summation of all terms (rate of change in the moving frame).

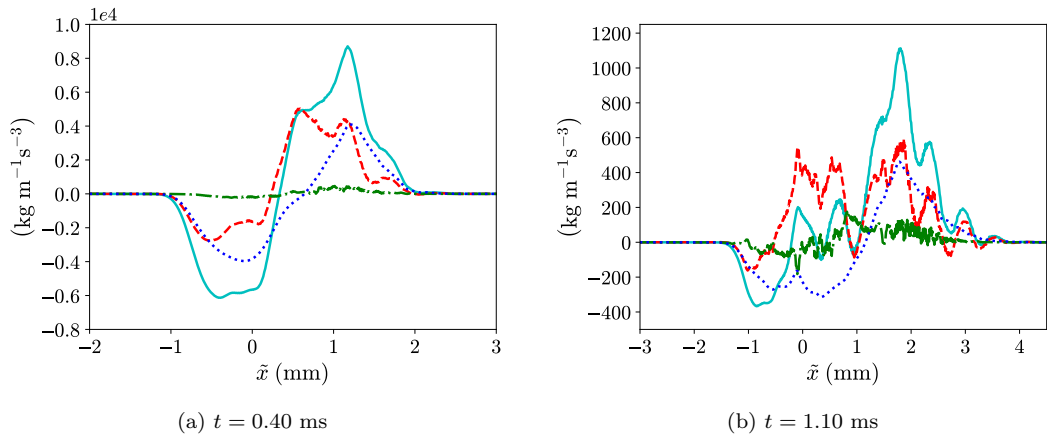


FIG. 19. Compositions of production term in the transport equation of Reynolds normal stress component in streamwise direction multiplied by mean density, $\bar{\rho}\tilde{R}_{11}$, at different times before re-shock. Cyan solid line: overall production; red dashed line: $2a_1\bar{p}_{,1}$; green dash-dotted line: $-2a_1\bar{\tau}_{11,1}$; blue dotted line: $-2\bar{\rho}\tilde{R}_{11}\tilde{u}_{,1}$.

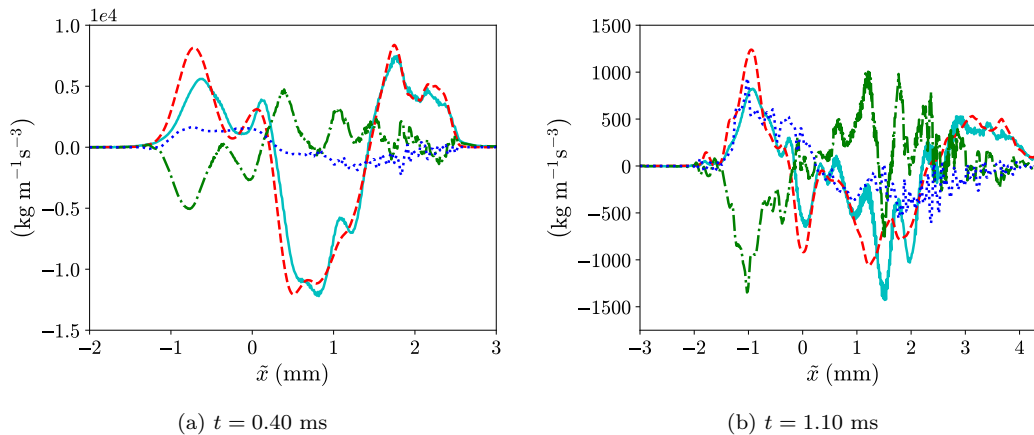


FIG. 20. Compositions of turbulent transport term in the transport equation of Reynolds normal stress component in streamwise direction multiplied by mean density, $\bar{\rho}R_{11}$, at different times before re-shock. Cyan solid line: overall turbulent transport; red dashed line: $-(\rho u''u''u'')_{,1}$; green dash-dotted line: $-2(u'p')_{,1}$; blue dotted line: $2(u'\tau'_{11})_{,1}$.

IX. FILTERED NAVIER-STOKES EQUATIONS AND TRANSPORT EQUATIONS OF LARGE-SCALE SECOND-MOMENTS

In the present flow, mixing transition follows after the mixing layer is traversed by the reflected shock. This re-shock deposits baroclinic vorticity at both large and small scales and rapid breakdown to fully-developed turbulence ensues. The eddies span a wide range of length scales, where the largest and smallest eddies are estimated to be at scales of $O(1000)$ and $O(1)$ microns respectively [31]. The small scales of the turbulent flow after re-shock are not well-resolved even in the highest resolution simulation. Therefore, it is more appropriate to study the transport equations of large-scale second-moments derived from the filtered Navier-Stokes equations at times after re-shock. The idea is that numerical regularization is assumed to have negligible effects on large-scale second-moments that only contain scales from zero wavenumber to a cut-off wavenumber imposed by a filter that is considerably larger than the grid cut-off wavenumber. The analysis of the transport equations of the large-scale second-moments is useful for (1) studying the mechanisms of the generation, destruction and spreading of the large-scale turbulent features in shock-induced variable-density turbulence, (2) examining the self-similarity of the turbulent flow, and (3) understanding how the subfilter-scale stress can affect the resolved large-scale turbulent features in LES.

While the effects of filtering on the buoyancy-driven variable-density turbulence have been studied in [45], the focus in current work is different. The analysis proposed here mainly focuses on the effects of SFS stress on large-scale statistical quantities resolved on a lower resolution grid and aims at gaining insight into the suitability of using LES data for analyzing RANS-based models.

The filtering operation of a variable, $f = f(x_i, t)$, with filter width, ℓ , can be defined as:

$$\langle f(x_i, t) \rangle_\ell = \int_{-\infty}^{\infty} f(x'_i, t) G(x'_i, x_i) dx'_i, \quad (43)$$

where $\langle f \rangle_\ell$ is the filtered value and $G(x'_i, x_i)$ denotes a filter function. In variable-density flows, it is also convenient to define the Favre-filtered value, $\langle f \rangle_L$, as:

$$\langle f \rangle_L = \frac{\langle \rho f \rangle_\ell}{\langle \rho \rangle_\ell}. \quad (44)$$

If we apply the filter on the mixture continuity equation and transport equation of momentum given by equations (4) and (2) respectively, we can obtain the filtered Navier-Stokes equations:

$$\frac{\partial \langle \rho \rangle_\ell}{\partial t} + \frac{\partial (\langle \rho \rangle_\ell \langle u_k \rangle_L)}{\partial x_k} = 0, \quad (45)$$

$$\frac{\partial (\langle \rho \rangle_\ell \langle u_i \rangle_L)}{\partial t} + \frac{\partial (\langle \rho \rangle_\ell \langle u_k \rangle_L \langle u_i \rangle_L)}{\partial x_k} = -\frac{\partial (\langle p \rangle_\ell \delta_{ki})}{\partial x_k} + \frac{\partial \langle \tau_{ki} \rangle_\ell}{\partial x_k} - \frac{\partial \tau_{ki}^{SFS}}{\partial x_k}, \quad (46)$$

where commutation terms are assumed to be negligible. τ_{ij}^{SFS} is the SFS stress tensor given by:

$$\tau_{ij}^{SFS} = \langle \rho u_i u_j \rangle_\ell - \langle \rho \rangle_\ell \langle u_i \rangle_L \langle u_j \rangle_L. \quad (47)$$

If averaging is further applied on the filtered continuity equation and transport equation of momentum given by equations (45) and (46) respectively, the following Favre-averaged filtered Navier–Stokes equations are obtained:

$$\frac{\partial \overline{\langle \rho \rangle}_\ell}{\partial t} + \frac{\partial \left(\overline{\langle \rho \rangle}_\ell \widetilde{\langle u_k \rangle}_L \right)}{\partial x_k} = 0, \quad (48)$$

$$\frac{\partial \left(\overline{\langle \rho \rangle}_\ell \widetilde{\langle u_i \rangle}_L \right)}{\partial t} + \frac{\partial \left(\overline{\langle \rho \rangle}_\ell \widetilde{\langle u_k \rangle}_L \widetilde{\langle u_i \rangle}_L \right)}{\partial x_k} = - \frac{\partial \left(\overline{\langle p \rangle}_\ell \delta_{ki} \right)}{\partial x_k} + \frac{\partial \langle \tau_{ki} \rangle_\ell}{\partial x_k} - \frac{\partial \overline{\tau_{ki}^{SFS}}}{\partial x_k} - \frac{\partial \left(\overline{\langle \rho \rangle}_\ell \widetilde{R}_{L,ki} \right)}{\partial x_k}, \quad (49)$$

where Reynolds and Favre decompositions on the filtered variables ($\langle f \rangle_\ell$ or $\langle f \rangle_L$) are involved:

$$\langle f \rangle_{\ell/L} = \overline{\langle f \rangle}_{\ell/L} + \langle f \rangle'_{\ell/L} = \widetilde{\langle f \rangle}_{\ell/L} + \langle f \rangle''_{\ell/L}, \quad (50)$$

and $\widetilde{R}_{L,ij}$ is the large-scale Favre-averaged Reynolds stress tensor computed with the filtered density and velocity fields and is given by:

$$\widetilde{R}_{L,ij} = \frac{\overline{\langle \rho \rangle}_\ell \langle u_i \rangle''_L \langle u_j \rangle''_L}{\overline{\langle \rho \rangle}_\ell}. \quad (51)$$

In a 1D mean flow, the transport equation of $\overline{\langle \rho \rangle}_\ell \widetilde{R}_{L,11}$ is given by:

$$\begin{aligned} & \underbrace{\frac{\partial \left(\overline{\langle \rho \rangle}_\ell \widetilde{R}_{L,11} \right)}{\partial t}}_{\text{term (I)}} + \underbrace{\frac{\partial \left(\overline{\langle \rho \rangle}_\ell \widetilde{\langle u \rangle}_L \widetilde{R}_{L,11} \right)}{\partial x}}_{\text{term (II)}} = \underbrace{2a_{L,1} \left(\frac{\partial \overline{\langle p \rangle}_\ell}{\partial x} - \frac{\partial \overline{\langle \tau_{11} \rangle}_\ell}{\partial x} + \frac{\partial \overline{\tau_{11}^{SFS}}}{\partial x} \right)}_{\text{term (III)}} - 2 \overline{\langle \rho \rangle}_\ell \widetilde{R}_{L,11} \frac{\partial \widetilde{\langle u \rangle}_L}{\partial x} \\ & - \underbrace{\frac{\partial \left(\overline{\langle \rho \rangle}_\ell \langle u \rangle''_L \langle u \rangle''_L \right)}{\partial x}}_{\text{term (IV)}} - 2 \underbrace{\frac{\partial \left(\langle u \rangle'_L \langle p \rangle'_\ell \right)}{\partial x}}_{\text{term (IV)}} + 2 \underbrace{\frac{\partial \left(\langle u \rangle'_L \langle \tau_{11} \rangle'_\ell \right)}{\partial x}}_{\text{term (IV)}} - 2 \underbrace{\frac{\partial \left(\langle u \rangle'_L \tau_{11}^{SFS'} \right)}{\partial x}}_{\text{term (IV)}} + \underbrace{2 \overline{\langle p \rangle}'_\ell \frac{\partial \langle u \rangle'_L}{\partial x}}_{\text{term (V)}} \\ & - 2 \underbrace{\left(\langle \tau_{11} \rangle'_\ell \frac{\partial \langle u \rangle'_L}{\partial x} + \langle \tau_{12} \rangle'_\ell \frac{\partial \langle u \rangle'_L}{\partial y} + \langle \tau_{13} \rangle'_\ell \frac{\partial \langle u \rangle'_L}{\partial z} \right)}_{\text{term (VI)}} + 2 \underbrace{\left(\tau_{11}^{SFS'} \frac{\partial \langle u \rangle'_L}{\partial x} + \tau_{12}^{SFS'} \frac{\partial \langle u \rangle'_L}{\partial y} + \tau_{13}^{SFS'} \frac{\partial \langle u \rangle'_L}{\partial z} \right)}_{\text{term (VI)}}, \end{aligned} \quad (52)$$

where the left hand side (LHS) consists of rate of change (I) and convection (II). The right hand side (RHS) consists of production (III), turbulent transport (IV), pressure-strain redistribution (V), and dissipation (VI). $a_{L,i} = \overline{\langle \rho \rangle}'_\ell \langle u_i \rangle'_L / \overline{\langle \rho \rangle}_\ell$ is the velocity associated with the large-scale turbulent mass flux $\overline{\langle \rho \rangle}'_\ell a_{L,i} = \overline{\langle \rho \rangle}'_\ell \langle u_i \rangle'_L$ computed on filtered fields.

The transport equation of $\overline{\langle \rho \rangle}_\ell \widetilde{R}_{L,22}$ for 1D mean flow can be reduced to:

$$\begin{aligned} & \underbrace{\frac{\partial \left(\overline{\langle \rho \rangle}_\ell \widetilde{R}_{L,22} \right)}{\partial t}}_{\text{term (I)}} + \underbrace{\frac{\partial \left(\overline{\langle \rho \rangle}_\ell \widetilde{\langle u \rangle}_L \widetilde{R}_{L,22} \right)}{\partial x}}_{\text{term (II)}} = \underbrace{\frac{\partial \left(\overline{\langle \rho \rangle}_\ell \langle v \rangle''_L \langle v \rangle''_L \right)}{\partial x}}_{\text{term (IV)}} + 2 \underbrace{\frac{\partial \left(\langle v \rangle'_L \langle \tau_{21} \rangle'_\ell \right)}{\partial x}}_{\text{term (IV)}} - 2 \underbrace{\frac{\partial \left(\langle v \rangle'_L \tau_{21}^{SFS'} \right)}{\partial x}}_{\text{term (IV)}} + \underbrace{2 \overline{\langle p \rangle}'_\ell \frac{\partial \langle v \rangle'_L}{\partial y}}_{\text{term (V)}} \\ & - 2 \underbrace{\left(\langle \tau_{21} \rangle'_\ell \frac{\partial \langle v \rangle'_L}{\partial x} + \langle \tau_{22} \rangle'_\ell \frac{\partial \langle v \rangle'_L}{\partial y} + \langle \tau_{23} \rangle'_\ell \frac{\partial \langle v \rangle'_L}{\partial z} \right)}_{\text{term (VI)}} + 2 \underbrace{\left(\tau_{21}^{SFS'} \frac{\partial \langle v \rangle'_L}{\partial x} + \tau_{22}^{SFS'} \frac{\partial \langle v \rangle'_L}{\partial y} + \tau_{23}^{SFS'} \frac{\partial \langle v \rangle'_L}{\partial z} \right)}_{\text{term (VI)}}. \end{aligned} \quad (53)$$

The transport equation of $\overline{\langle \rho \rangle}_\ell \widetilde{R}_{L,33}$ is similar.

The large-scale turbulent kinetic energy per unit mass is defined as $k_L = \widetilde{R}_{L,ii}/2$. The transport equation of $\langle \overline{\rho} \rangle_\ell k_L$ can be obtained by taking half of the trace of the transport equation of $\langle \overline{\rho} \rangle_\ell \widetilde{R}_{L,ij}$. In 1D mean flow, it has the following form:

$$\begin{aligned}
\underbrace{\frac{\partial (\langle \overline{\rho} \rangle_\ell k_L)}{\partial t}}_{\text{term (I)}} + \underbrace{\frac{\partial (\langle \overline{\rho} \rangle_\ell \widetilde{u}'_L k_L)}{\partial x}}_{\text{term (II)}} &= \underbrace{a_{L,1} \left(\frac{\partial \langle \overline{p} \rangle_\ell}{\partial x} - \frac{\partial \langle \overline{\tau_{11}} \rangle_\ell}{\partial x} + \frac{\partial \overline{\tau_{11}^{SFS}}}{\partial x} \right)}_{\text{term (III)}} - \underbrace{\langle \overline{\rho} \rangle_\ell \widetilde{R}_{L,11} \frac{\partial \widetilde{u}'_L}{\partial x}}_{\text{term (IV)}} \\
\underbrace{\frac{1}{2} \frac{\partial (\langle \overline{\rho} \rangle_\ell \langle u_i \rangle_L'' \langle u_i \rangle_L'' \langle u \rangle_L'')}{\partial x}}_{\text{term (IV)}} - \underbrace{\frac{\partial (\langle u \rangle_L' \langle p \rangle_\ell')}{\partial x}}_{\text{term (V)}} + \underbrace{\frac{\partial (\langle u_i \rangle_L' \langle \tau_{i1} \rangle_\ell')}{\partial x}}_{\text{term (VI)}} - \underbrace{\frac{\partial (\langle u_i \rangle_L' \tau_{i1}^{SFS'})}{\partial x}}_{\text{term (VI)}} \\
&+ \underbrace{\langle p \rangle_\ell' \frac{\partial \langle u_i \rangle_L'}{\partial x_i}}_{\text{term (V)}} - \underbrace{\langle \tau_{ij} \rangle_\ell' \frac{\partial \langle u_i \rangle_L'}{\partial x_j}}_{\text{term (VI)}} + \underbrace{\tau_{ij}^{SFS'} \frac{\partial \langle u_i \rangle_L'}{\partial x_j}}_{\text{term (VI)}},
\end{aligned} \tag{54}$$

where the left hand side (LHS) consists of rate of change (I) and convection (II). The right hand side (RHS) consists of production (III), turbulent transport (IV), pressure-dilatation (V), and dissipation (VI). Note that term (III) represents the transfer of energy between $\langle \overline{\rho} \rangle_\ell k_L$ and the the mean kinetic energy computed from filtered fields, $K_L = \overline{\langle \rho \rangle_\ell \widetilde{u}'_L \langle u_i \rangle_L'}/2$. Besides, the combination of $-\langle u_i \rangle_L' \tau_{i1}^{SFS'}$ and $\tau_{ij}^{SFS'} \frac{\partial \langle u_i \rangle_L'}{\partial x_j}$ contributes to the transfer of energy between $\langle \overline{\rho} \rangle_\ell k_L$ and the mean SFS turbulent kinetic energy, $\tau_{ii}^{SFS'}/2$.

In 1D mean flow, the transport equation of large-scale turbulent mass flux component in streamwise direction, $\langle \overline{\rho} \rangle_\ell a_{L,1}$, can be simplified to:

$$\begin{aligned}
\underbrace{\frac{\partial (\langle \overline{\rho} \rangle_\ell a_{L,1})}{\partial t}}_{\text{term (I)}} + \underbrace{\frac{\partial (\langle \overline{\rho} \rangle_\ell \widetilde{u}'_L a_{L,1})}{\partial x}}_{\text{term (II)}} &= \underbrace{b_L \left(\frac{\partial \langle \overline{p} \rangle_\ell}{\partial x} - \frac{\partial \langle \overline{\tau_{11}} \rangle_\ell}{\partial x} + \frac{\partial \overline{\tau_{11}^{SFS}}}{\partial x} \right)}_{\text{term (III)}} - \underbrace{\widetilde{R}_{L,11} \frac{\partial \langle \overline{\rho} \rangle_\ell}{\partial x}}_{\text{term (IV)}} \\
&+ \underbrace{\langle \overline{\rho} \rangle_\ell \frac{\partial (a_{L,1} a_{L,1})}{\partial x}}_{\text{term (IV)}} - \underbrace{\langle \overline{\rho} \rangle_\ell a_{L,1} \frac{\partial \langle \overline{u} \rangle_L}{\partial x}}_{\text{term (V)}} - \underbrace{\langle \overline{\rho} \rangle_\ell \frac{\partial (\langle \overline{\rho} \rangle_\ell' \langle u \rangle_L' \langle u \rangle_L' / \langle \overline{\rho} \rangle_\ell)}{\partial x}}_{\text{term (V)}} \\
&+ \underbrace{\langle \overline{\rho} \rangle_\ell \left(\frac{1}{\langle \overline{\rho} \rangle_\ell} \right)' \left(\frac{\partial \langle \overline{p} \rangle_\ell'}{\partial x} - \frac{\partial \langle \overline{\tau_{11}} \rangle_\ell'}{\partial x} - \frac{\partial \langle \overline{\tau_{12}} \rangle_\ell'}{\partial y} - \frac{\partial \langle \overline{\tau_{13}} \rangle_\ell'}{\partial z} + \frac{\partial \overline{\tau_{11}^{SFS'}}}{\partial x} + \frac{\partial \overline{\tau_{12}^{SFS'}}}{\partial y} + \frac{\partial \overline{\tau_{13}^{SFS'}}}{\partial z} \right)}_{\text{term (VI)}} + \langle \overline{\rho} \rangle_\ell \varepsilon_{a_{L,1}},
\end{aligned} \tag{55}$$

where the LHS consists of rate of change (I) and convection (II). The RHS contains production (III), redistribution (IV), turbulent transport (V), and destruction (VI). Also,

$$\varepsilon_{a_{L,i}} = -\langle u_i \rangle_L' \frac{\partial \langle u_k \rangle_L'}{\partial x_k}. \tag{56}$$

b_L is the large-scale density-specific-volume covariance computed from the filtered fields and is give by $b_L = -\langle \overline{\rho} \rangle_\ell' (1/\langle \overline{\rho} \rangle_\ell)'$.

In 1D mean flow, the transport equation of $\langle \overline{\rho} \rangle_\ell b_L$ is given by:

$$\begin{aligned}
\underbrace{\frac{\partial (\langle \overline{\rho} \rangle_\ell b_L)}{\partial t}}_{\text{term (I)}} + \underbrace{\frac{\partial (\langle \overline{\rho} \rangle_\ell \widetilde{u}'_L b_L)}{\partial x}}_{\text{term (II)}} &= \underbrace{-2(b_L + 1) a_{L,1} \frac{\partial \langle \overline{\rho} \rangle_\ell}{\partial x}}_{\text{term (III)}} + \underbrace{2 \langle \overline{\rho} \rangle_\ell a_{L,1} \frac{\partial b_L}{\partial x}}_{\text{term (IV)}} \\
&+ \underbrace{\langle \overline{\rho} \rangle_\ell^2 \frac{\partial (\langle \overline{\rho} \rangle_\ell' (1/\langle \overline{\rho} \rangle_\ell)' \langle u \rangle_L' / \langle \overline{\rho} \rangle_\ell)}{\partial x}}_{\text{term (V)}} + \underbrace{2 \langle \overline{\rho} \rangle_\ell^2 \varepsilon_{b_L}}_{\text{term (VI)}},
\end{aligned} \tag{57}$$

where the LHS consists of rate of change (I) and convection (II). The RHS consists of production (III), redistribution (IV), turbulent transport (V), and destruction (VI). Also,

$$\varepsilon_{b_L} = \left(\frac{1}{\langle \rho \rangle_\ell} \right)' \frac{\partial \langle u_k \rangle'_L}{\partial x_k}. \quad (58)$$

The truncated Gaussian filter [46] is used. At each filtering operation, 1D filters in x -, y -, and z -direction are applied successively to the 3D fields. The filter in x -direction is given by:

$$\begin{aligned} \langle f_{i,j,k} \rangle_{\ell,x} = & \frac{3565}{10368} f_{i,j,k} + \frac{3091}{12960} (f_{i-1,j,k} + f_{i+1,j,k}) + \frac{1997}{25920} (f_{i-2,j,k} + f_{i+2,j,k}) \\ & + \frac{149}{12960} (f_{i-3,j,k} + f_{i+3,j,k}) + \frac{107}{103680} (f_{i-4,j,k} + f_{i+4,j,k}), \end{aligned} \quad (59)$$

where the effective filter width of one filtering operation is $\ell = 4\Delta$ and Δ is the grid spacing of the finest grid level. Filtering in y - and z -directions are in similar forms. The Gaussian filtering operation can be applied successively to achieve filtering with essentially larger filter width. If the filter is applied N_f times repeatedly, the effective filter width is $\ell \approx 4\sqrt{N_f}\Delta$. The approximated filter widths obtained on finest grid level of grid E with different number of filtering operations is shown in table III. The truncated Gaussian filter is selected because of its positivity-preserving property for the density field.

TABLE III. Approximated filter widths obtained on finest grid level of grid E with different number of filtering operations.

Number of filtering operations	Approximated filter width in Δ	Approximated filter width in physical unit (mm)
1	4 Δ	0.049
4	8 Δ	0.098
16	16 Δ	0.195
64	32 Δ	0.391
256	64 Δ	0.781

X. EFFECTS OF FILTER WIDTH ON LARGE-SCALE SECOND-MOMENTS AND SFS STRESS

The effects of filter width on the large-scale second-moments including the Reynolds normal stress in streamwise direction multiplied by the mean filtered density: $\overline{\langle \rho \rangle}_\ell a_{L,1}$, $\overline{\langle \rho \rangle}_\ell b_L$, and $\overline{\langle \rho \rangle}_\ell \tilde{R}_{L,11}$ at $t = 1.40$ ms are shown in figures 21(a), 21(b), and 21(c) respectively. It can be seen that the magnitudes of the large-scale quantities reduce when the essential width of filter applied to the density and momentum fields is increased because they are composed of scales from zero wavenumber to a larger cut-off wavenumber. The shape of each quantity remains quite self-similar with different filter widths. Especially the location of the peak of each quantity does not move significantly under the effect of filtering. At large filter widths, all large-scale second-moments including $\overline{\langle \rho \rangle}_\ell \tilde{R}_{L,11}$ have similar degrees of changes in the magnitudes with the same filter width change.

Figure 22(a) shows the effect of filtering on mean SFS normal stress component in streamwise direction, $\overline{\tau_{11}^{SFS}}$. It can be seen that the magnitude of the SFS stress component increases with larger filter width. In fact, it is noticed that the sum of $\overline{\tau_{11}^{SFS}}$ and large-scale $\overline{\langle \rho \rangle}_\ell \tilde{R}_{L,11}$ is virtually constant under the filtering effect. The same relation is also observed for the sum of large-scale turbulent kinetic energy and the mean SFS turbulent kinetic energy, $\overline{\tau_{ii}^{SFS}}/2$. The magnitude of large-scale turbulent kinetic energy decreases while that of SFS turbulent kinetic energy rises when more filtering operations are applied, as seen in figures 21(d) and 22(b) respectively. These suggest that the correlations between the small scales and large scales are negligible compared to the large-scale-large-scale and small-scale-small-scale correlations. The effects of filter width on large-scale second-moments, SFS stress, and SFS turbulent kinetic energy at other times after re-shock are shown in the Supplemental Material.

XI. BUDGETS OF LARGE-SCALE SECOND-MOMENTS AFTER RE-SHOCK

In this section, the budgets of large-scale second-moments computed with the filtered density and Favre-filtered velocity fields: $\overline{\langle \rho \rangle}_\ell a_{L,1}$, $\overline{\langle \rho \rangle}_\ell b_L$, and $\overline{\langle \rho \rangle}_\ell \tilde{R}_{L,11}$ together with $\overline{\langle \rho \rangle}_\ell k_L$ across the mixing layer after re-shock are examined. The chosen filter width is $\ell \approx 64\Delta = 0.781$ mm.

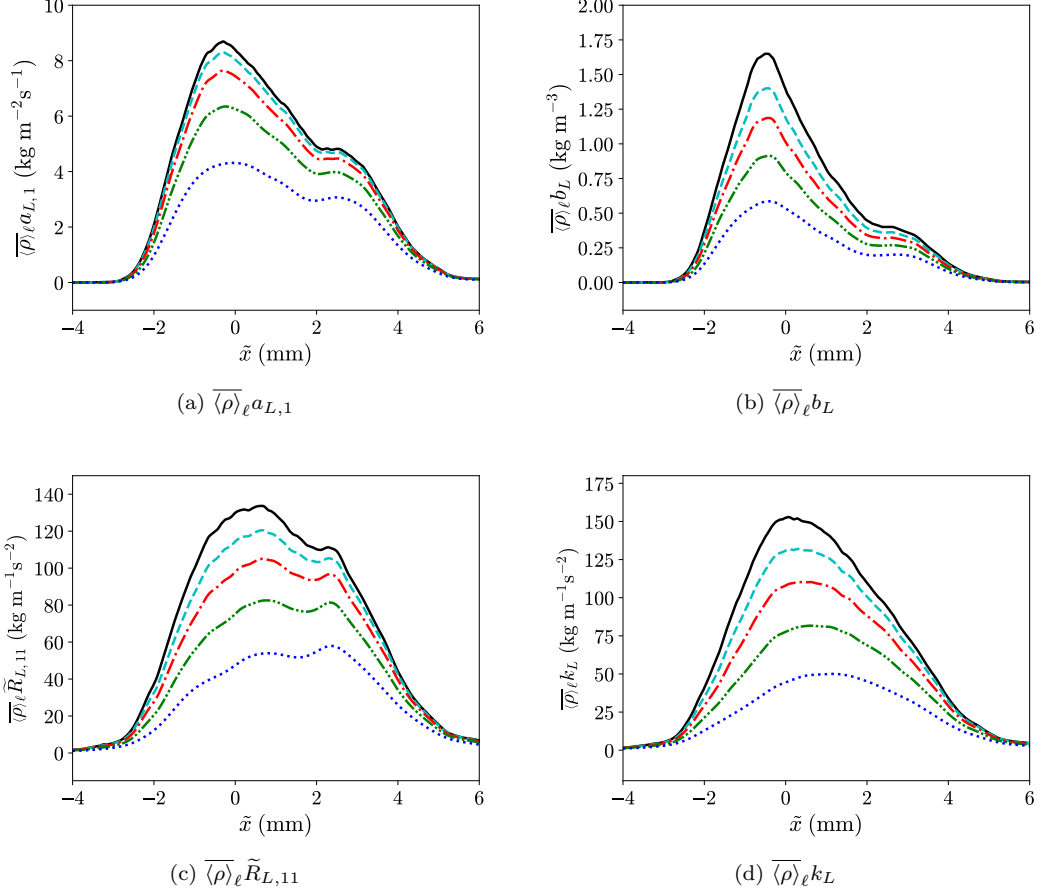


FIG. 21. Effect of filtering on large-scale second-moments and turbulent kinetic energy, $\overline{(\rho)_\ell} k_L$, at $t = 1.40$ ms after re-shock. Black solid line: no filtering; cyan dashed line: $\ell \approx 8\Delta$; red dash-dotted line: $\ell \approx 16\Delta$; green dash-dot-dotted line: $\ell \approx 32\Delta$; blue dotted line: $\ell \approx 64\Delta$.

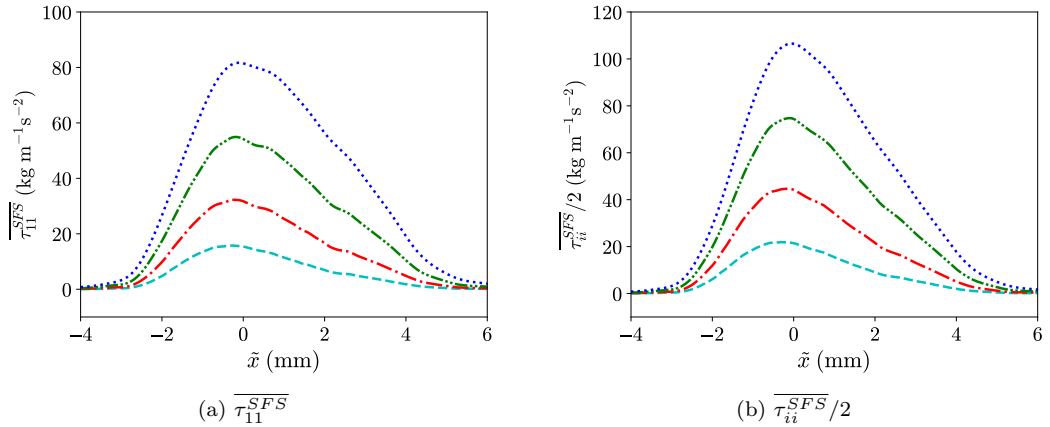


FIG. 22. Effect of filtering on mean SFS stress component in streamwise direction, $\overline{\tau_{11}^{SFS}}$, and mean SFS turbulent kinetic energy, $\overline{\tau_{ii}^{SFS}}/2$ at $t = 1.40$ ms after re-shock. Cyan dashed line: $\ell \approx 8\Delta$; red dash-dotted line: $\ell \approx 16\Delta$; green dash-dot-dotted line: $\ell \approx 32\Delta$; blue dotted line: $\ell \approx 64\Delta$.

As with the unfiltered budgets before re-shock, the budgets of large-scale second-moments after re-shock are studied

in the \tilde{x} coordinate system, equivalent to studying the budgets in the moving reference frame of the mixing layer. The convective terms in all of the transport equations of large-scale second-moments for 1D mean flow have the common form of $[\overline{\langle \rho \rangle_\ell \langle u \rangle_L}(\cdot)]_{,1}$, where (\cdot) represents any of the large-scale second-moments ($a_{L,1}$, b_L , $\tilde{R}_{L,ij}$, or k_L). Using the relation $\langle u \rangle_L = \overline{\langle u \rangle_L} + a_{L,1}$, the convective terms can be rewritten as:

$$\frac{\partial \overline{\langle \rho \rangle_\ell \langle u \rangle_L}(\cdot)}{\partial x} = \underbrace{\frac{\partial \overline{\langle \rho \rangle_\ell \overline{\langle u \rangle_L}(\cdot)}{\partial x}}_{\text{term (I)}} + \underbrace{\frac{\partial \overline{\langle \rho \rangle_\ell} a_{L,1}(\cdot)}{\partial x}}_{\text{term (II)}}, \quad (60)$$

where term (I) is the convection due to mean Favre-filtered velocity and term (II) is the convection due to velocity associated with large-scale turbulent mass flux. Similar to the case without filtering, $\overline{\langle u \rangle_L}$ is observed to be uniformly close to zero in the moving reference frame of the mixing layer and the term (I) can be neglected. Thus, the convective term can be thought as fully contributed by $[\overline{\langle \rho \rangle_\ell} a_{L,1}]_{,1}$. In this section, only the budgets of the large-scale second-moments at $t = 1.20$ ms and $t = 1.60$ ms are shown. The budgets at other times after re-shock are included in the Supplemental Material.

A. Large-scale turbulent mass flux

Figure 23 shows the spatial profiles of different RHS terms in the transport equation of large-scale turbulent mass flux component in streamwise direction, $\overline{\langle \rho \rangle_\ell} a_{L,1}$, given by equation (55), together with the negative of the convection term due to $a_{L,1}$ after re-shock. Similar to the budgets before re-shock, the magenta dotted line represents the residue which is defined as the subtraction of the net RHS terms from the net LHS term in the simulation frame. The residue here provides a way to verify that the numerical regularization or SGS effect has negligible effects on the budgets of large-scale second-moments at the chosen filter width. The rate of change of $\overline{\langle \rho \rangle_\ell} a_{L,1}$ in the moving reference frame of the mixing layer is represented by the thin black line, which is the subtraction of convective term due to $a_{L,1}$ from the summation of net RHS and residue.

As seen from figure 23, the production and destruction terms are the dominant terms among all RHS terms in the interior mixing region after re-shock. In this region, the magnitude of destruction is larger than that of the production, and this drives the peak of large-scale turbulent mass flux to diminish over time after re-shock, as indicated by the negative rate of change at all times. At the edges of the mixing region, the turbulent transport term becomes relatively more important and causes the turbulent mass flux to spread over time. The redistribution and convective terms are small across the mixing layer compared to other RHS terms. In fact, the redistribution term is commonly ignored in many turbulent mixing models, such as the BHR k - S - a model by Banerjee *et al.* [18] and the k - L - a model by Morgan and Wickett [23]. The compositions of the production and destruction terms are shown in figures 24 and 25 respectively. As seen from both figures, the components with filtered molecular shear stress, $-b_L \overline{\langle \tau_{11} \rangle_{\ell,1}}$ and $-\overline{\langle \rho \rangle_\ell} (1/\langle \rho \rangle_\ell)' (\partial \langle \tau_{1i} \rangle'_\ell / \partial x_i)$, are both zero at different times and this indicates that the molecular shear stress has no direct effect on the large-scale turbulent mass flux through its budget.

Examining figure 24 for the composition of the production term, it can be seen that that the shapes and relative importance of the two components of the production term, $-\tilde{R}_{L,11} \overline{\langle \rho \rangle_{\ell,1}}$ and $b_L \overline{\langle p \rangle_{\ell,1}}$, after re-shock are similar to those of the corresponding ones before re-shock. However, there is an additional term with the SFS stress, $b_L \overline{\tau_{11}^{SFS}}_{,1}$, in the composition due to filtering. In general, the component with the large-scale Reynolds stress, $-\tilde{R}_{L,11} \overline{\langle \rho \rangle_{\ell,1}}$, has the largest contribution to production term and appears strictly positive. Another two constituents, $b_L \overline{\langle p \rangle_{\ell,1}}$ and $b_L \overline{\tau_{11}^{SFS}}_{,1}$, have smaller contributions and have conflicting effects. The latter largely reduces the influence of the former on the production term. Therefore, the production term can be regarded as mainly supplied by the component with the large-scale Reynolds stress. As for the destruction, it can be seen in figure 25 that the contribution of each constituent after re-shock is similar to the corresponding one in the unfiltered budgets before re-shock, except that the role of the component with molecular shear stress is replaced by a component with SFS stress, $\overline{\langle \rho \rangle_\ell} (1/\langle \rho \rangle_\ell)' (\partial \tau_{1i}^{SFS} / \partial x_i)$. Similar to the corresponding component with ε_{a_1} in the budgets before re-shock, the component with $\varepsilon_{a_{L,1}}$ also contributes significantly to the destruction term after re-shock.

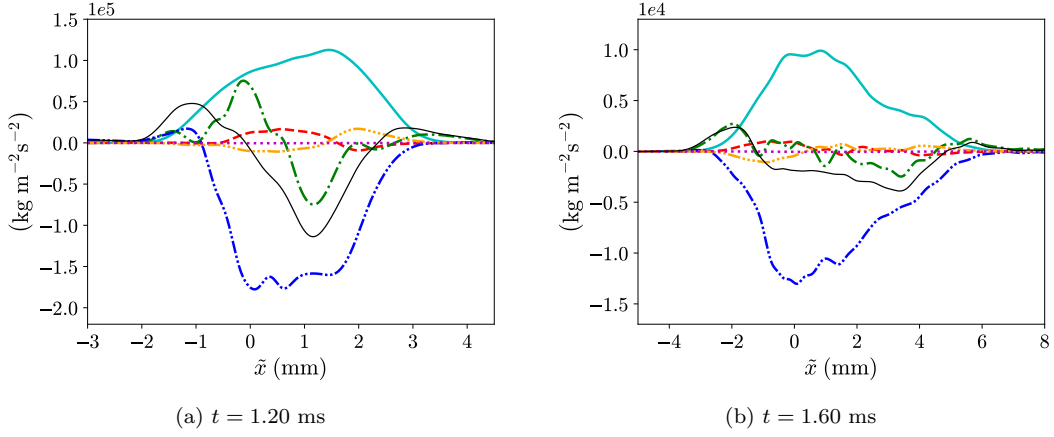


FIG. 23. Budgets of large-scale turbulent mass flux component in streamwise direction, $\overline{\langle \rho \rangle}_\ell a_{L,1}$, given by equation (55), at different times after re-shock. Cyan solid line: production (III); red dashed line: redistribution (IV); green dash-dotted line: turbulent transport (V); blue dash-dot-dotted line: destruction (VI); orange dash-triple-dotted line: negative of convection due to streamwise velocity associated with turbulent mass flux; magenta dotted line: residue; thin black solid line: summation of all terms (rate of change in the moving frame).

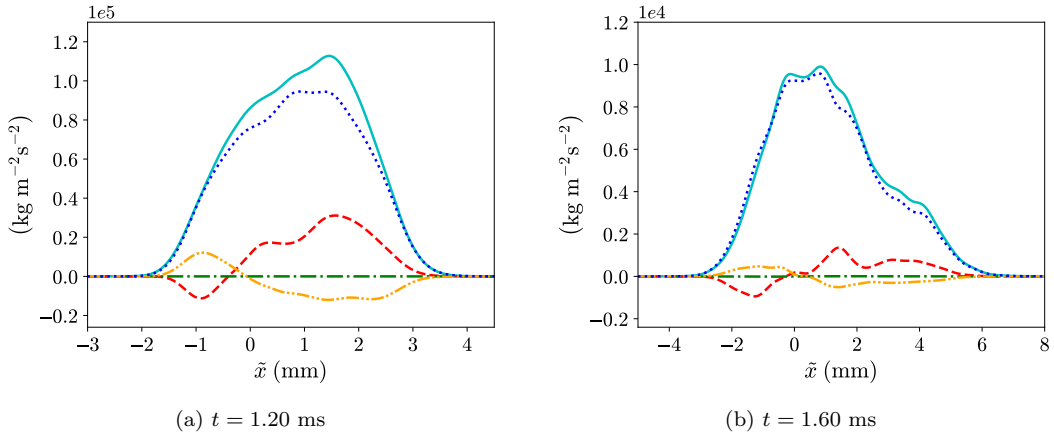


FIG. 24. Compositions of production term in the transport equation of large-scale turbulent mass flux component in streamwise direction, $\overline{\langle \rho \rangle}_\ell a_{L,1}$, at different times after re-shock. Cyan solid line: overall production; red dashed line: $b_L \overline{\langle p \rangle}_{\ell,1}$; green dash-dotted line: $-b_L \overline{\langle \tau_{11} \rangle}_{\ell,1}$; orange dash-dot-dotted line: $b_L \overline{\tau_{11}^{SFS}}_{,1}$; blue dotted line: $-\tilde{R}_{L,11} \overline{\langle \rho \rangle}_{\ell,1}$.

B. Large-scale density-specific-volume covariance

Figure 26 shows the spatial profiles of different terms that appear in the transport equation of large-scale density-specific-volume covariance multiplied by the mean filtered density, $\overline{\langle \rho \rangle}_\ell b_L$, given by equation (57) after re-shock. As same as the plots for budgets of the large-scale turbulent mass flux, the magenta dotted line represents the residue. As seen in the sub-figures, the residue is virtually zero at different times after re-shock and this means that there is insignificant effect of numerical regularization on the rate of change of $\overline{\langle \rho \rangle}_\ell b_L$.

As seen from the figure, the production and destruction terms are the dominant terms in the interior region of the mixing layer. In the interior part of the mixing layer, the rate of change of $\overline{\langle \rho \rangle}_\ell b_L$ is negative just after re-shock as the magnitude of the negative destruction term is larger than that of the positive production term. Thus, the amplitude of the large-scale second-moment decreases just after re-shock. Nevertheless, soon after re-shock, the relative magnitude of the production term in the middle part of the mixing layer becomes larger, and even larger than that of the destruction term at late times. As a result, the rate of change of $\overline{\langle \rho \rangle}_\ell b_L$ at the peak location turns positive at later times. Although the turbulent transport term is not small in the central part of the mixing layer, its effect is small compared to the production and destruction terms. However, the turbulent transport term becomes relatively more

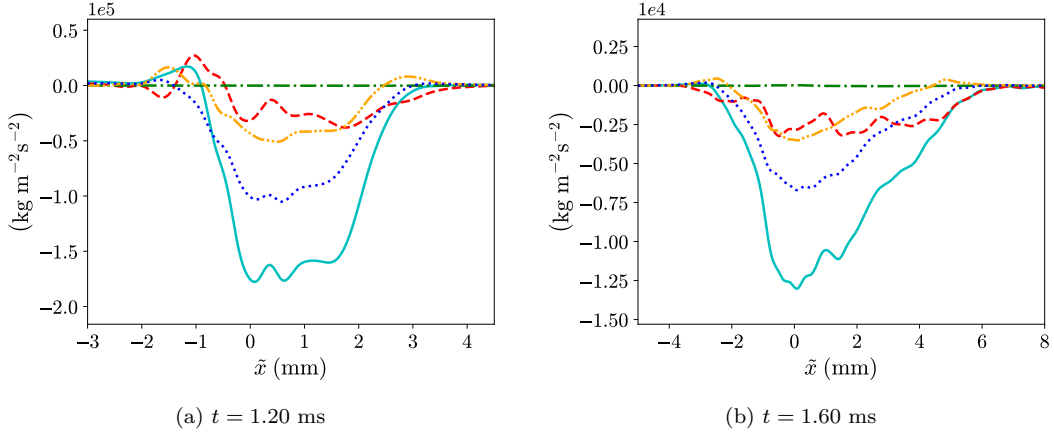


FIG. 25. Compositions of destruction term in the transport equation of large-scale turbulent mass flux component in streamwise direction, $\overline{\langle \rho \rangle_\ell} \alpha_{L,1}$, at different times after re-shock. Cyan solid line: overall destruction; red dashed line: $\langle \rho \rangle_\ell (1/\langle \rho \rangle_\ell)' \langle p \rangle'_{\ell,1}$; green dash-dotted line: $-\langle \rho \rangle_\ell (1/\langle \rho \rangle_\ell)' (\partial \langle \tau_{1i} \rangle'_\ell / \partial x_i)$; orange dash-dot-dotted line: $\langle \rho \rangle_\ell (1/\langle \rho \rangle_\ell)' (\partial \tau_{1i}^{SS'} / \partial x_i)$; blue dotted line: $\langle \rho \rangle_\ell \varepsilon_{\alpha L,1}$.

important at the edges of mixing region. The term is positive at both edges and is the vital term at the heavier fluid side especially. This leads to the spreading of $\langle \rho \rangle_\ell b_L$ over time.

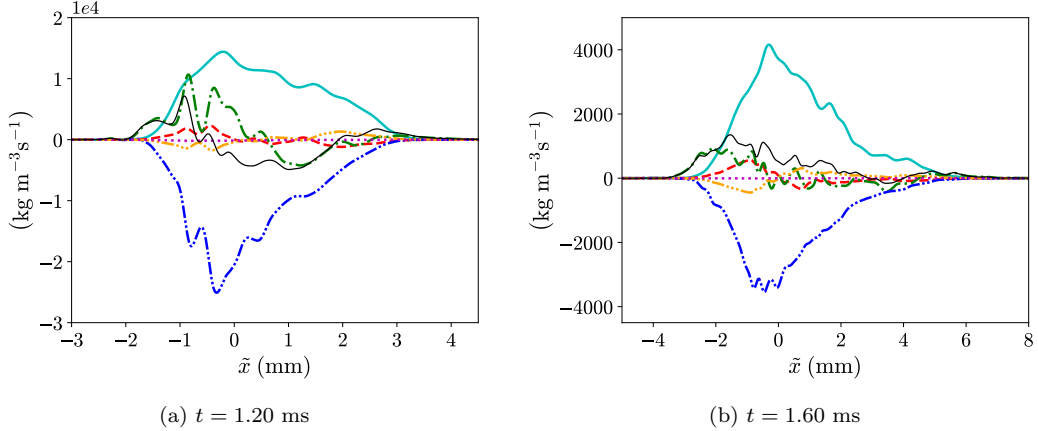


FIG. 26. Budgets of large-scale density-specific-volume covariance multiplied by mean filtered density, $\overline{\langle \rho \rangle_\ell} b_L$, given by equation (57), at different times after re-shock. Cyan solid line: production (III); red dashed line: redistribution (IV); green dash-dotted line: turbulent transport (V); blue dash-dot-dotted line: destruction (VI); orange dash-triple-dotted line: negative of convection due to streamwise velocity associated with turbulent mass flux; magenta dotted line: residue; thin black solid line: summation of all terms (rate of change in the moving frame).

C. Large-scale Favre-averaged Reynolds stress and large-scale turbulent kinetic energy

In figure 27, the spatial profiles of different budget terms of large-scale Favre-averaged Reynolds stress component in the streamwise direction multiplied by the mean filtered density, $\overline{\langle \rho \rangle_\ell} \tilde{R}_{L,11}$, after re-shock are shown. Each budget term in the transport equation of $\overline{\langle \rho \rangle_\ell} \tilde{R}_{L,11}$ is given by equation (52). As shown in the figure, the residue, represented by the magenta dotted line, is basically zero at all times. Thus, the effect of numerical regularization on $\overline{\langle \rho \rangle_\ell} \tilde{R}_{L,11}$ can be ignored.

From the figure, we can see that all terms except the convection term play significant roles on the rate of change

of $\overline{\langle \rho \rangle}_\ell \widetilde{R}_{L,11}$ in the interior part of the mixing region. Similar to the budgets before re-shock, the production term is positive on the light fluid side and negative on the heavy fluid side to transport $\overline{\langle \rho \rangle}_\ell \widetilde{R}_{L,11}$ from the heavier fluid side to the lighter fluid side. On the other hand, generally the turbulent transport term has larger magnitude but opposite effect in the interior region of the mixing layer compared to the production term. In the same region, both pressure-strain redistribution and dissipation terms are negative in general and hence the overall rate of change is negative. At the edges the mixing layer, only the turbulent transport and pressure-strain redistribution are critical terms. Their combined effect contributes to the spreading of $\overline{\langle \rho \rangle}_\ell \widetilde{R}_{L,11}$ on the lighter fluid side over time while there is some anti-spreading effect on the heavier fluid side for a quite long period of time after re-shock.

Figures 28 and 29 show the compositions of production and turbulent transport terms respectively after re-shock. Both figures show that the components due to filtered molecular shear stress, $-2a_{L,1}\overline{\langle \tau_{11} \rangle}_\ell$ and $2\overline{\langle u \rangle}'_L \overline{\langle \tau_{11} \rangle}'_\ell$, are insignificant to the budgets at different times after re-shock. Considering the composition of production term in figure 28, the component with SFS stress, $2a_{L,1}\overline{\tau_{11}^{SFS}}$, appears as a new term compared to the budgets without filtering before re-shock. Both constituents $2a_{L,1}\overline{\langle p \rangle}'_\ell$ and $-2\overline{\langle \rho \rangle}_\ell \widetilde{R}_{L,11} \overline{\langle u \rangle}'_{L,1}$ play similar roles to the production term. They are negative on the heavier fluid side and positive on the lighter fluid side. However, the former has larger effect on the lighter side while the effect of the latter is stronger on the heavier fluid side. The component with SFS stress has similar magnitude as $-2\overline{\langle \rho \rangle}_\ell \widetilde{R}_{L,11} \overline{\langle u \rangle}'_{L,1}$ but opposite effect that brings $\overline{\langle \rho \rangle}_\ell \widetilde{R}_{L,11}$ from the lighter fluid side to the heavier fluid side. Inspecting the composition of the turbulent transport term, the three constituents: $-\overline{\langle \rho \rangle}_\ell \overline{\langle u \rangle}'_L \overline{\langle u \rangle}''_L \overline{\langle u \rangle}''_L$, $-2\overline{\langle u \rangle}'_L \overline{\langle p \rangle}'_\ell$, and $-2\overline{\langle u \rangle}'_L \tau_{11}^{SFS'}$ have significant contributions to the term after re-shock. The triple velocity correlation component, $-\overline{\langle \rho \rangle}_\ell \overline{\langle u \rangle}''_L \overline{\langle u \rangle}''_L \overline{\langle u \rangle}''_L$, and the component arisen from filtering, $-2\overline{\langle u \rangle}'_L \tau_{11}^{SFS'}$, are responsible for the spreading of the $\overline{\langle \rho \rangle}_\ell \widetilde{R}_{L,11}$. On the other hand, the constituent $-2\overline{\langle u \rangle}'_L \overline{\langle p \rangle}'_\ell$ has anti-spreading effect.

Figure 30 shows the comparison of different budget terms in the transport equation of large-scale turbulent kinetic energy, $\overline{\langle \rho \rangle}_\ell k_L$, given by equation (54). It should be noted that in incompressible single-species flow, the pressure-dilatation term is zero. As seen from the figure, the pressure-dilatation term in the variable-density flow being studied here is not zero. However, its influence is generally very small across the mixing layer and its effect is roughly canceled by the convection term. The effect from pressure-dilatation is commonly ignored in many RANS-based models [18, 23] for RMI-induced turbulence. In the interior part of the mixing region, the dissipation dominates the overall rate of change of the large-scale turbulent kinetic energy and the quantity decays over time. Note that the dissipation term is contributed mainly by the component with SFS stress, $\tau_{ij}^{SFS'}(\partial \langle u_i \rangle'_L / \partial x_j)$.

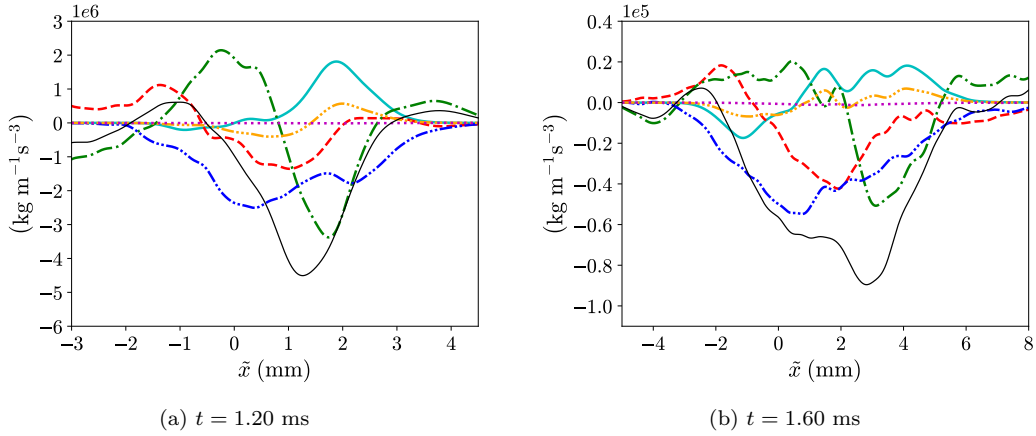


FIG. 27. Budgets of large-scale Favre-averaged Reynolds normal stress component in streamwise direction multiplied by mean filtered density, $\overline{\langle \rho \rangle}_\ell \widetilde{R}_{L,11}$, given by equation (52), at different times after re-shock. Cyan solid line: production (III); red dashed line: press-strain redistribution (V); green dash-dotted line: turbulent transport (IV); blue dash-dot-dotted line: dissipation (VI); orange dash-triple-dotted line: negative of convection due to streamwise velocity associated with turbulent mass flux; magenta dotted line: residue; thin black solid line: summation of all terms (rate of change in the moving frame).

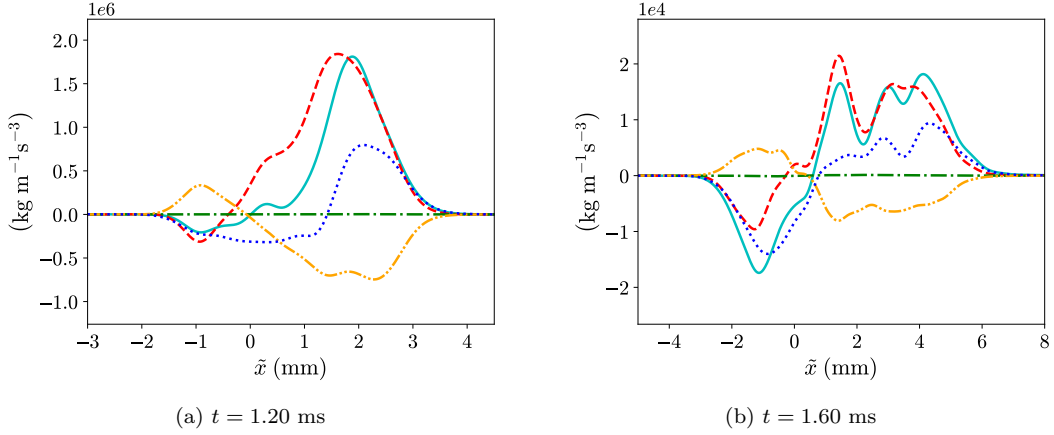


FIG. 28. Compositions of production term in the transport equation of large-scale Favre-averaged Reynolds normal stress component in streamwise direction multiplied by mean filtered density, $\langle \rho \rangle_{\ell} \tilde{R}_{L,11}$, at different times after re-shock. Cyan solid line: overall production; red dashed line: $2a_{L,1}\langle p \rangle_{\ell,1}$; green dash-dotted line: $-2a_{L,1}\langle \tau_{11} \rangle_{\ell,1}$; orange dash-dot-dotted line: $2a_{L,1}\tau_{11}^{SFS'}{}_{,1}$; blue dotted line: $-2\langle \rho \rangle_{\ell} \tilde{R}_{L,11} \langle u \rangle_{L,1}$.

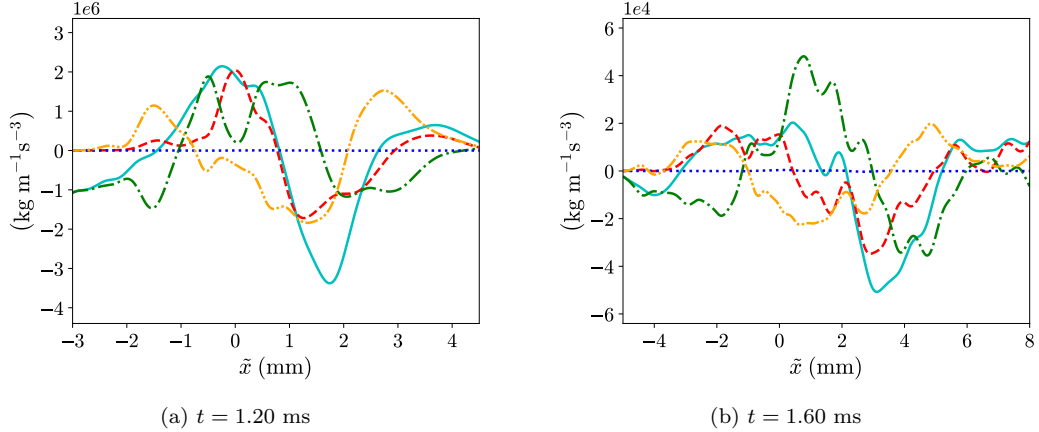


FIG. 29. Compositions of turbulent transport term in the transport equation of large-scale Favre-averaged Reynolds normal stress component in streamwise direction multiplied by mean filtered density, $\langle \rho \rangle_{\ell} \tilde{R}_{L,11}$, at different times after re-shock. Cyan solid line: overall turbulent transport; red dashed line: $-\langle \rho \rangle_{\ell} \langle u \rangle_L' \langle u \rangle_L'' \langle u \rangle_L''$; green dash-dotted line: $-2\langle u \rangle_L' \langle p \rangle_{\ell,1}$; blue dotted line: $2\langle u \rangle_L' \langle \tau_{11} \rangle_{\ell,1}$; orange dash-dot-dotted line: $-2\langle u \rangle_L' \tau_{11}^{SFS'}{}_{,1}$.

XII. EFFECTS OF FILTERING ON BUDGETS OF LARGE-SCALE SECOND-MOMENTS AFTER RE-SHOCK

The effects of filtering on the budgets of different large-scale second-moments and turbulent kinetic energy with $\ell \approx 16\Delta$ and $\ell \approx 64\Delta$ at $t = 1.40$ ms after re-shock are shown in figures 31, 32, 33, and 34 respectively. Note that the unfiltered budgets and filtered budgets with another filter width can be found in the Supplemental Material.

It should be mentioned that the budget of $\bar{\rho}a_1$ is already closed when no filtering is used and hence from figure 31, it can be seen that the residues in the budgets of the corresponding large-scale turbulent mass flux component with different filter widths are also negligible across the entire mixing region. Similar to the effects of the filter on the large-scale second-moments, the magnitudes of different terms in the transport equation of the large-scale turbulent mass flux component decrease when larger filter width is applied on the mixture density and momentum equations, but their shapes remain quite self-similar. From figures 32 and 33, it can be seen that the residues in the budgets of density-specific-volume covariance and the Reynolds normal stress component (both multiplied by the mean filtered density) are already virtually zero when the Navier–Stokes equations are filtered with filter width $\ell \approx 16\Delta$. The shapes

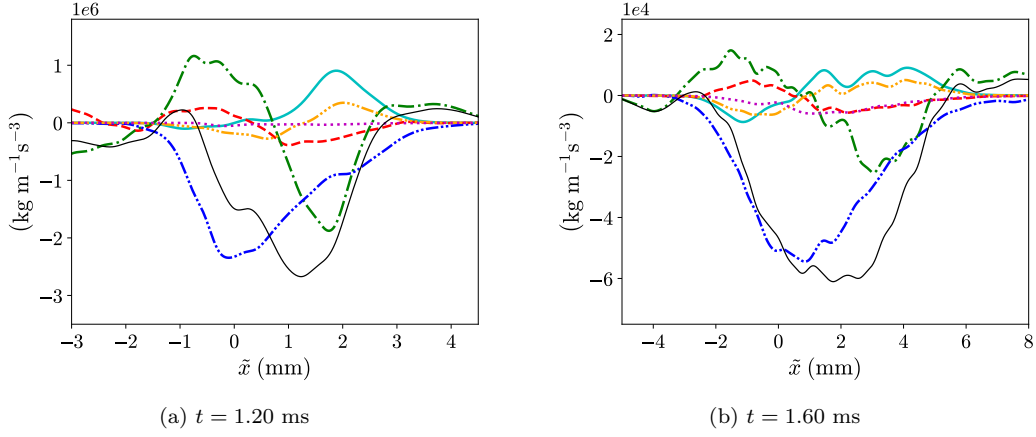


FIG. 30. Budgets of large-scale turbulent kinetic energy, $\overline{\langle \rho \rangle_\ell k_L}$, given by equation (54), at different times after re-shock. Cyan solid line: production (III); red dashed line: pressure-dilatation (V); green dash-dotted line: turbulent transport (IV); blue dash-dot-dotted line: dissipation (VI); orange dash-triple-dotted line: negative of convection due to streamwise velocity associated with turbulent mass flux; magenta dotted line: residue; thin black solid line: summation of all terms (rate of change in the moving frame).

of different terms in the budgets of the two large-scale second-moments also appear self-similar and the magnitudes reduce with larger filter width. As for the budgets of large-scale turbulent kinetic energy, even larger filter width, or more successive filtering operations are needed for the residue to become negligibly small, which is indicated by figure 34. Nevertheless, the budget terms of the large-scale turbulent kinetic energy are also quite similar for filter widths $\ell \approx 16\Delta$ and $\ell \approx 64\Delta$.

Figures 35 and 36 respectively show the effects of filtering on the compositions of production and destruction terms in the budgets of large-scale turbulent mass flux component in streamwise direction at $t = 1.40$ ms. It can be seen from both figures that the magnitudes of components with the SFS stress in the production and destruction compositions, $b_L \overline{\tau_{11}^{SFS}}_{,1}$ and $\overline{\langle \rho \rangle_\ell (1/\langle \rho \rangle_\ell)' (\partial \tau_{1i}^{SFS'} / \partial x_i)}$, increase when larger filter width is applied. Examining the production term, while there is a larger effect from the constituent with the SFS stress, $b_L \overline{\tau_{11}^{SFS}}_{,1}$ with wider filter width, the magnitude of term $b_L \overline{\langle p \rangle}_{\ell,1}$ also becomes larger to offset the increased effect from $b_L \overline{\tau_{11}^{SFS}}_{,1}$. Thus, the shape of the overall production term remains self-similar with filtering. As for the destruction term, the corresponding component with SFS stress also increases in magnitude to provide more destruction effect when the filter width is larger but another two constituents, $\overline{\langle \rho \rangle_\ell (1/\langle \rho \rangle_\ell)' \langle p \rangle'_{\ell,1}}$ and $\overline{\langle \rho \rangle_\ell \varepsilon_{a_L,1}}$ adjust (the magnitude of the former decreases and that of the latter increases) and hence the overall destruction term is also self-similar with filtering.

The effects of filtering on the composition of production and turbulent transport terms in the budget of large-scale Reynolds normal stress component in streamwise direction multiplied by mean filtered density are studied in figures 37 and 38 respectively at $t = 1.40$ ms. The component with SFS stress in the production term, $2a_{L,1} \overline{\tau_{11}^{SFS}}_{,1}$, has larger magnitude with more filtering operations but this change is offset by the adjustment of $2a_{L,1} \overline{\langle p \rangle}_{\ell,1}$ which also has larger magnitude but opposite effect compared with the former. Similarly, the constituent with SFS stress in the turbulent transport term, $-2(\overline{\langle u \rangle'_L \tau_{11}^{SFS'}})_{,1}$, has greater magnitude as the filter width increases but its larger influence is offset by the change of $-2(\overline{\langle u \rangle'_L \langle p \rangle'_{\ell,1}})$. In general, the overall shapes of production and turbulent transport term are quite similar for different filter widths, but their compositions change as the SFS stress plays more important role in each of the two terms.

XIII. CONCLUSIONS

Second-moment analysis of high Atwood number variable-density mixing induced by RMI was conducted with high-resolution 3D AMR simulation data. In the numerical experiment, the material interface separating SF₆ and air is impulsively accelerated twice and the mixing layer becomes turbulent after re-shock. The roles of the two second-moments: turbulent mass flux and density-specific-volume covariance play in the development of Favre-averaged Reynolds stress were discussed through the examination the transport equations of the second-moments, including

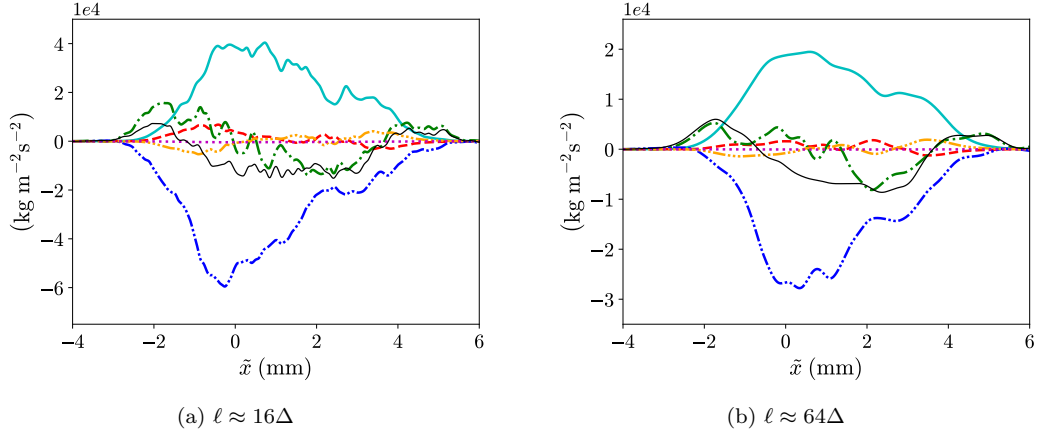


FIG. 31. Effect of filtering on budgets of large-scale turbulent mass flux component in streamwise direction, $\overline{(\rho)_\ell} a_{L,1}$, given by equation (55), at $t = 1.40$ ms. Cyan solid line: production (III); red dashed line: redistribution (IV); green dash-dotted line: turbulent transport (V); blue dash-dot-dotted line: destruction (VI); orange dash-triple-dotted line: negative of convection due to streamwise velocity associated with turbulent mass flux; magenta dotted line: residue; thin black solid line: summation of all terms (rate of change in the moving frame).

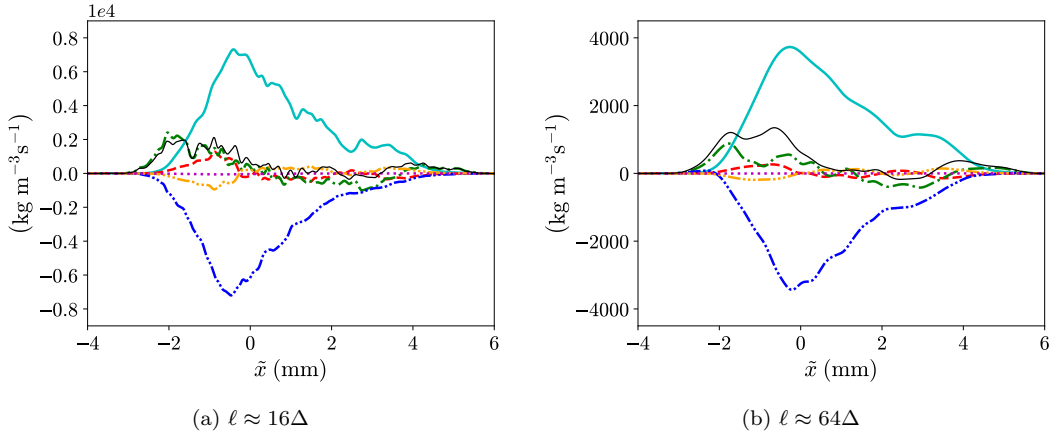


FIG. 32. Effect of filtering on budgets of large-scale density-specific-volume covariance multiplied by mean filtered density, $\overline{(\rho)_\ell} b_L$, given by equation (57), at $t = 1.40$ ms. Cyan solid line: production (III); red dashed line: redistribution (IV); green dash-dotted line: turbulent transport (V); blue dash-dot-dotted line: destruction (VI); orange dash-triple-dotted line: negative of convection due to streamwise velocity associated with turbulent mass flux; magenta dotted line: residue; thin black solid line: summation of all terms (rate of change in the moving frame).

the Favre-averaged Reynolds stress and turbulent kinetic energy. The study of the transport mechanisms of the second-moments can foster the improvement of existing reduced-order models for closing the Favre-averaged Navier–Stokes equations in RANS-based simulations. The quantities of interest including the second-moments computed with the simulation data were found to be well grid-converged at the finest grid setting and the study of their time evolution revealed the non-Boussinesq and anisotropic nature of the variable-density flow induced by RMI. The transport equations of the Reynolds stress and second-moments were studied before re-shock when mixing occurs due to the instability. The relative importance of different terms in the budgets of the quantities across the mixing layer was found to vary a lot and the origins of the generation, destruction, and spreading of the quantities of interest over time were traced back to the corresponding budget terms. Unlike the situation that all scales in the flow are well-resolved in the highest resolution simulation before re-shock, the wide span of scales generated due to mixing transition after re-shock leads to under-resolved simulation results. While the budgets of some second-moments, including the Reynolds stress, are unclosed during this time period, the budgets of large-scale Reynolds stress and second-moments at sufficiently large scale were found to be unaffected by the numerical regularization, when the influence of the SFS stress is taken into account. The effects of SFS stress on the development of large-scale quantities at different

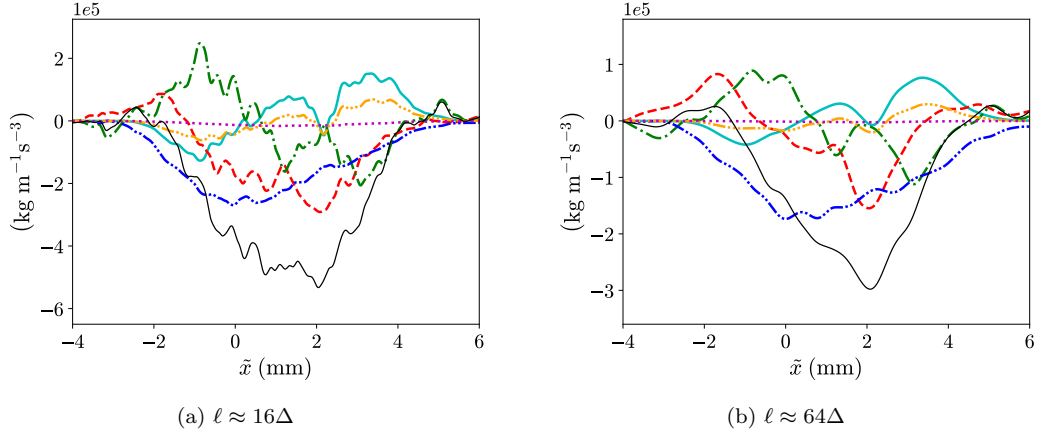


FIG. 33. Effect of filtering on budgets of large-scale Reynolds normal stress component in streamwise direction multiplied by mean filtered density, $\overline{\langle \rho \rangle}_\ell \tilde{R}_{L,11}$, given by equation (52), at $t = 1.40$ ms. Cyan solid line: production (III); red dashed line: press-strain redistribution (V); green dash-dotted line: turbulent transport (IV); blue dash-dot-dotted line: dissipation (VI); orange dash-triple-dotted line: negative of convection due to streamwise velocity associated with turbulent mass flux; magenta dotted line: residue; thin black solid line: summation of all terms (rate of change in the moving frame).

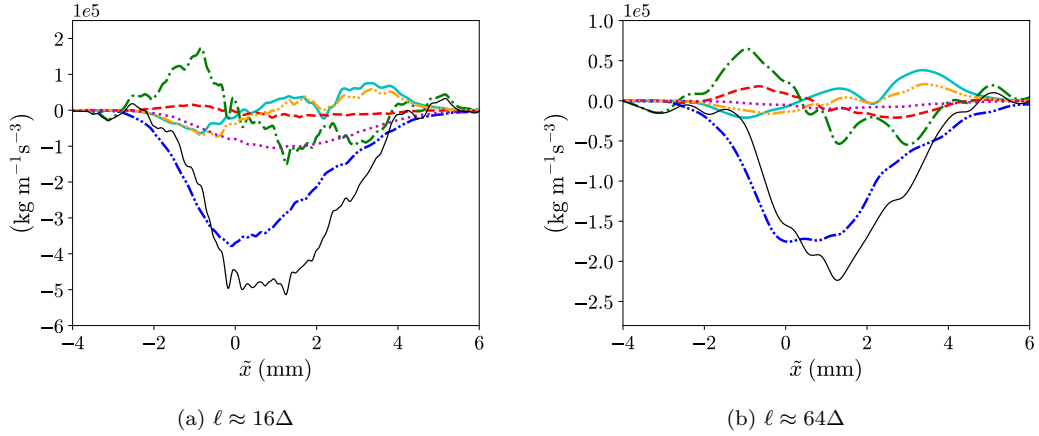


FIG. 34. Effect of filtering on budgets of large-scale turbulent kinetic energy, $\overline{\langle \rho \rangle}_\ell k_L$, given by equation (54), at $t = 1.40$ ms. Cyan solid line: production (III); red dashed line: pressure-dilatation (V); green dash-dotted line: turbulent transport (IV); blue dash-dot-dotted line: dissipation (VI); orange dash-triple-dotted line: negative of convection due to streamwise velocity associated with turbulent mass flux; magenta dotted line: residue; thin black solid line: summation of all terms (rate of change in the moving frame).

filtered scales were studied. Although the SFS stress significantly contributes to the composition of different budget terms, the overall budgets of large-scale Reynolds stress and second-moments remain quite self-similar with filtering. This suggests that analysis of budgets of large-scale quantities in LESs can be relevant for the development and validation of RANS-based models, when the effects of SFS stress are included. This also addresses the importance of reconstructing SFS stress in LESs of this type of variable-density flows in order to model the development of the turbulence accurately. Nevertheless, the study of the evolution mechanism of SFS stress requires the analysis of its transport equation with fully resolved turbulence data. As a result, future research of RMI-induced variable-density turbulence with DNS data can largely advance turbulence modeling in both LES and hybrid RANS-LES approaches.

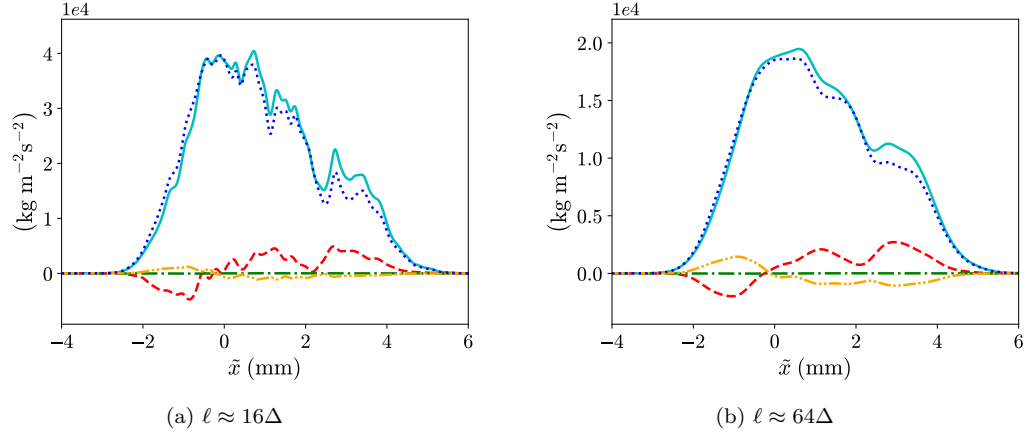


FIG. 35. Effect of filtering on compositions of production term in the transport equation of large-scale turbulent mass flux component in streamwise direction, $\langle \rho \rangle_\ell a_{L,1}$, at $t = 1.40$ ms. Cyan solid line: overall production; red dashed line: $b_L \langle p \rangle_{\ell,1}$; green dash-dotted line: $-b_L \langle \tau_{11} \rangle_{\ell,1}$; orange dash-dot-dotted line: $b_L \tau_{11}^{SFS'}_{\ell,1}$; blue dotted line: $-\tilde{R}_{L,11} \langle \rho \rangle_{\ell,1}$.

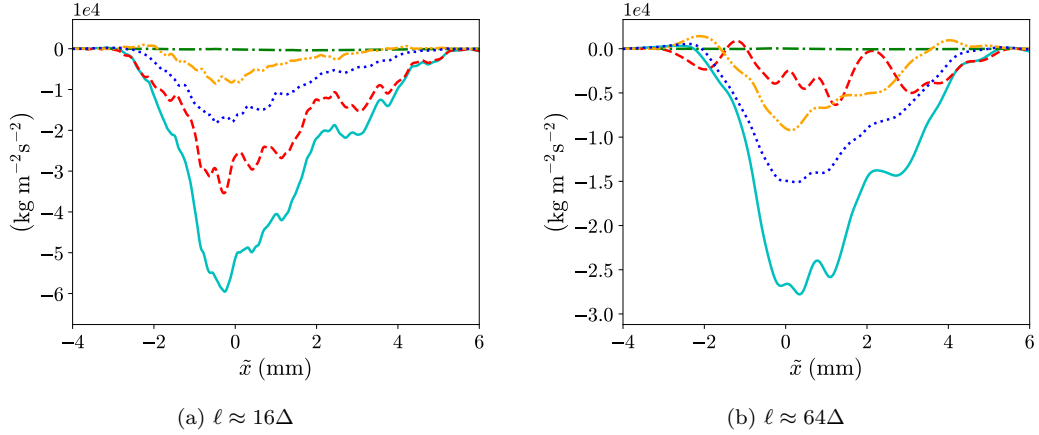


FIG. 36. Effect of filtering on compositions of destruction term in the transport equation of large-scale turbulent mass flux component in streamwise direction, $\langle \rho \rangle_\ell a_{L,1}$, at $t = 1.40$ ms. Cyan solid line: overall destruction; red dashed line: $\langle \rho \rangle_\ell (1/\langle \rho \rangle_\ell)' \langle p \rangle'_{\ell,1}$; green dash-dotted line: $-\langle \rho \rangle_\ell (1/\langle \rho \rangle_\ell)' (\partial \langle \tau_{1i} \rangle'_\ell / \partial x_i)$; orange dash-dot-dotted line: $\langle \rho \rangle_\ell (1/\langle \rho \rangle_\ell)' (\partial \tau_{1i}^{SFS'} / \partial x_i)$; blue dotted line: $\langle \rho \rangle_\ell \varepsilon_{a_{L,1}}$.

XIV. ACKNOWLEDGMENTS

This work was performed under the auspices of U.S. Department of Energy. M. L. Wong and S. K. Lele were supported by Los Alamos National Laboratory, under Grant No. 431679. Los Alamos National Laboratory is operated by Triad National Security, LLC, for the National Nuclear Security Administration of U.S. Department of Energy (Contract No. 89233218CNA000001). Computational resources were provided by the Los Alamos National Laboratory Institutional Computing Program and the Advanced Simulation and Computation (ASC) Program.

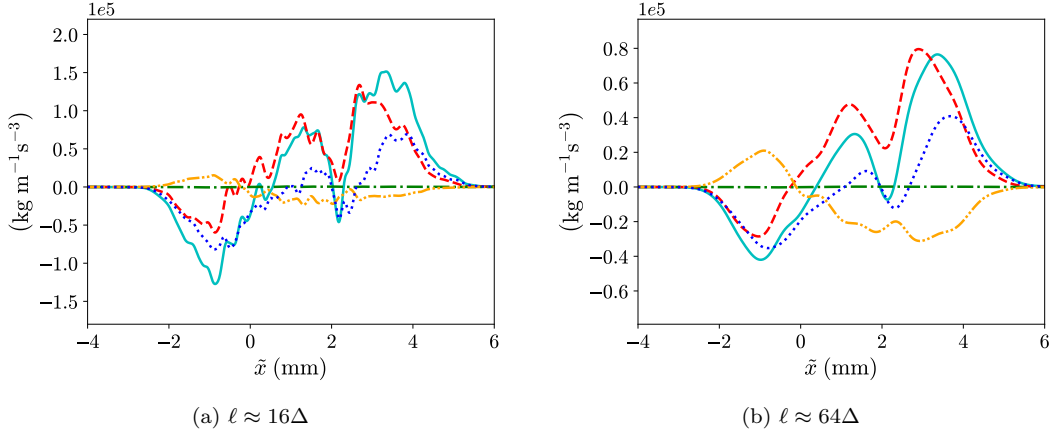


FIG. 37. Effect of filtering on compositions of production term in the transport equation of large-scale Favre-averaged Reynolds normal stress component in streamwise direction multiplied by mean filtered density, $\langle \rho \rangle_\ell \tilde{R}_{L,11}$, at $t = 1.40$ ms. Cyan solid line: overall production; red dashed line: $2a_{L,1} \langle p \rangle_{\ell,1}$; green dash-dotted line: $-2a_{L,1} \langle \tau_{11} \rangle_{\ell,1}$; orange dash-dot-dotted line: $2a_{L,1} \tau_{11}^{SFS'}$; blue dotted line: $-2 \langle \rho \rangle_\ell \tilde{R}_{L,11} \langle u \rangle_{L,1}$.

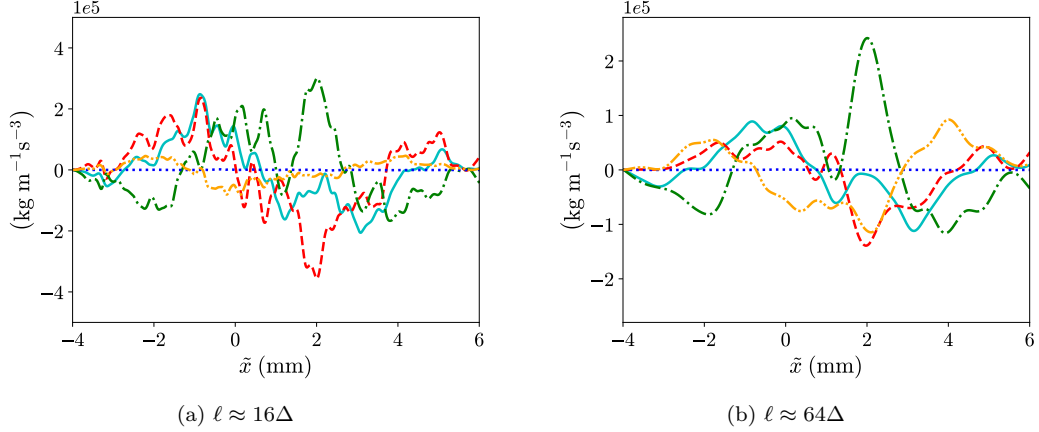


FIG. 38. Effect of filtering on compositions of turbulent transport term in the transport equation of large-scale Favre-averaged Reynolds normal stress component in streamwise direction multiplied by mean filtered density, $\langle \rho \rangle_\ell \tilde{R}_{L,11}$, at $t = 1.40$ ms. Cyan solid line: overall turbulent transport; red dashed line: $-\langle \rho \rangle_\ell \langle u \rangle_L'' \langle u \rangle_L'' \langle u \rangle_L''$; green dash-dotted line: $-2 \langle u \rangle_L' \langle p \rangle_L'$; blue dotted line: $2 \langle u \rangle_L' \langle \tau_{11} \rangle_L'$; orange dash-dot-dotted line: $-2 \langle u \rangle_L' \tau_{11}^{SFS'}$.

Appendix A: Time evolution of numbers of grid cells in simulations

Figure 39 shows the number of grid cells and weighted number of grid cells summed over all grid levels for different AMR grid resolutions over time. The weighted number of grid cells is defined as:

$$\sum_{l=0}^{l_{\max}} \frac{\Delta x_{l_{\max}}}{\Delta x_l} N_l, \quad (\text{A1})$$

where N_l and Δx_l are the number of grid cells and grid spacing respectively at level l . The maximum level number $l_{\max} = 2$ is used in this work. The weighted number of grid cells accounts for the fact that time step size is larger for grid cells at lower grid level from the CFL condition and has less computational cost compared to grid cells at higher grid levels. Since larger time step sizes are used for coarser grid levels in the multi-time stepping (sub-cycling) algorithm of the AMR code, the weighted number of grid cells is a better metric for comparing the computational cost of different AMR simulations. From figure 39, it can be seen that both the number of cells and weighted number of

cells are the largest near the end of simulation for each grid resolution. The maximum number of cells and weighted number of cells for the grid E setting are around 4.55 and 4.19 billions respectively. Both number of cells and weighted number of cells are close to each other over time since most of the grid cells are on the finest level.

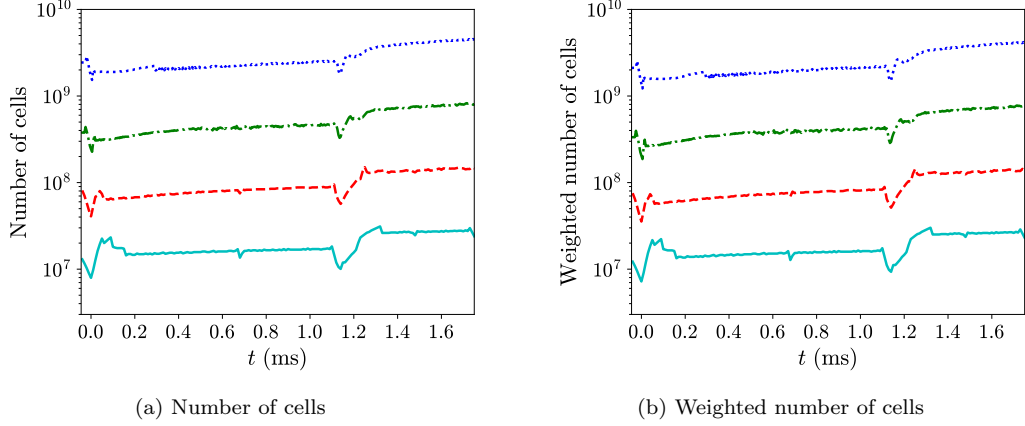


FIG. 39. Number of grid cells during the simulations. Cyan solid line: grid B; red dashed line: grid C; green dash-dotted line: grid D; blue dotted line: grid E.

Appendix B: Transport coefficients

The shear viscosity, μ_i , of a species i is given by the Chapman-Enskog's model [47]:

$$\mu_i = 2.6693 \times 10^{-6} \frac{\sqrt{M_i T}}{\Omega_{\mu,i} \sigma_i^2}, \quad (\text{B1})$$

where σ_i is the collision diameter and $\Omega_{\mu,i}$ is the collision integral of the species given by

$$\Omega_{\mu,i} = A (T_i^*)^B + C \exp(DT_i^*) + E \exp(FT_i^*), \quad (\text{B2})$$

where $T_i^* = T/(\epsilon/k)_i$, $A = 1.16145$, $B = -0.14874$, $C = 0.52487$, $D = -0.7732$, $E = 2.16178$, and $F = -2.43787$. T is the temperature of the species. $(\epsilon/k)_i$ is the Lennard-Jones energy parameter and M_i is the molecular weight of the species. The values of M_i , $(\epsilon/k)_i$, and σ_i are given in Table IV.

The bulk viscosity, μ_v , of air is given by the linear model by Gu and Ubachs [48]:

$$\mu_v = A + BT, \quad (\text{B3})$$

where $A = -3.15 \times 10^{-5} \text{ kg m}^{-1}\text{s}^{-1}$ and $B = 1.58 \times 10^{-7} \text{ kg m}^{-1}\text{s}^{-1}\text{K}^{-1}$.

The bulk viscosity, μ_v , of SF₆ is given by the Cramer's model [49]:

$$\mu_v = (\gamma - 1)^2 c_v|_v (p\tau_v), \quad (\text{B4})$$

$$c_v|_v = \left(\frac{c_v}{R} - \frac{f_r + 3}{2} \right), \quad (\text{B5})$$

$$(p\tau_v) = A \exp\left(\frac{B}{T^{1/3}} + \frac{C}{T^{2/3}} \right), \quad (\text{B6})$$

where $f_r = 3$, $A = 0.2064 \times 10^{-5} \text{ kg m}^{-1}\text{s}^{-1}$, $B = 121 \text{ K}^{1/3}$, and $C = -339 \text{ K}^{2/3}$ for SF₆.

The thermal conductivity of species i , κ_i , is defined by:

$$\kappa_i = c_{p,i} \frac{\mu_i}{Pr_i}, \quad (\text{B7})$$

where Pr_i and $c_{p,i}$ are the species-specific Prandtl number and specific heat at constant pressure respectively.

Mass diffusion coefficient of a binary mixture, D_{ij} , is given by [50]:

$$D_{ij} = D_i = D_j = \frac{0.0266}{\Omega_{D,ij}} \frac{T^{3/2}}{p\sqrt{M_{ij}\sigma_{ij}^2}}, \quad (\text{B8})$$

where p and T are the pressure and temperature of the mixture. $\Omega_{D,ij}$ is the collision integral for diffusion given by:

$$\Omega_{D,ij} = A (T_{ij}^*)^B + C \exp(DT_{ij}^*) + E \exp(FT_{ij}^*) + G \exp(HT_{ij}^*), \quad (\text{B9})$$

where $T_{ij}^* = T/T_{\epsilon_{ij}}$, $A = 1.06036$, $B = -0.1561$, $C = 0.19300$, $D = -0.47635$, $E = 1.03587$, $F = -1.52996$, $G = 1.76474$, and $H = -3.89411$. M_{ij} , σ_{ij} , and $T_{\epsilon_{ij}}$ are the effective molecular weight, collision diameter, and Lennard–Jones energy parameter respectively for the mixture:

$$M_{ij} = \frac{2}{\frac{1}{M_i} + \frac{1}{M_j}}, \quad (\text{B10})$$

$$\sigma_{ij} = \frac{\sigma_i + \sigma_j}{2}, \quad (\text{B11})$$

$$T_{\epsilon_{ij}} = \sqrt{\left(\frac{\epsilon}{k}\right)_i \left(\frac{\epsilon}{k}\right)_j}. \quad (\text{B12})$$

The values of M_i , $(\epsilon/k)_i$, and σ_i of different species are given in table IV.

TABLE IV. Fluid properties.

Gas	γ_i	$c_{p,i}$ (J kg ⁻¹ K ⁻¹)	$c_{v,i}$ (J kg ⁻¹ K ⁻¹)	M_i (g mol ⁻¹)	R_i (J kg ⁻¹ K ⁻¹)	$(\epsilon/k)_i$ (K)	σ_i (Å)	Pr_i
SF ₆	1.09312	668.286	611.359	146.055	56.9269	222.1	5.128	0.79
Air	1.39909	1040.50	743.697	28.0135	296.802	78.6	3.711	0.71

Appendix C: Mixing rules

With the assumption that all species are at pressure and temperature equilibria, the ratio of specific heats of the mixture follows as

$$\gamma = \frac{c_p}{c_v}, \quad c_p = \sum_{i=1}^N Y_i c_{p,i}, \quad c_v = \sum_{i=1}^N Y_i c_{v,i}. \quad (\text{C1})$$

The molecular weight of the mixture is given by

$$M = \left(\sum_{i=1}^N \frac{Y_i}{M_i} \right)^{-1}. \quad (\text{C2})$$

The mixture shear viscosity, bulk viscosity, and thermal conductivity are given by

$$\mu = \frac{\sum_{i=1}^N \mu_i Y_i / \sqrt{M_i}}{\sum_{i=1}^N Y_i / \sqrt{M_i}}, \quad (\text{C3})$$

$$\mu_v = \frac{\sum_{i=1}^N \mu_{v,i} Y_i / \sqrt{M_i}}{\sum_{i=1}^N Y_i / \sqrt{M_i}}, \quad (\text{C4})$$

$$\kappa = \frac{\sum_{i=1}^N \kappa_i Y_i / \sqrt{M_i}}{\sum_{i=1}^N Y_i / \sqrt{M_i}}. \quad (\text{C5})$$

[1] Robert D Richtmyer, “Taylor instability in shock acceleration of compressible fluids,” *Communications on Pure and Applied Mathematics* **13**, 297–319 (1960).

- [2] EE Meshkov, “Instability of the interface of two gases accelerated by a shock wave,” *Fluid Dynamics* **4**, 101–104 (1969).
- [3] K Kifonidis, T Plewa, L Scheck, H-Th Janka, and E Müller, “Non-spherical core collapse supernovae-II. the late-time evolution of globally anisotropic neutrino-driven explosions and their implications for SN 1987 A,” *Astronomy & Astrophysics* **453**, 661–678 (2006).
- [4] J Guzman and T Plewa, “Non-spherical core-collapse supernovae: evolution towards homologous expansion,” *Nonlinearity* **22**, 2775 (2009).
- [5] NJ Hammer, H-Th Janka, and E Müller, “Three-dimensional simulations of mixing instabilities in supernova explosions,” *The Astrophysical Journal* **714**, 1371 (2010).
- [6] David Arnett, “The role of mixing in astrophysics,” *The Astrophysical Journal Supplement Series* **127**, 213 (2000).
- [7] Steven W Haan, Stephen M Pollaine, John D Lindl, Laurance J Suter, Richard L Berger, Linda V Powers, W Edward Alley, Peter A Amendt, John A Futterman, W Kirk Levedahl, *et al.*, “Design and modeling of ignition targets for the National Ignition Facility,” *Physics of Plasmas* **2**, 2480–2487 (1995).
- [8] SW Haan, JD Lindl, DA Callahan, DS Clark, JD Salmonson, BA Hammel, LJ Atherton, RC Cook, MJ Edwards, S Glenzer, *et al.*, “Point design targets, specifications, and requirements for the 2010 ignition campaign on the National Ignition Facility,” *Physics of Plasmas* **18**, 051001 (2011).
- [9] KS Raman, VA Smalyuk, DT Casey, SW Haan, DE Hoover, OA Hurricane, JJ Kroll, A Nikroo, JL Peterson, BA Remington, *et al.*, “An in-flight radiography platform to measure hydrodynamic instability growth in inertial confinement fusion capsules at the National Ignition Facility,” *Physics of Plasmas* **21**, 072710 (2014).
- [10] Joseph Yang, Toshi Kubota, and Edward E Zukoski, “Applications of shock-induced mixing to supersonic combustion,” *AIAA journal* **31**, 854–862 (1993).
- [11] Qingchun Yang, Juntao Chang, and Wen Bao, “Richtmyer–Meshkov instability induced mixing enhancement in the scramjet combustor with a central strut,” *Advances in Mechanical Engineering* **6**, 614189 (2014).
- [12] Daniel Livescu, “Turbulence with large thermal and compositional density fluctuations,” *Annual Review of Fluid Mechanics* **52**, 309–341 (2020).
- [13] Parviz Moin and Krishnan Mahesh, “Direct numerical simulation: a tool in turbulence research,” *Annual review of fluid mechanics* **30**, 539–578 (1998).
- [14] Marcel Lesieur, Olivier Métais, Pierre Comte, *et al.*, *Large-eddy simulations of turbulence* (Cambridge university press, 2005).
- [15] Stephen B Pope, *Turbulent Flows* (Cambridge University Press, 2000).
- [16] Bruno Chaouat, “The state of the art of hybrid rans/les modeling for the simulation of turbulent flows,” *Flow, turbulence and combustion* **99**, 279–327 (2017).
- [17] Didier Besnard, Francis H Harlow, Rick M Rauenzahn, and Charles Zemach, *Turbulence transport equations for variable-density turbulence and their relationship to two-field models*, Tech. Rep. (Los Alamos National Lab., NM (United States), 1992).
- [18] Arindam Banerjee, Robert A Gore, and Malcolm J Andrews, “Development and validation of a turbulent-mix model for variable-density and compressible flows,” *Physical Review E* **82**, 046309 (2010).
- [19] K Stalsberg-Zarling and RA Gore, “The BHR2 turbulence model: incompressible isotropic decay, Rayleigh–Taylor, Kelvin–Helmholtz and homogeneous variable density turbulence,” *LANL Report*, LA-UR-11 **4773** (2011).
- [20] John D Schwarzkopf, Daniel Livescu, Robert A Gore, Rick M Rauenzahn, and J Raymond Ristorcelli, “Application of a second-moment closure model to mixing processes involving multicomponent miscible fluids,” *Journal of Turbulence*, N49 (2011).
- [21] John Dennis Schwarzkopf, Daniel Livescu, Jon Ronald Baltzer, Robert Allen Gore, and JR Ristorcelli, “A two-length scale turbulence model for single-phase multi-fluid mixing,” *Flow, Turbulence and Combustion* **96**, 1–43 (2016).
- [22] Olivier Grégoire, Denis Souffland, and Serge Gauthier, “A second-order turbulence model for gaseous mixtures induced by Richtmyer–Meshkov instability,” *Journal of Turbulence*, N29 (2005).
- [23] Brandon E Morgan and Michael E Wickett, “Three-equation model for the self-similar growth of Rayleigh–Taylor and Richtmyer–Meshkov instabilities,” *Physical Review E* **91**, 043002 (2015).
- [24] Guy Dimonte and Robert Tipton, “K-L turbulence model for the self-similar growth of the Rayleigh–Taylor and Richtmyer–Meshkov instabilities,” *Physics of Fluids* **18**, 085101 (2006).
- [25] Patrick Chassaing, “The modeling of variable density turbulent flows. a review of first-order closure schemes,” *Flow, turbulence and combustion* **66**, 293–332 (2001).
- [26] Juan Pedro Mellado, Sutanu Sarkar, and Ye Zhou, “Large-eddy simulation of rayleigh-taylor turbulence with compressible miscible fluids,” *Physics of Fluids* **17**, 076101 (2005).
- [27] Ping Wang, Jochen Fröhlich, Vittorio Michelassi, and Wolfgang Rodi, “Large-eddy simulation of variable-density turbulent axisymmetric jets,” *International Journal of Heat and Fluid Flow* **29**, 654–664 (2008).
- [28] Jing-song Bai, Jin-hong Liu, Tao Wang, Li-yong Zou, Ping Li, and Duo-wang Tan, “Investigation of the richtmyer-meshkov instability with double perturbation interface in nonuniform flows,” *Physical Review E* **81**, 056302 (2010).
- [29] DJ Hill, C Pantano, and DI Pullin, “Large-eddy simulation and multiscale modelling of a richtmyer–meshkov instability with reshock,” *Journal of fluid mechanics* **557**, 29–61 (2006).
- [30] GS Sidharth and Graham V Candler, “Stretched-vortex based subgrid-scale modeling of variable-density flows,” in *45th AIAA Fluid Dynamics Conference* (2015) p. 2782.
- [31] Man Long Wong, Daniel Livescu, and Sanjiva K Lele, “High-resolution Navier–Stokes simulations of Richtmyer–Meshkov instability with reshock,” *Physical Review Fluids* **4**, 104609 (2019).

- [32] Joseph O Hirschfelder, Charles F Curtiss, Robert Byron Bird, and Maria Goeppert Mayer, *Molecular theory of gases and liquids*, Vol. 26 (Wiley New York, 1954).
- [33] Forman A Williams, *Combustion theory* (CRC Press, 2018).
- [34] Man Long Wong, *High-order shock-capturing methods for study of shock-induced turbulent mixing with adaptive mesh refinement simulations*, Ph.D. thesis, Stanford University (2019).
- [35] Brian TN Gunney and Robert W Anderson, “Advances in patch-based adaptive mesh refinement scalability,” *Journal of Parallel and Distributed Computing* **89**, 65–84 (2016).
- [36] Brian TN Gunney, Andrew M Wissink, and David A Hysom, “Parallel clustering algorithms for structured AMR,” *Journal of Parallel and Distributed Computing* **66**, 1419–1430 (2006).
- [37] Richard D Hornung, Andrew M Wissink, and Scott R Kohn, “Managing complex data and geometry in parallel structured AMR applications,” *Engineering with Computers* **22**, 181–195 (2006).
- [38] Richard D Hornung and Scott R Kohn, “Managing application complexity in the SAMRAI object-oriented framework,” *Concurrency and computation: practice and experience* **14**, 347–368 (2002).
- [39] Andrew M Wissink, Richard D Hornung, Scott R Kohn, Steve S Smith, and Noah Elliott, “Large scale parallel structured AMR calculations using the SAMRAI framework,” in *Supercomputing, ACM/IEEE 2001 Conference* (IEEE, 2001) pp. 22–22.
- [40] Man Long Wong and Sanjiva K Lele, “High-order localized dissipation weighted compact nonlinear scheme for shock-and interface-capturing in compressible flows,” *Journal of Computational Physics* **339**, 179–209 (2017).
- [41] Chi-Wang Shu and Stanley Osher, “Efficient implementation of essentially non-oscillatory shock-capturing schemes, II,” *Journal of Computational Physics* **83**, 32–78 (1989).
- [42] M. L. Wong and S. K. Lele, “Multiresolution feature detection in adaptive mesh refinement with high-order shock-and interface-capturing scheme,” 46th AIAA Fluid Dynamics Conference, AIAA Aviation (2016).
- [43] D Livescu, JR Ristorcelli, RA Gore, SH Dean, WH Cabot, and AW Cook, “High-Reynolds number Rayleigh–Taylor turbulence,” *Journal of Turbulence* **10**, N13 (2009).
- [44] Daniel Livescu and JR Ristorcelli, “Variable-density mixing in buoyancy-driven turbulence,” *Journal of Fluid Mechanics* **605**, 145–180 (2008).
- [45] Juan A Saenz, Denis Aslangil, and Daniel Livescu, “Filtering, averaging, and scale dependency in homogeneous variable density turbulence,” *Physics of Fluids* **33**, 025115 (2021).
- [46] Andrew W Cook and William H Cabot, “Hyperviscosity for shock-turbulence interactions,” *Journal of Computational Physics* **203**, 379–385 (2005).
- [47] Sydney Chapman and TG Cowling, “The mathematical theory of non-uniform gases,” *The Mathematical Theory of Non-uniform Gases*, by Sydney Chapman and TG Cowling and Foreword by C. Cercignani, pp. 447. ISBN 052140844X. Cambridge, UK: Cambridge University Press, January 1991. , 447 (1991).
- [48] Ziyu Gu and Wim Ubachs, “A systematic study of rayleigh-brillouin scattering in air, N₂, and O₂ gases,” *The Journal of chemical physics* **141**, 104320 (2014).
- [49] MS Cramer, “Numerical estimates for the bulk viscosity of ideal gases,” *Physics of Fluids (1994-present)* **24**, 066102 (2012).
- [50] Bruce E Poling, John M Prausnitz, O’Connell John Paul, and Robert C Reid, *The properties of gases and liquids*, Vol. 5 (McGraw-Hill New York, 2001).

Supplemental Material: Analysis of second-moments and their budgets for Richtmyer–Meshkov instability with variable-density turbulence induced by re-shock

Man Long Wong*

*Department of Aeronautics and Astronautics, &
Center for Turbulence Research, Stanford, CA 94305, USA*

Jon R. Baltzer

*XTD-IDA, Los Alamos National Laboratory
Los Alamos, NM 87545, USA*

Daniel Livescu

*CCS-2, Los Alamos National Laboratory
Los Alamos, NM 87545, USA*

Sanjiva K. Lele

*Department of Aeronautics and Astronautics,
Department of Mechanical Engineering, &
Center for Turbulence Research, Stanford University
Stanford, CA 94305, USA
(Dated: October 11, 2024)*

I. PHASE SHIFTS OF INITIAL PERTURBATION

The phase shifts of each mode, ϕ_m and ψ_m , are given in table I

TABLE I. Phase shifts ϕ_m and ψ_m of each mode with wavenumber m .

m	ϕ_m	ψ_m
20	9.90312199015667e-1	2.63387681374906e+0
21	6.06257346743012e+0	3.38548538635238e+0
22	6.01619287992480e+0	2.49296356445290e+0
23	3.43615792623680e+0	2.17122208289517e+0
24	1.74985591686112e+0	1.17030742344034e+0
25	6.12864439548636e-1	5.80180501936920e-1
26	3.97323032474265e+0	9.22094456924136e-1
27	5.73890975922526e+0	1.89961157824218e+0
28	7.97881698340870e-1	7.18638171852740e-4
29	5.69125859039526e+0	4.52593227359734e+0
30	5.11905989575681e+0	2.62022653271778e+0

II. EFFECTS OF FILTER WIDTH ON LARGE-SCALE SECOND-MOMENTS AND SFS STRESS AT $t = 1.20$ ms AND $t = 1.60$ ms AFTER RE-SHOCK

The effects of filter width on the large-scale second-moments: $\overline{\langle \rho \rangle_\ell a_{L,1}}$, $\overline{\langle \rho \rangle_\ell b_L}$, and $\overline{\langle \rho \rangle_\ell \tilde{R}_{L,11}}$ at $t = 1.20$ ms and $t = 1.60$ ms obtained with grid E after re-shock are shown in figures 1, 2, and 3 respectively. Figure 4 shows the effect of filter width on the large-scale turbulent kinetic energy. The effects of filtering on the mean SFS stress component in streamwise direction, $\overline{\tau_{11}^{SFS}}$, and the mean SFS turbulent kinetic energy, $\overline{\tau_{ii}^{SFS}}/2$, are shown in figures 5 and 6 respectively.

* mlwong@alumni.stanford.edu

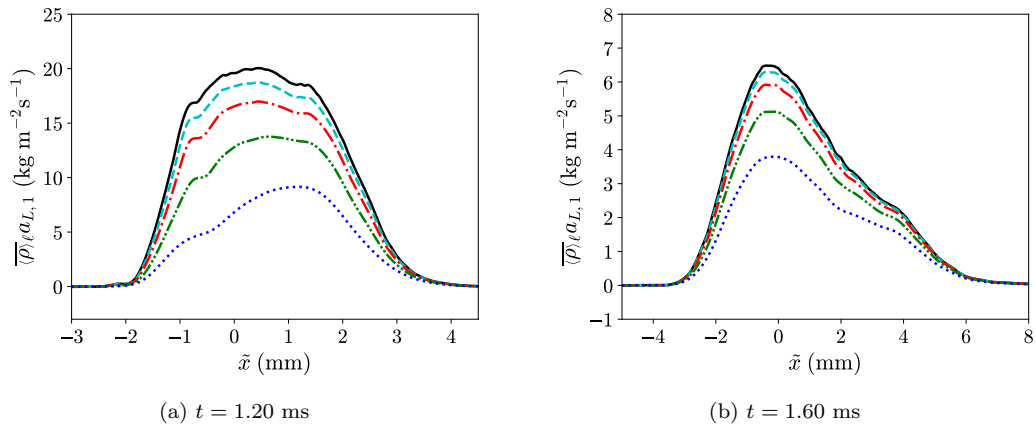


FIG. 1. Effect of filtering on large-scale turbulent mass flux component in streamwise direction, $\overline{(\rho)_\ell a_{L,1}}$, at $t = 1.20$ ms and $t = 1.60$ ms after re-shock. Black solid line: no filtering; cyan dashed line: $\ell \approx 8\Delta$; red dash-dotted line: $\ell \approx 16\Delta$; green dash-dot-dotted line: $\ell \approx 32\Delta$; blue dotted line: $\ell \approx 64\Delta$.

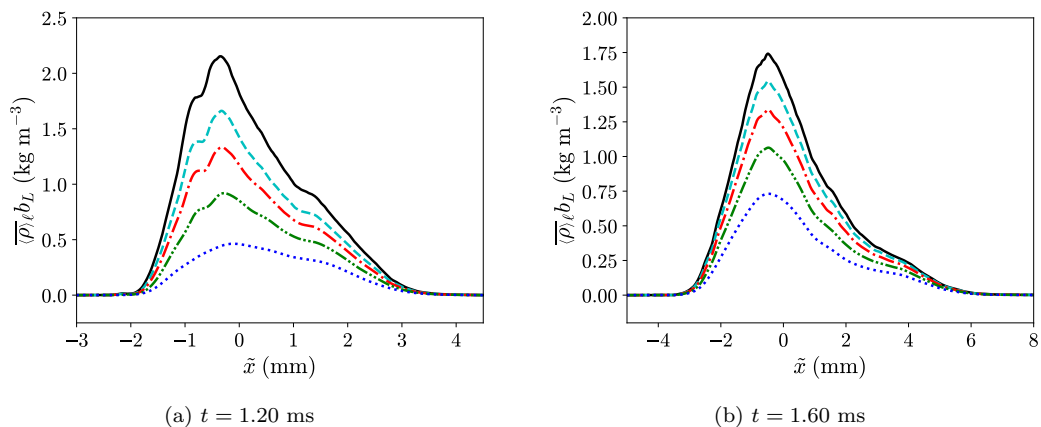


FIG. 2. Effect of filter width on large-scale density-specific-volume covariance multiplied by mean filtered density, $\overline{(\rho)_\ell b_L}$, at $t = 1.20$ ms and $t = 1.60$ ms after re-shock. Black solid line: no filtering; cyan dashed line: $\ell \approx 8\Delta$; red dash-dotted line: $\ell \approx 16\Delta$; green dash-dot-dotted line: $\ell \approx 32\Delta$; blue dotted line: $\ell \approx 64\Delta$.

III. BUDGETS OF LARGE-SCALE SECOND-MOMENTS AT $t = 1.40$ ms AND $t = 1.75$ ms AFTER RE-SHOCK

The budgets of $\overline{(\rho)_\ell a_{L,1}}$, $\overline{(\rho)_\ell b_L}$, $\overline{(\rho)_\ell \tilde{R}_{L,11}}$, and $\overline{(\rho)_\ell k_L}$ at $t = 1.40$ ms and $t = 1.75$ ms obtained with grid E after re-shock are shown respectively in figures 7, 8, 9, and 10. The compositions of the production term and destruction term of $\overline{(\rho)_\ell a_{L,1}}$ at the two times are displayed in figures 11 and 12 respectively. The compositions of the production term and turbulent transport term of $\overline{(\rho)_\ell \tilde{R}_{L,11}}$ at the two times are shown in figures 13 and 14 respectively.

IV. UNFILTERED BUDGETS AND FILTERED BUDGETS OF SECOND-MOMENTS AFTER RE-SHOCK WITH $\ell \approx 32\Delta$

The budgets of unfiltered second-moments and those of the large-scale second-moments with $\ell \approx 32\Delta$ obtained with grid E at $t = 1.40$ ms are shown in figures 15, 16, 17, and 18 respectively. The compositions of the production term and destruction term of $\overline{(\rho)_\ell a_{L,1}}$ at the same time are displayed in figures 19 and 20 respectively. The compositions of the production term and turbulent transport term of $\overline{(\rho)_\ell \tilde{R}_{L,11}}$ are shown in figures 21 and 22 respectively.

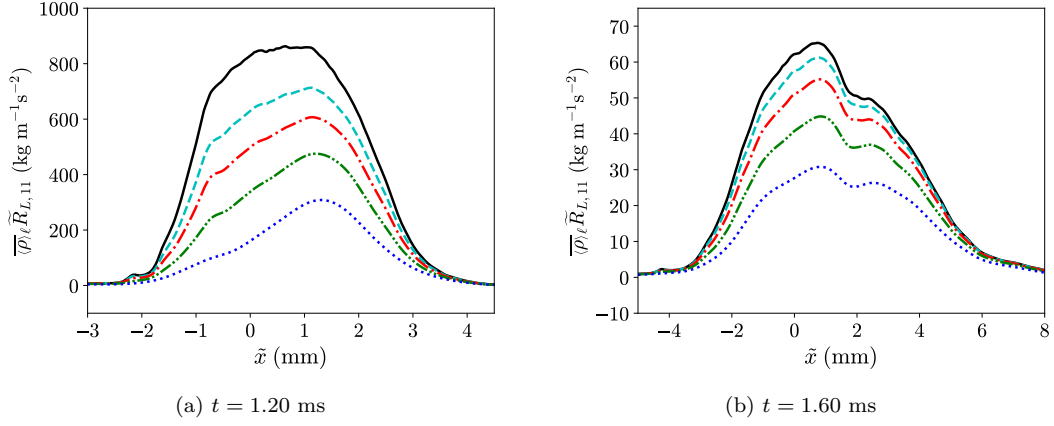


FIG. 3. Effect of filtering on large-scale Reynolds normal stress component in streamwise direction multiplied by mean filtered density, $\overline{\langle \rho \rangle}_\ell \widetilde{R}_{L,11}$, at $t = 1.20$ ms and $t = 1.60$ ms after re-shock. Black solid line: no filtering; cyan dashed line: $\ell \approx 8\Delta$; red dash-dotted line: $\ell \approx 16\Delta$; green dash-dot-dotted line: $\ell \approx 32\Delta$; blue dotted line: $\ell \approx 64\Delta$.

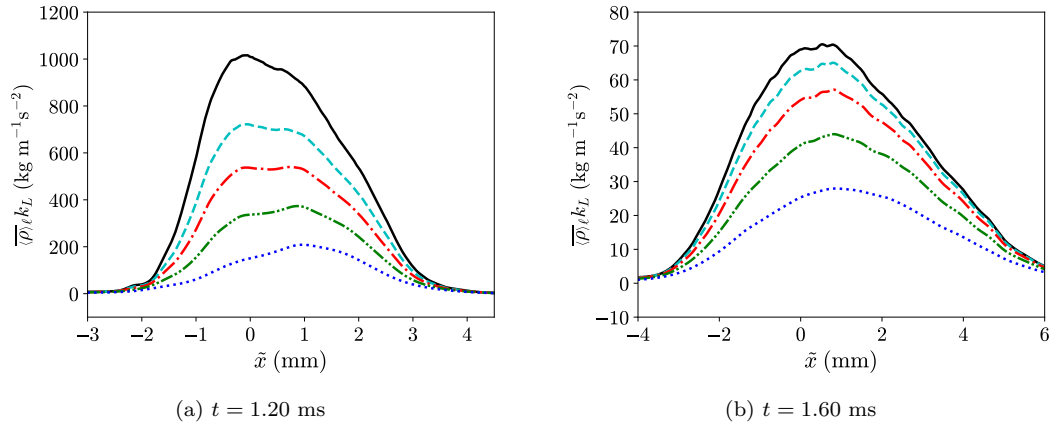


FIG. 4. Effect of filtering on large-scale turbulent kinetic energy, $\overline{\langle \rho \rangle}_\ell k_L$, at $t = 1.20$ ms and $t = 1.60$ ms after re-shock. Black solid line: no filtering; cyan dashed line: $\ell \approx 8\Delta$; red dash-dotted line: $\ell \approx 16\Delta$; green dash-dot-dotted line: $\ell \approx 32\Delta$; blue dotted line: $\ell \approx 64\Delta$.

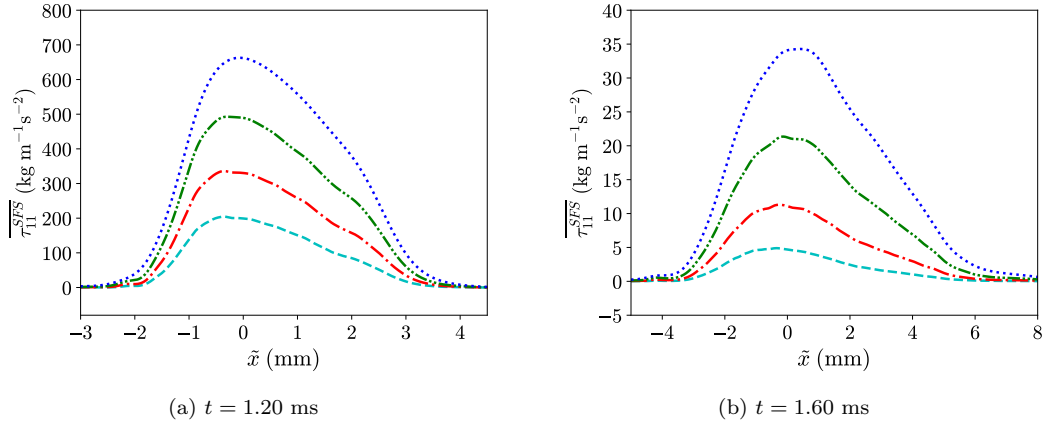


FIG. 5. Effect of filtering on mean SFS stress component in streamwise direction, $\overline{\tau_{11}^{SFS}}$, at $t = 1.20$ ms and $t = 1.60$ ms after re-shock. Cyan dashed line: $\ell \approx 8\Delta$; red dash-dotted line: $\ell \approx 16\Delta$; green dash-dot-dotted line: $\ell \approx 32\Delta$; blue dotted line: $\ell \approx 64\Delta$.

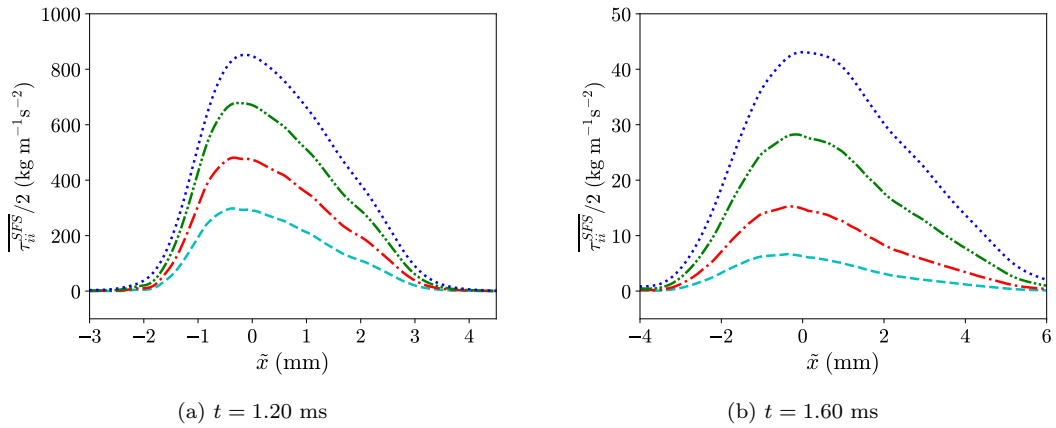


FIG. 6. Effect of filtering on mean SFS turbulent kinetic energy, $\overline{\tau_{ii}^{SFS}}/2$, at $t = 1.20$ ms and $t = 1.60$ ms after re-shock. Cyan dashed line: $\ell \approx 8\Delta$; red dash-dotted line: $\ell \approx 16\Delta$; green dash-dot-dotted line: $\ell \approx 32\Delta$; blue dotted line: $\ell \approx 64\Delta$.

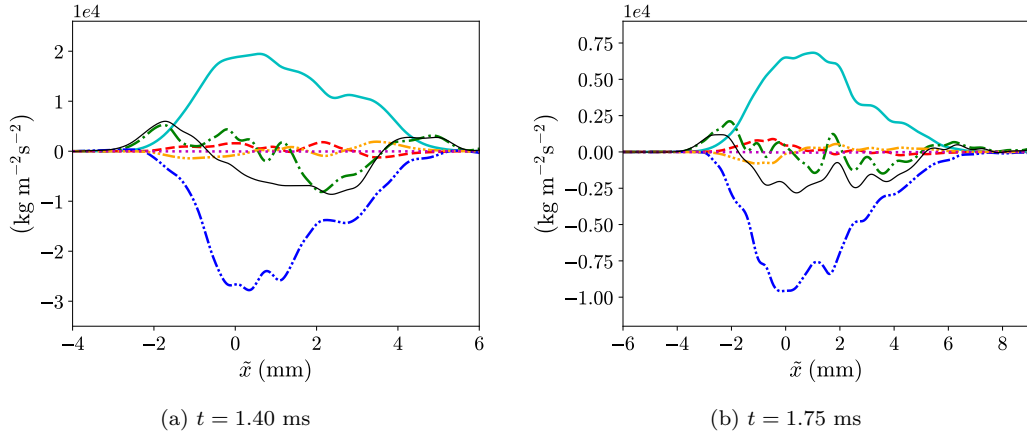


FIG. 7. Budgets of large-scale turbulent mass flux component in streamwise direction, $\overline{\langle \rho \rangle_\ell a_{L,1}}$, at $t = 1.40$ ms and $t = 1.75$ ms after re-shock. Cyan solid line: production (III); red dashed line: redistribution (IV); green dash-dotted line: turbulent transport (V); blue dash-dot-dotted line: destruction (VI); orange dash-triple-dotted line: negative of convection due to streamwise velocity associated with turbulent mass flux; magenta dotted line: residue; thin black solid line: summation of all terms (rate of change in the moving frame).

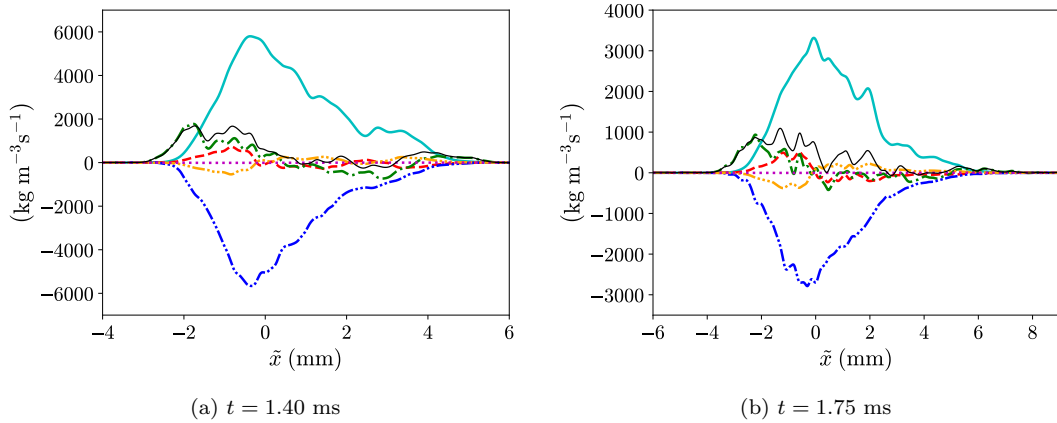


FIG. 8. Budgets of large-scale density-specific-volume covariance multiplied by mean filtered density, $\overline{\langle \rho \rangle_\ell b_L}$, at $t = 1.40$ ms and $t = 1.75$ ms after re-shock. Cyan solid line: production (III); red dashed line: redistribution (IV); green dash-dotted line: turbulent transport (V); blue dash-dot-dotted line: destruction (VI); orange dash-triple-dotted line: negative of convection due to streamwise velocity associated with turbulent mass flux; magenta dotted line: residue; thin black solid line: summation of all terms (rate of change in the moving frame).

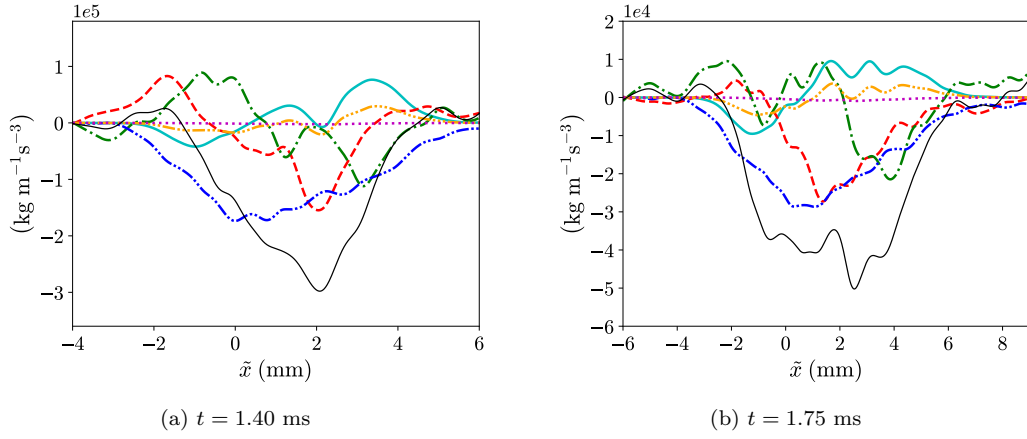


FIG. 9. Budgets of large-scale Favre-averaged Reynolds normal stress component in streamwise direction multiplied by mean filtered density, $\overline{(\rho)_\ell} \overline{R_{L,11}}$, at $t = 1.40$ ms and $t = 1.75$ ms after re-shock. Cyan solid line: production (III); red dashed line: press-strain redistribution (V); green dash-dotted line: turbulent transport (IV); blue dash-dot-dotted line: dissipation (VI); orange dash-triple-dotted line: negative of convection due to streamwise velocity associated with turbulent mass flux; magenta dotted line: residue; thin black solid line: summation of all terms (rate of change in the moving frame).

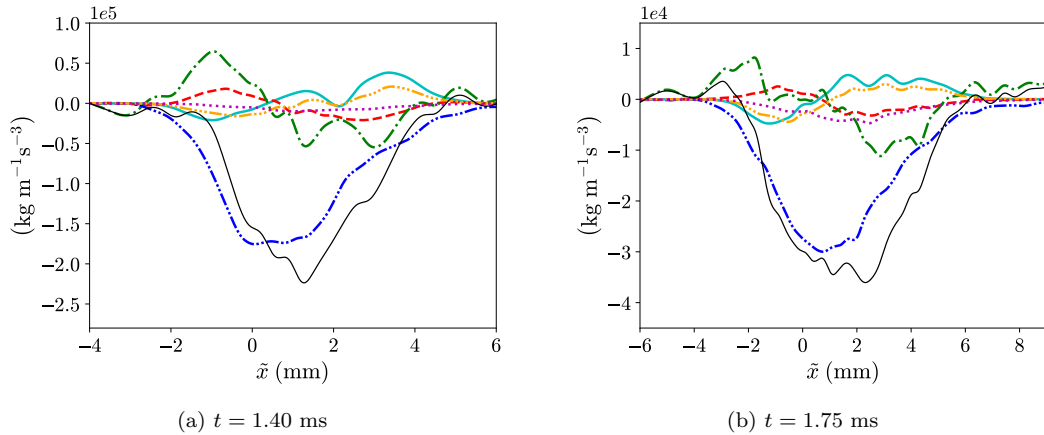


FIG. 10. Budgets of large-scale turbulent kinetic energy, $\overline{(\rho)_\ell} k_L$, at $t = 1.40$ ms and $t = 1.75$ ms after re-shock. Cyan solid line: production (III); red dashed line: pressure-dilatation (V); green dash-dotted line: turbulent transport (IV); blue dash-dot-dotted line: dissipation (VI); orange dash-triple-dotted line: negative of convection due to streamwise velocity associated with turbulent mass flux; magenta dotted line: residue; thin black solid line: summation of all terms (rate of change in the moving frame).

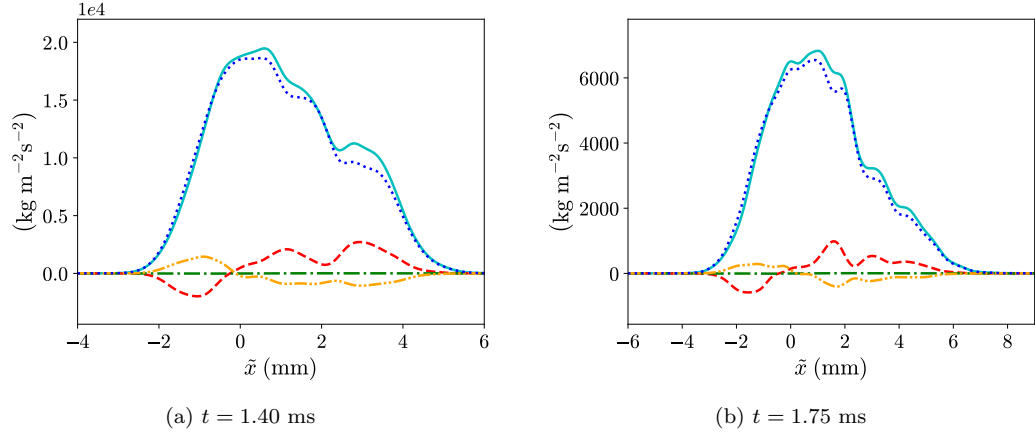


FIG. 11. Compositions of production term in the transport equation of large-scale turbulent mass flux component in streamwise direction, $\overline{\langle \rho \rangle}_\ell a_{L,1}$, at $t = 1.40$ ms and $t = 1.75$ ms after re-shock. Cyan solid line: overall production; red dashed line: $b_L \overline{\langle p \rangle}_{\ell,1}$; green dash-dotted line: $-b_L \overline{\langle \tau_{11} \rangle}_{\ell,1}$; orange dash-dot-dotted line: $b_L \overline{\tau_{11}^{SFS}}_{\ell,1}$; blue dotted line: $-\widetilde{R}_{L,11} \overline{\langle \rho \rangle}_{\ell,1}$.

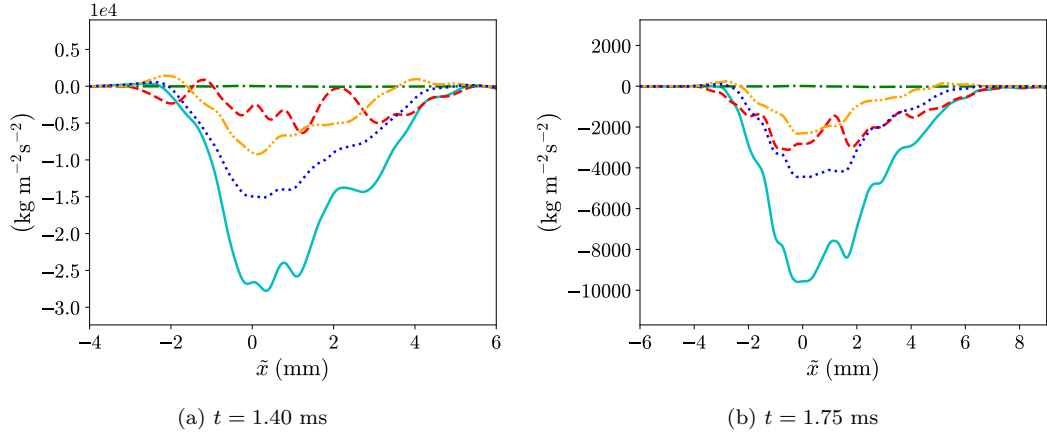


FIG. 12. Compositions of destruction term in the transport equation of large-scale turbulent mass flux component in streamwise direction, $\overline{\langle \rho \rangle}_\ell a_{L,1}$, at $t = 1.40$ ms and $t = 1.75$ ms after re-shock. Cyan solid line: overall destruction; red dashed line: $\overline{\langle \rho \rangle}_\ell (1/\langle \rho \rangle)_\ell' \langle p \rangle'_{\ell,1}$; green dash-dotted line: $-\overline{\langle \rho \rangle}_\ell (1/\langle \rho \rangle)_\ell' (\partial \langle \tau_{1i} \rangle'_\ell / \partial x_i)$; orange dash-dot-dotted line: $\overline{\langle \rho \rangle}_\ell (1/\langle \rho \rangle)_\ell' (\partial \tau_{1i}^{SFS})' / \partial x_i$; blue dotted line: $\overline{\langle \rho \rangle}_\ell \varepsilon_{a_{L,1}}$.

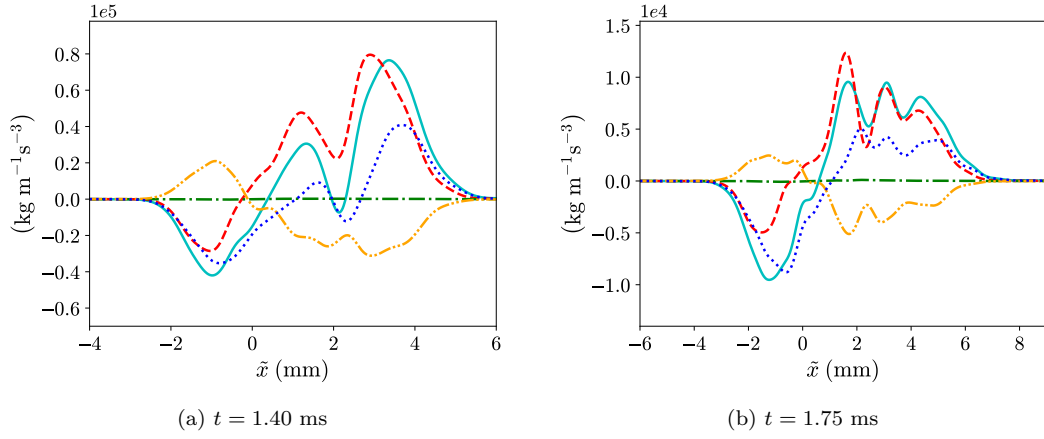


FIG. 13. Compositions of production term in the transport equation of large-scale Favre-averaged Reynolds normal stress component in streamwise direction multiplied by mean filtered density, $\langle \rho \rangle_\ell \tilde{R}_{L,11}$, at $t = 1.40$ ms and $t = 1.75$ ms after re-shock. Cyan solid line: overall production; red dashed line: $2a_{L,1} \langle \tilde{p} \rangle_{\ell,1}$; green dash-dotted line: $-2a_{L,1} \langle \tilde{\tau}_{11} \rangle_{\ell,1}$; orange dash-dot-dotted line: $2a_{L,1} \tau_{11}^{SFS}$; blue dotted line: $-2 \langle \rho \rangle_\ell \tilde{R}_{L,11} \langle \tilde{u} \rangle_{L,1}$.

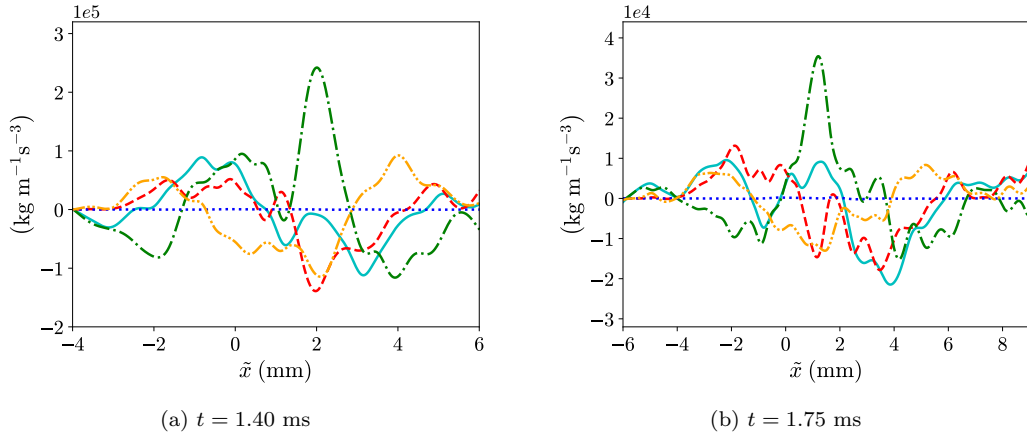


FIG. 14. Compositions of turbulent transport term in the transport equation of large-scale Favre-averaged Reynolds normal stress component in streamwise direction multiplied by mean filtered density, $\langle \rho \rangle_\ell \tilde{R}_{L,11}$, at $t = 1.40$ ms and $t = 1.75$ ms after re-shock. Cyan solid line: overall turbulent transport; red dashed line: $-\langle \rho \rangle_\ell \langle u \rangle_L'' \langle u \rangle_L'' \langle u \rangle_L''$; green dash-dotted line: $-2 \langle u \rangle_L' \langle p \rangle_\ell'$; blue dotted line: $2 \langle u \rangle_L' \langle \tau_{11} \rangle_\ell'$; orange dash-dot-dotted line: $-2 \langle u \rangle_L' \tau_{11}^{SFS}$.

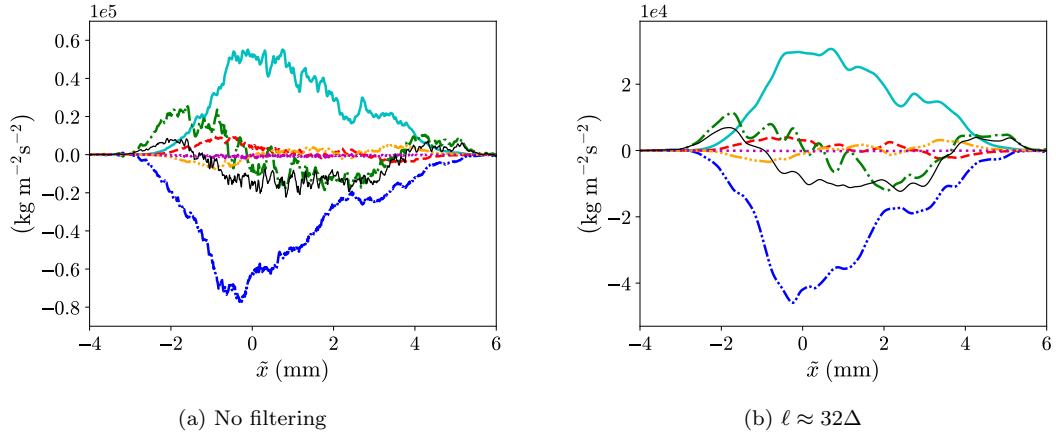


FIG. 15. Effect of filtering on budgets of large-scale turbulent mass flux component in streamwise direction, $\overline{(\rho)}_\ell a_{L,1}$, at $t = 1.40$ ms. Cyan solid line: production (III); red dashed line: redistribution (IV); green dash-dotted line: turbulent transport (V); blue dash-dot-dotted line: destruction (VI); orange dash-triple-dotted line: negative of convection due to streamwise velocity associated with turbulent mass flux; magenta dotted line: residue; thin black solid line: summation of all terms (rate of change in the moving frame).

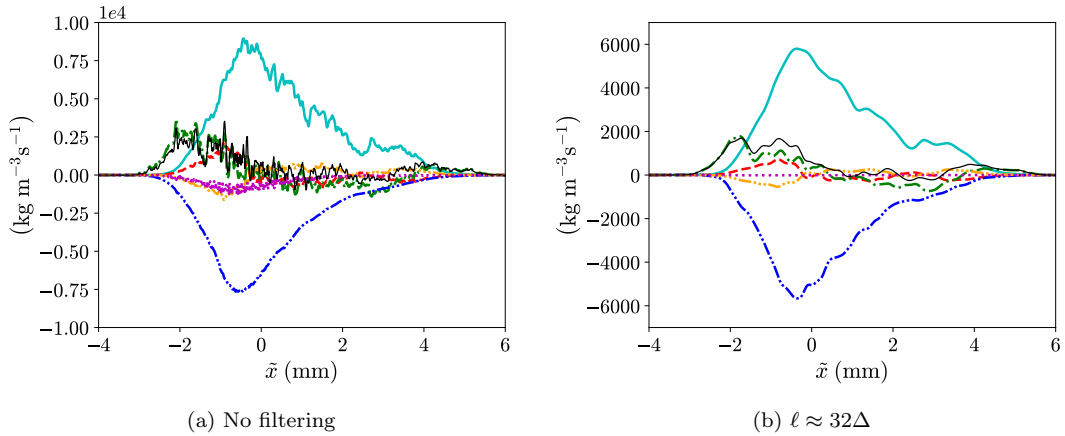


FIG. 16. Effect of filtering on budgets of large-scale density-specific-volume covariance multiplied by mean filtered density, $\overline{(\rho)}_\ell b_L$, at $t = 1.40$ ms. Cyan solid line: production (III); red dashed line: redistribution (IV); green dash-dotted line: turbulent transport (V); blue dash-dot-dotted line: destruction (VI); orange dash-triple-dotted line: negative of convection due to streamwise velocity associated with turbulent mass flux; magenta dotted line: residue; thin black solid line: summation of all terms (rate of change in the moving frame).

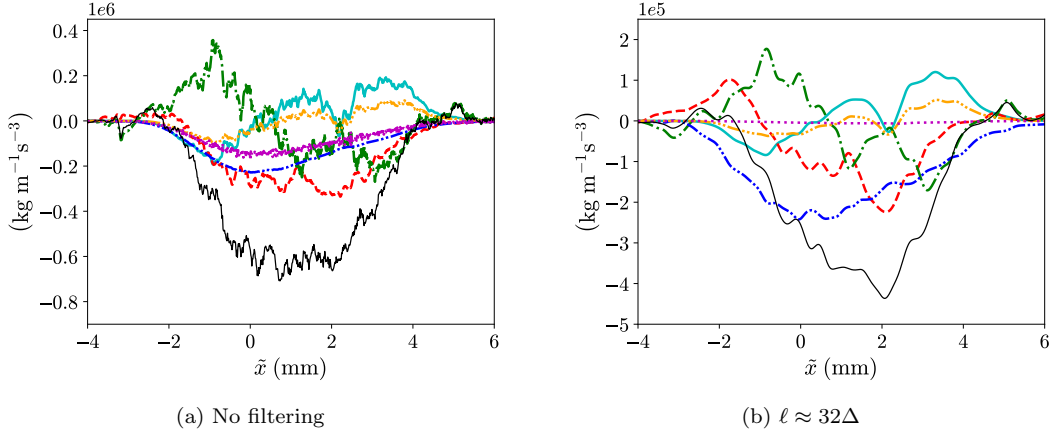


FIG. 17. Effect of filtering on budgets of large-scale Reynolds normal stress component in streamwise direction multiplied by mean filtered density, $\overline{(\rho)}_\ell \widetilde{R}_{L,11}$, at $t = 1.40$ ms. Cyan solid line: production (III); red dashed line: press-strain redistribution (V); green dash-dotted line: turbulent transport (IV); blue dash-dot-dotted line: dissipation (VI); orange dash-triple-dotted line: negative of convection due to streamwise velocity associated with turbulent mass flux; magenta dotted line: residue; thin black solid line: summation of all terms (rate of change in the moving frame).

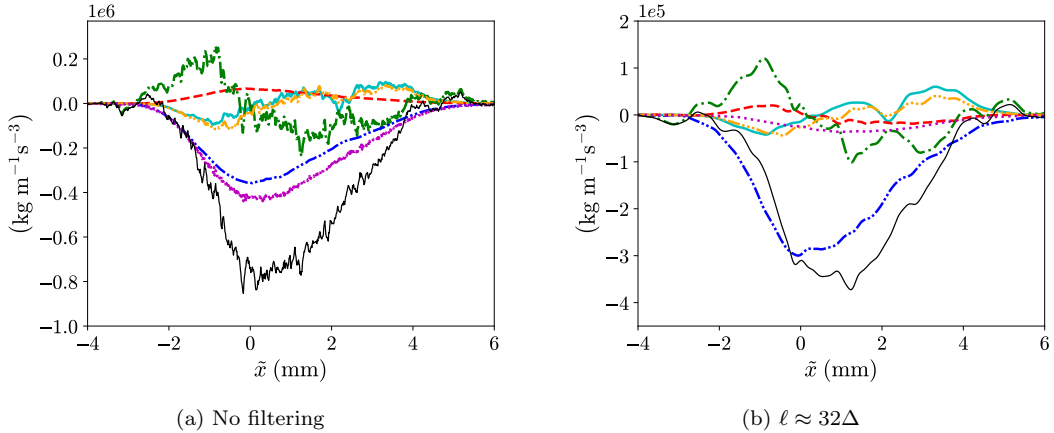


FIG. 18. Effect of filtering on budgets of large-scale turbulent kinetic energy, $\overline{(\rho)}_\ell k_L$, at $t = 1.40$ ms. Cyan solid line: production (III); red dashed line: pressure-dilatation (V); green dash-dotted line: turbulent transport (IV); blue dash-dot-dotted line: dissipation (VI); orange dash-triple-dotted line: negative of convection due to streamwise velocity associated with turbulent mass flux; magenta dotted line: residue; thin black solid line: summation of all terms (rate of change in the moving frame).

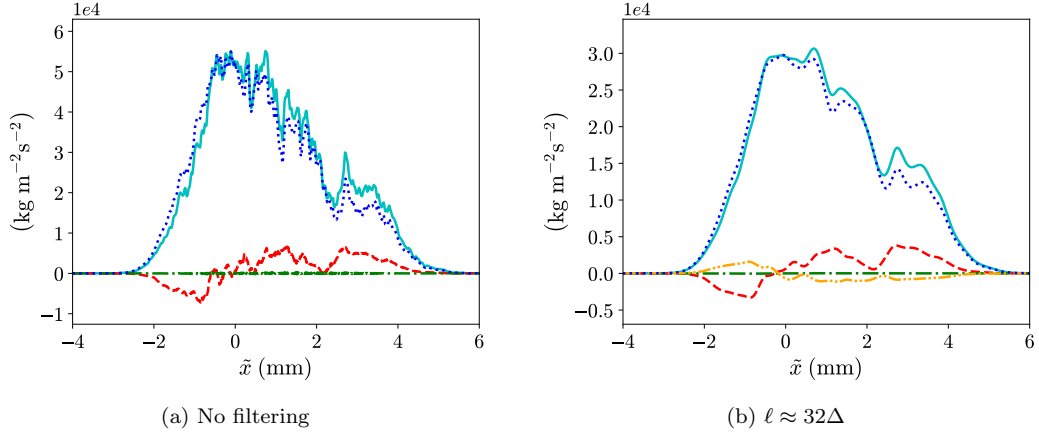


FIG. 19. Effect of filtering on compositions of production term in the transport equation of large-scale turbulent mass flux component in streamwise direction, $\overline{\langle \rho \rangle}_{\ell} a_{L,1}$, at $t = 1.40$ ms. Cyan solid line: overall production; red dashed line: $b_L \overline{\langle \rho \rangle}_{\ell,1}$; green dash-dotted line: $-b_L \overline{\langle \tau_{11} \rangle}_{\ell,1}$; orange dash-dot-dotted line: $b_L \overline{\tau_{11}^{SFS}}_{,1}$; blue dotted line: $-\widetilde{R}_{L,11} \overline{\langle \rho \rangle}_{\ell,1}$.

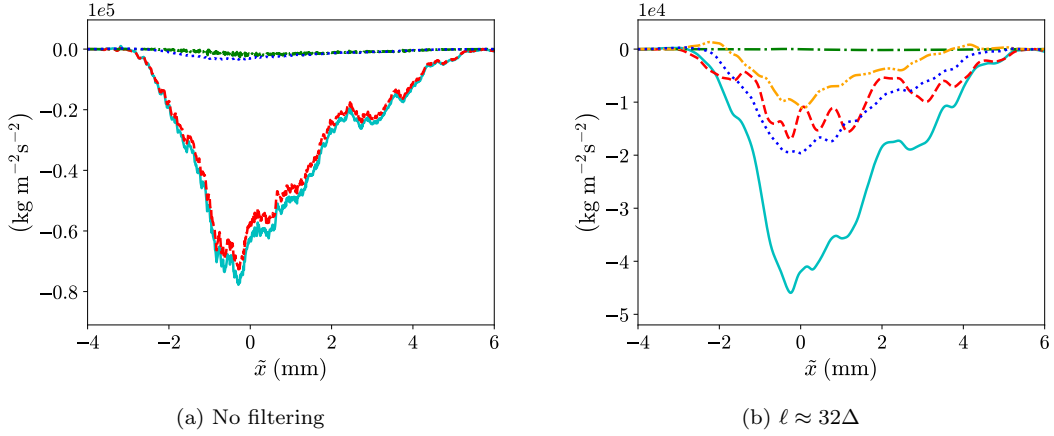


FIG. 20. Effect of filtering on compositions of destruction term in the transport equation of large-scale turbulent mass flux component in streamwise direction, $\overline{\langle \rho \rangle}_{\ell} a_{L,1}$, at $t = 1.40$ ms. Cyan solid line: overall destruction; red dashed line: $\overline{\langle \rho \rangle}_{\ell} (1/\langle \rho \rangle_{\ell})' \langle \rho \rangle'_{\ell,1}$; green dash-dotted line: $-\overline{\langle \rho \rangle}_{\ell} (1/\langle \rho \rangle_{\ell})' (\partial \langle \tau_{1i} \rangle'_{\ell} / \partial x_i)$; orange dash-dot-dotted line: $\overline{\langle \rho \rangle}_{\ell} (1/\langle \rho \rangle_{\ell})' (\partial \tau_{1i}^{SFS'} / \partial x_i)$; blue dotted line: $\overline{\langle \rho \rangle}_{\ell} \varepsilon_{a_{L,1}}$.

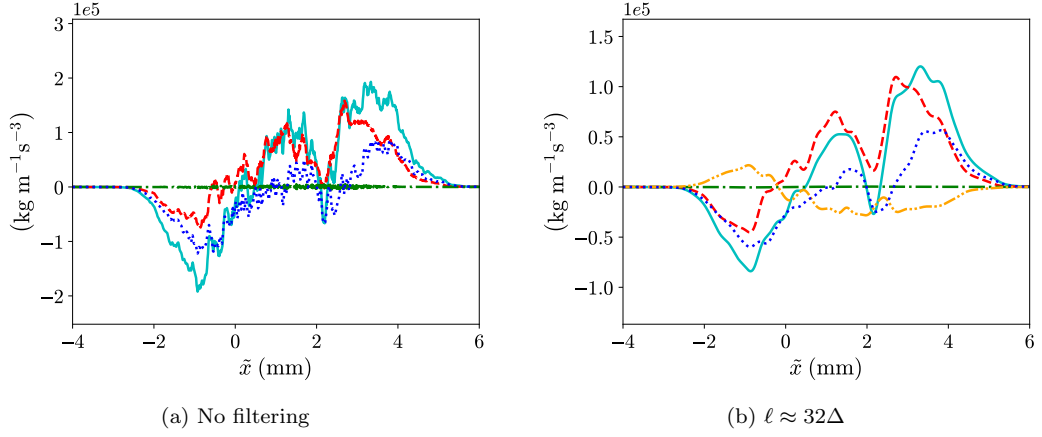


FIG. 21. Effect of filtering on compositions of production term in the transport equation of large-scale Favre-averaged Reynolds normal stress component in streamwise direction multiplied by mean filtered density, $\langle \rho \rangle_\ell \widetilde{R}_{L,11}$, at $t = 1.40$ ms. Cyan solid line: overall production; red dashed line: $2a_{L,1} \langle p \rangle_{\ell,1}$; green dash-dotted line: $-2a_{L,1} \langle \tau_{11} \rangle_{\ell,1}$; orange dash-dot-dotted line: $2a_{L,1} \overline{\tau_{11}^{SFS}}_{,1}$; blue dotted line: $-2 \langle \rho \rangle_\ell \widetilde{R}_{L,11} \langle u \rangle_{L,1}$.

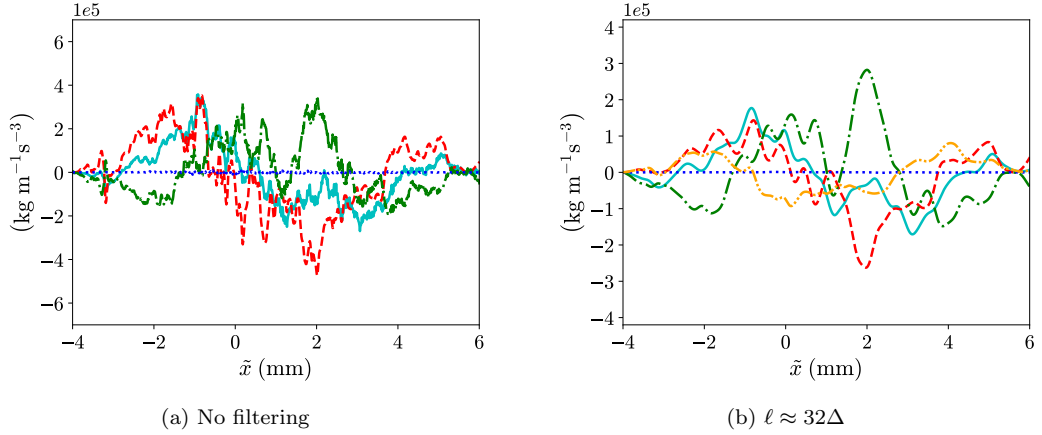


FIG. 22. Effect of filtering on compositions of turbulent transport term in the transport equation of large-scale Favre-averaged Reynolds normal stress component in streamwise direction multiplied by mean filtered density, $\langle \rho \rangle_\ell \widetilde{R}_{L,11}$, at $t = 1.40$ ms. Cyan solid line: overall turbulent transport; red dashed line: $-\langle \rho \rangle_\ell \langle u \rangle'_L \langle u \rangle''_L \langle u \rangle''_L$; green dash-dotted line: $-2 \langle \langle u \rangle'_L \langle p \rangle'_\ell \rangle_{,1}$; blue dotted line: $2 \langle \langle u \rangle'_L \langle \tau_{11} \rangle'_\ell \rangle_{,1}$; orange dash-dot-dotted line: $-2 \langle \langle u \rangle'_L \tau_{11}^{SFS'} \rangle_{,1}$.